

Interaction between wave hydrodynamics and flexible vegetation

Alejandra Gijón Mancheño

Msc. Thesis

 TU Delft

Interaction between wave hydrodynamics and flexible vegetation

by

Alejandra Gijón Mancheño

in partial fulfillment of the requirements for the degree of

Master of Science

Coastal & Marine Engineering and Management

at the Delft University of Technology, to be defended publicly on Tuesday June 28th, 2016 at
10:30 AM.

Thesis committee:

Prof. dr. ir. W.S.J. Uijtewaald, TU Delft

Prof. dr. ir. A.J.H.M. Reniers, TU Delft

Dr. ir. N. Jacobsen, Deltares

Dr. ir. R. Uittenbogaard, Deltares

Dr. ir. B.K. Van Wesenbeeck, TU Delft/Deltares

An electronic version of this thesis is available at

<http://repository.tudelft.nl/>

Correspondence with the author may be directed to:

alegijonman@hotmail.com



The CoMEM programme

The Erasmus+: Erasmus Mundus MSc in Coastal and Marine Engineering and Management is an integrated programme including mobility organized by five European partner institutions, coordinated by Norwegian University of Science and Technology (NTNU).

The joint study programme of 120 ECTS credits (two years full-time) has been obtained at two or three of the five CoMEM partner institutions:

- Norges Teknisk- Naturvitenskapelige Universitet (NTNU) Trondheim, Norway
- Technische Universiteit (TU) Delft, The Netherlands
- Universitat Politècnica de Catalunya (UPC). BarcelonaTech. Barcelona, Spain
- University of Southampton, Southampton, Great Britain
- City University London, London, Great Britain

During the first three semesters of the programme, students study at two or three different universities depending on their track of study. In the fourth and final semester an MSc project and thesis has to be completed. The two-year CoMEM programme leads to a multiple set of officially recognized MSc diploma certificates. These will be issued by the universities that have been attended by the student. The transcripts issued with the MSc Diploma Certificate of each university include grades/marks and credits for each subject.

Information regarding the CoMEM programme can be obtained from the programme coordinator:

Øivind A. Arntsen, Dr.ing.

Associate professor in Marine Civil Engineering

Department of Civil and Transport Engineering

NTNU Norway

Telephone: +4773594625

Cell: +4792650455

Fax: + 4773597021

Email: ovind.arntsen@ntnu.no

CoMEM URL: <https://www.ntnu.edu/studies/mscomem>

CoMEM Thesis

This thesis was completed by:

Alejandra Gijón Mancheño

Under supervision of:

Prof. dr. ir. W.S.J. Uijtewaal, TU Delft

Prof. dr. ir. A.J.H.M. Reniers, TU Delft

Dr. ir. N. Jacobsen, Deltares

Dr. ir. R. Uittenbogaard, Deltares

Dr. ir. B.K. Van Wesenbeeck, TU Delft/Deltares

As a requirement to attend the degree of

*Erasmus+: Erasmus Mundus Master in Coastal and Marine Engineering and Management
(CoMEM)*

Taught at the following educational institutions:

Norges Teknisk- Naturvitenskapelige Universitet (NTNU), Trondheim, Norway

Technische Universiteit (TU) Delft, Delft, The Netherlands

University of Southampton, Southampton, Great Britain

At which the student has studied from August 2014 to July 2016.

Acknowledgements

This report is the result of my thesis for the Erasmus Master Course in Coastal and Maritime Engineering and Management, where I have studied the interaction between wave hydrodynamics and flexible vegetation using a process-based model, Dynveg.

This thesis would not be possible without the support of my committee. Thanks Wim for giving me the opportunity to take part in this research. Thank you also for your guidance, useful comments and support. My work involved analysing Dynveg in detail, but you always helped me keep a broader perspective and look beyond my work. Thanks Niels and Rob for your time and guidance throughout the process. You helped me structure my research and provided me with your insights on the physical processes, among many other things. Your comments allowed me to complete my thesis, but more importantly, they will help me during the rest of my career. Thanks Ad for your insightful remarks during the meetings and for your role not only in my thesis, but for the whole CoMEM group. Thank you Bregje for providing your perspective and expertise in a topic where a multidisciplinary approach is essential.

Thanks to my friends, both from CoMEM and from back home, for your support. I particularly want to thank Ana and Stuart, for the discussions about our projects and many other topics, and for all the good moments spent together while working on our theses.

Thanks to Jorge for his unconditional support during all these years.

And finally, I want to thank to my parents, Juan Antonio y Toñi. I do not think that it possible to receive more love and support than what you have shown me.

Thanks to everyone,

Alejandra Gijón Mancheño

Delft, June 2016.

Summary

Aquatic vegetation attenuates local currents, dampens wave energy and promotes sedimentation. Its function as shoreline defence has gained strong interest in the recent years, since it may offer sustainable and cost-effective solutions to coastal protection problems. Predictions of wave dissipation by macrophytes require understanding of the hydrodynamics, plant motion and the coupling between the two. Moreover, the presence of aquatic organisms affects the velocity field across different scales, from the interactions with individual plants to the effects of a community of elements, and different methodologies are applied for each of them.

Dynveg focuses on the interaction between the organisms and the surrounding fluid at the stem-scale. It describes the motion of a blade based on the balance between the parameterized flow-induced loads and the restoring action of the stiffness and the buoyancy of the plant. It has been validated against experimental data for steady flows (Dijkstra and Uittlenbogaard, 2010). Döbken (2015) further developed Dynveg for its implementation under wave hydrodynamics. Bakker (2015) conducted a series of experiments using artificial plants in the wave flume of the Fluid Mechanics Laboratory, at Delft University of Technology, in order to generate data to evaluate the performance of the model.

The present work aimed to use the laboratory measurements to validate Dynveg for oscillatory flows, in the small plant deformation regime (i.e., using the data of the most rigid stem). Additional checks were carried out to validate the modelled tip displacement under uniformly distributed loads.

After its validation, Dynveg was applied in a one-way coupling using different velocity profiles. The analysis started from a depth-uniform oscillatory flow and the complexity of the flow was progressively increased by adding the effect of the variations of the velocity over the water column, changes along the horizontal coordinate, non-linear effects and the eulerian flow in successive steps.

Several conclusions were derived from the results. Plants have been observed to describe asymmetric trajectories under waves both in the field and laboratory experiments (Luhar et al., 2010; Luhar and Nepf, 2016), with larger deflections in the direction of wave propagation. This behaviour had been attributed to wave non-linearities and to the streaming within the canopy. The asymmetry in the motion was not present in the results of Dynveg when the input velocity profile was constant over the vertical. Nevertheless, it appeared when linear wave theory was implemented, before introducing higher harmonics or the effect of the mean flow. The results seem to suggest that the orbital water motion drives the asymmetric plant posture under waves, although higher order effects may enhance it even further. This would have a number of implications on the methods used to study plant behaviour under waves. For instance U-tubes produce depth-uniform velocity profiles and their use in the laboratory would not include the mechanism that drives asymmetric plant motion.

Variations of the velocity along the horizontal coordinate had a comparatively smaller influence in the predictions than the changes over the vertical for the analysed conditions, although that may not be necessarily the case for values of stiffness below the tested range or under more energetic wave conditions.

Other trends found in the existing literature were also identified in the model results. Plant motion led the water flow in accordance to the observations by Mullarney and Henderson (2010) and Stevens and Hurd (2001). When stems with different flexibilities were modelled under the same wave conditions, the most rigid plants produced more energy dissipation. The model results showed that the work of a flexible stem could be the same that of a completely still plant even for tip excursions equal to the 20% of the stem height. This could considerably simplify the methods used to predict wave attenuation, since for those cases it would not be necessary to model plant motion. The modelled work decreased for the lowest values of stiffness. Longer plants were able to reduce their relative motion with respect to the fluid for a longer part of the wave period, whereas shorter stems stayed deflected for a longer fraction of the wave cycle in accordance to the studies by Gaylord and Denny (1997) and

Bradley and Houser (2009). When the dimensionless work was plotted against the Cauchy number the curves corresponded to different stem lengths converged, with maximum discrepancies of around 10% for intermediate values of Ca . Such relationships could be applied to develop simplified expressions to account for wave dissipation in computationally demanding coastal models

It was concluded that Dynveg showed a satisfactory performance reproducing both the results of the experiments and field observations from the literature. The next step would be its validation against the experimental data obtained testing the most flexible stems. The model could also be validated using velocities measured within a canopy, at the laboratory or at the field, in order to incorporate the effect of the mass drift inside the vegetation.

Once validated, Dynveg could be used in multiple applications. Firstly, more simple predictive frameworks could be developed to account for wave attenuation. The results of sensitivity analysis could be very useful in the planning of field campaigns, for instance in determining which parameters require more accurate measurements. Dynveg could also be combined with statistical methods to account for the variability in plant properties within a natural canopy and to evaluate the rates of gap formation in a meadow. The later application could have important implications to the success of future restoration projects.

Table of contents

1. Introduction.....	15
1.1. Problem description.....	15
1.2. Scope and objectives	16
1.3. Approach	17
1.4. Report outline.....	18
2. Theoretical background	19
2.1. Flow over immersed bodies.....	19
2.2. Wave hydrodynamics	32
3. Model.....	35
3.1. Dynamic blade model.....	35
3.2. Numerical implementation	37
4. Experiments by Bakker.....	39
4.1. Set-up	39
4.2. Observations.....	40
5. Model validation for submerged rigid cylinders.....	41
5.1. Determination of the force coefficients	41
5.2. Validation of Dynveg.....	46
6. Analysis of plant dynamics under wave loading with Dynveg	51
6.1. Depth-uniform oscillatory flow	52
6.2. Linear wave theory.....	54
6.3. Linear wave theory including horizontal variations of the velocity field.....	62
6.4. Eulerian flow.....	66
6.5. Second order Stokes waves	68
7. Discussion	71
7.1. Plant posture and stem excursion	71
7.2. Relative plant velocity	73
7.3. Base forces.....	74
7.4. Effect of spatial variations in the velocity field	75
7.5. Eulerian flow.....	76
7.6. Formulation of the drag.....	77
7.7. Wave dissipation.....	78
8. Conclusions and recommendations.....	81
8.1. Conclusions	81
8.2. Recommendations.....	82
9. References	87

1. Introduction

1.1. Problem description

Aquatic vegetation (or macrophytes) encompasses different species of organisms, such as coral reefs, algae forests, mangroves, and seagrasses, among others. They are an important part of coastal, estuarine and freshwater environments and provide multiple ecosystem services (Dijkstra, 2006). Macrophytes serve as a habitat for many species of birds, insects, and other aquatic life (Zedler et al., 2001; Greenberg et al., 2006). They enhance water quality by filtering, oxygen production and nutrient recycling (Peterson et al., 1984; Hemminga and Duarte, 2000). Moreover, aquatic vegetation attenuates local currents (Gambi et al., 1990), dampens wave energy (Fonseca and Calahan, 1992; Knutson et al., 1982; Möller et al., 1999) and promotes sedimentation (Shi et al., 2012; Callaghan et al., 2010), subsequently acting as a buffer against flooding and erosion. The function of coastal vegetation as a shoreline defence has gained strong interest due to the increasing concern and uncertainty related to sea level rise (Borje et al., 2011) and the increasing popularity of soft-engineering measures in coastal protection (Capobianco and Stive, 2000, Hook et al. 1988).

Predictions of wave attenuation by macrophytes require understanding of the hydraulic processes in vegetation fields (Suzuki and Arikawa, 2011). This involves knowledge of the hydrodynamics (waves and currents), plant motion, and the interaction between the two. Furthermore, the presence of aquatic vegetation influences the velocity field across different scales, from turbulence production at a single stem to changes in the mean flow due to the cumulative effect of the elements of a meadow (Nepf, 2011). Initial models of wave dampening (Darylmpole et al., 1984, Kobayashi et al., 1993) related wave height reduction with the work done by drag force acting on the blades. They introduced a number of assumptions, such as considering plants as rigid cylinders, the application of the linear wave theory and the use of calibration parameters among others (Nepf, 2011). However, even though such approaches proved to be applicable in practice, they are not suitable for the case of flexible vegetation since they do not reproduce the underlying physical processes.

The study of wave attenuation has been addressed with different methodologies at the different scales involved (Zeller et al., 2014). Flow at the scale of the individual plants is dominated by the no-slip condition at every surface of contact (Nepf, 2012). Such a condition produces an energy transfer by turbulent motions from the mean flow to the molecular scale, where the energy is dissipated into heat. Numerical models for flow through vegetation with rigid stems have been developed and used extensively to reproduce such interactions (Li and Xie, 2011). Direct numerical simulation (DNS) of the flow characteristics is still restricted to small-scale domains [$0 (10^{-3})$ to $0 (10^{-2})$ m] and low Reynolds number environments because of its high computational cost (Chakrabarti et al., 2016). As a consequence, most of the research has focused on Large Eddy Simulation (LES) models, which explicitly solve canopy turbulence larger than twice the grid mesh, and Reynolds Averaged Navier–Stokes equations (RANS) models, which only simulate mean velocity fields and require explicit specification of momentum sinks in the model equations (Chakrabarti et al., 2016).

Nevertheless, the computational complexity of the problem increases considerably when the vegetation is flexible, since it requires accounting for the continuously varying geometry and position of the plants. Some attempts have been done based on the assumption of small plant deflection, such as those by Kutija and Hong (1996) or Erduarn and Kutija (2003). Ikeda et al. (2001) developed a 2D-LES model to simulate the wavy motion of flexible vegetation using a complex plant grid to track the movement of each stem. However, these kind of methods are too computationally demanding, which have led to the development of more simplified solutions to account for the interaction between vegetation and water motion. A widespread alternative consists of representing the momentum loss at the plant-fluid interface through the use of parameterized forces that depend on empirical coefficients. Several models of plant motion have been developed, schematizing an individual stem or blade as a number of segments and applying a balance between the parameterized fluid-induced loads and

the restoring forces acting at each of those sections (for instance, those proposed by Mullarney and Henderson, 2010; Zeller et al., 2014; Abdelhram, 2007; Luhar and Nepf, 2016, among others). These approaches may be used to acquire a better understanding of the flow-induced dynamics at flexible elements under varying hydrodynamic conditions. Moreover, their findings can be applied to develop simple predictive frameworks that can be implemented in large-scale coastal models (Luhar and Nepf, 2016), where the dimensions of the domain make it unfeasible to use sufficiently fine grids to account for stem-scale processes. The inclusion of vegetation dynamics in wave attenuation models can be done through the use of drag coefficients or effective plant lengths in the momentum equations that incorporate the feedback between blade bending and water flow.

Dynveg belongs to the category of process-based approaches. It simulates the movement of one single plant based on a Lagrangian balance between the posture-dependent hydrodynamic forces and the restoring action of buoyancy and stiffness (Dijkstra, 2006; Uittenbogaard, 2006). It has been successfully combined with the large-scale model Delft3D to reproduce two-dimensional physical processes in meadows of flexible vegetation under steady flow (Dijkstra, 2006). It has also been applied together with an existing 1DV k-e turbulence model and validated against observations of plant motion, forces on vegetation and flow characteristics from laboratory experiments (Dijkstra et al., 2010). Döbken (2015) further developed Dynveg for its implementation under unsteady flows. A set of experiments was conducted in the wave flume of the Fluid Mechanics Laboratory at Delft University of Technology, in order to generate data to validate the performance of the model for oscillatory flows. Individual artificial plants were tested in a number of wave conditions, and stem positions, flow velocities and horizontal base forces were measured for each of those cases (Bakker, 2015). The aim of the present study is to use this data-set to evaluate the performance of Dynveg and, once validated, to apply it to obtain a better insight on plant response to wave hydrodynamics.

1.2. Scope and objectives

The present thesis aims to improve the understanding of the processes between wave hydrodynamics and flexible vegetation using Dynveg to model the motion of one single stem. The research objectives can be summarized as follows:

- Validation of Dynveg for the small deformation regime. Evaluation of the model capability to reproduce the measured forces obtained by Bakker (2015) in a set of laboratory experiments using a stiff mimic. Analysis of the performance of the model predicting tip motion using the equation of the deflection at the end of a cantilever beam.
- Description the physical processes experienced by vegetation under wave hydrodynamics using Dynveg. Analysis of how changes in the wave properties and the associated flow kinematics affect the response of a stem. Evaluation of the influence of the characteristics of the vegetation (geometry, rigidity) on wave dissipation. Qualitative comparison of the results and trends reproduced by the model with the existing literature.
- Evaluation of the suitability of U-tubes to study plant motion under wave hydrodynamics. Flow visualization tests are easy to perform in U-tubes, which may make them attractive candidates to analyse plant motion. The flow conditions generated in such structures have been simulated using Dynveg in order to study if they can reproduce the hydrodynamic forcing and plant behaviour experienced by submerged plants under waves.
- Analysis of the limitations associated with the use of velocity profiles computed at one single location instead of a spatially varying velocity field. As a stem deflects, the different parts of the plant will be exposed to different phases of a wave. Such an effect is neglected when the velocity profile is only specified at one position.

1.3. Approach

The study was addressed in two steps:

- (1) Model validation for rigid vegetation
- (2) Analysis of the response of plants under wave loading using Dynveg.

1.3.1. Model validation for rigid vegetation

Dynveg was validated against the laboratory measurements obtained by Bakker (2015) testing the most rigid stem, for which the plant motion could be considered negligible. This simplifies the problem, since it is not necessary to reproduce the plant dynamics to evaluate the fluid forces on the vegetation. The Morison formulation is a semi-empirical equation that relates fluid forces with the kinematic properties of the flow through force coefficients. The value of such coefficients was determined by fitting the formula using the velocity and force time-series recorded in the experiments. A pair of values was determined for each of the wave conditions in which the plant was tested. The empirical coefficients together with the measured velocities were implemented as an input of the model. The computed forces were compared with the measurements, to evaluate the accuracy of the model. Additional checks were done in order to evaluate the performance of Dynveg, making use of the equation of the cantilever beam and reproducing forces calculated from linear wave theory.

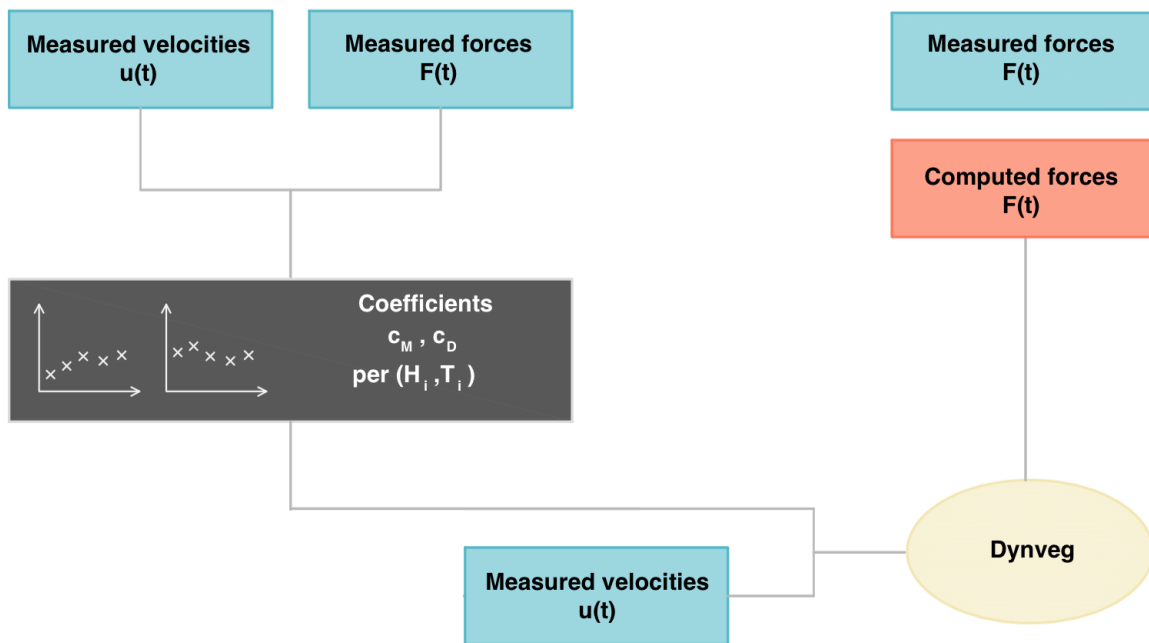


Figure 1. Flow chart of the Dynveg validation cycle for a rigid plant, using the velocity and force time-series recorded during the laboratory experiments for a single stem.

1.3.2. Analysis of plant dynamics under waves using Dynveg

Once the model was validated, it was used to study the response of a vegetation stem under waves. This analysis was conducted starting from the simplest case, a depth-uniform periodic flow. The complexity was progressively increased by implementing linear wave theory (introducing changes along the vertical coordinate), including horizontal variations in the velocity field and adding other higher-order effects (such as the effect of the return flow caused by mass transport by waves and non-linearity's associated with steep waves).

Each of these effects were applied individually and then finally combined to see how they contributed to the behaviour of the stem. The influence of varying the properties of the plant (size, shape, stiffness) was also evaluated.

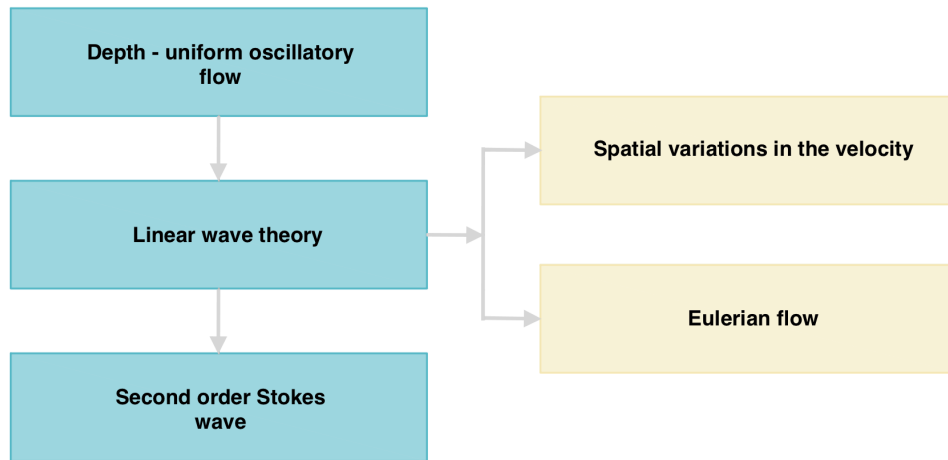


Figure 2. Flow chart representing the structure of the analysis of plant dynamics under wave loading.

1.4. Report outline

The relevant literature to contextualize the present work is presented in Section 2. The equations of Dynveg and the characteristics of its numerical implementation are introduced in Section 3. A series of flume experiments using plastic strips was conducted to obtain data to analyse the performance of the model. The set-up of such experiments is presented in Section 4. The validation procedure for a rigid stem and the obtained results are exposed in Section 5. Some of the results of Dynveg displayed fluctuations that were further analysed in Appendix B. Additional checks of the model are presented in Appendix A. The influence of the timestep and the numerical integration method are evaluated in Appendix C.

After validating Dynveg, different wave kinematics and plant properties were tested in a series of model runs. The results of the analysis are shown in Section 7 and discussed in Section 8. The influence of the initial flow velocity on the computed plant motion was studied in Appendix D. The main conclusions and recommendations of the study are summarized in Section 9. The first steps in the validation of the model using experimental data of flexible vegetation are presented in Appendix E.

2. Theoretical background

The present Section provides an overview on the interaction between the vegetation and the surrounding fluid, starting with the processes caused by one single element (such as blades or stems) and progressively increasing the complexity until explaining the dynamics of a community of organisms. A still object immersed in a steady current results in the development of a boundary layer on its surface, and the characteristics of such region determine the resistance exerted by the vegetation on the fluid, as exposed in Section 2.1.1. When the flow is unsteady, additional inertial forces arise as a consequence of the changes in the velocity field. This aspect is further explored in Section 2.1.3. By reorienting and following the water motion, plants can modify their position under more extreme conditions to reduce the hydrodynamic forces. A brief review of this adaptive mechanism is presented in Section 2.1.4.1. Plant motion increases the complexity of the problem, since in order to evaluate the magnitude of the loads, it is necessary to reproduce the behaviour of the body. The different ways in which reconfiguration is addressed are discussed in Section 2.1.4.2. The problems associated with modelling plant dynamics and the characteristics of the existing models are presented in Section 2.1.4.3. The influence of one single plant on the hydrodynamics can be considered negligible. However, the cumulative effect of the forces in a canopy produces changes in the mean flow, drains energy from the fluid and attenuates waves. Such topics are discussed in more detail in Section 2.1.5. Lastly, some of the existing theories and equations to model wave hydrodynamics are introduced in Section 2.2.

2.1. Flow over immersed bodies

2.1.1. Flow past individual rigid elements in steady flow

2.1.1.1. Development of the boundary layer

Flow at the scale of the individual elements is dominated by the no-slip condition at every surface (i.e., stem, blades and branches) (Nepf, 2011), which states that there will be no relative motion between a solid boundary and the viscous fluid immediately in contact with it (Day, 1990). The thin region on the surface of a body in which the fluid velocity changes from zero to the velocity of the undisturbed flow is denoted as boundary layer (Munson et al., 2013). Low fluid velocities and high velocity gradients result in a higher relative importance of viscous effects with respect to inertial effects and laminar flow within this region. As the thickness of the layer increases in the direction of the flow, perturbations may be stronger and overcome viscous damping (Nepf, 2011). This results in an outer region governed by turbulent transport of momentum and a second region, adjacent to the solid surface, where viscous shear stresses dominate (Stevens and Hurd, 2001). The Reynolds number defines the relative importance of inertial and viscous effects, Re :

$$Re = \frac{u \cdot D}{\nu} \quad (2.1)$$

Where u is the fluid velocity, D is a characteristic length scale of the object and ν is the kinematic viscosity of the fluid. As the Reynolds number becomes larger, the importance of viscous effects is confined to a smaller region near the body, whereas for low Reynolds numbers, the presence of the object is felt throughout a relatively large portion of the flow field.

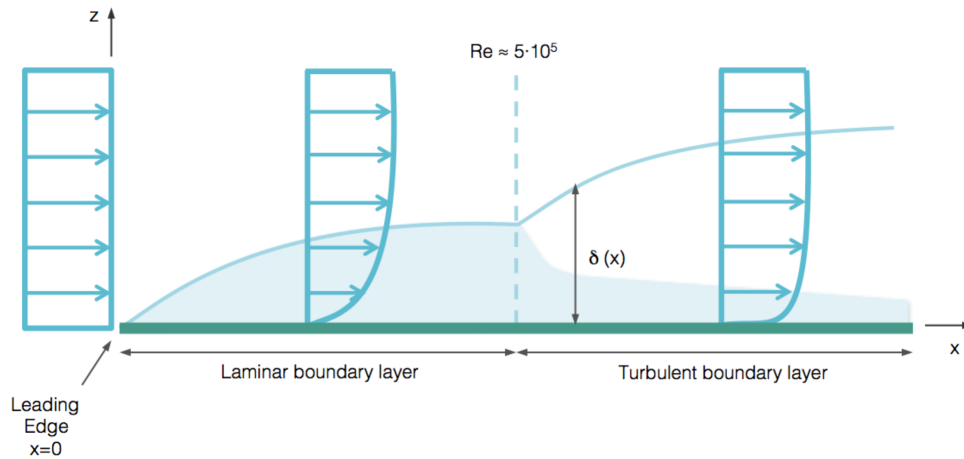


Figure 3. Idealized sketch of the flow regions within the boundary layer along a blade schematized as a flat plate (green line). Its thickness increases along the plate and is denoted by $\delta(x)$. The boundary layer is initially laminar right after the leading edge and becomes turbulent when the Reynolds number based on the distance along the plate ($D = x$) reaches a value of approximately $Re \approx 5 \cdot 10^5$ (White, 2008). After the transition, only a fraction of the layer of the remains laminar, the viscous sublayer (shaded area).

In the cases where the morphology of the macrophyte is more irregular (for instance due to the presence of corrugations or bulbs in the blades) or when the branches or stems have a blunt shape, fluid particles experience changing pressure gradients as they travel along the curved surface (Hurd et al., 1996). If the energy losses due to friction are high enough, the boundary layer will not be able to overcome the adverse pressure gradient along the rear half of the undulation. This will result in flow separation and a wake region behind the object where the fluid recirculates and travels against the upstream flow. Boundary separation causes a decrease in the average pressure at the downstream side compared to the front part of the body, producing a force in the direction of the flow.

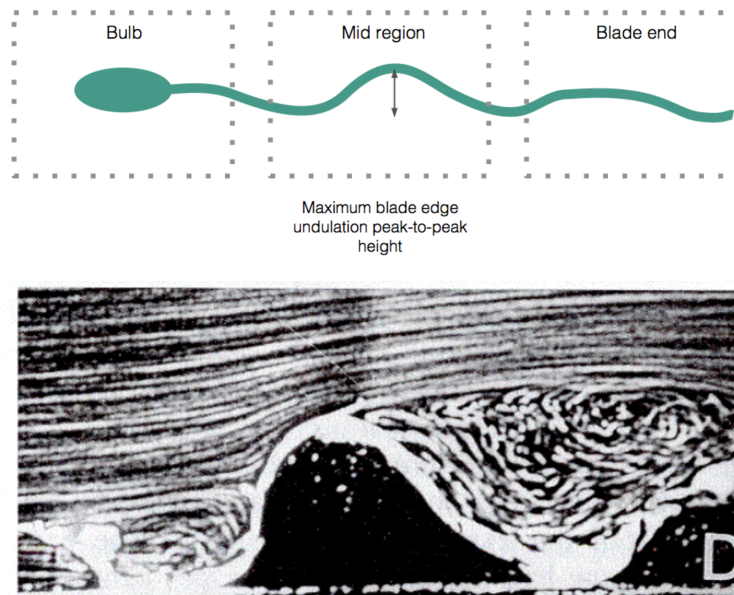


Figure 4. The upper plot shows a schematic side view of an exposed blade of *Macrocystis Integrifolia* from a wave-sheltered site. The square boxes indicate the bulb, middle and end regions of the blade. The lower plot shows flow separation behind the undulations at the middle region, photographed during laboratory visualization experiments in the University of British Columbia (Hurd et al., 1997).

2.1.1.2. Forces acting on a rigid submerged body in steady flow

The interactions at the fluid-surface interface can be described in terms of both (turbulent and viscous) shear stresses on the body, τ_w , and normal stresses due to the pressure, p . The resultant force parallel to the upstream velocity is termed the drag force, F_D , and is given by:

$$F_D = \int p \cos \theta dA + \int \tau_w \sin \theta dA \quad (2.2)$$

Here dA is a differential area element and θ defines the angle between the flow and the line perpendicular to the surface of the object. Since the distributions of the stresses are often very difficult to obtain, the drag force is usually parameterized using a quadratic law:

$$F_D = \frac{1}{2} c_D \rho u^2 A \quad (2.3)$$

Where A is the frontal area of the element from the direction of the flow, u is the flow velocity, ρ is the fluid density and c_D is a dimensionless drag coefficient which includes the effect of both viscous and form (pressure) drag.

2.1.1.3. Factors affecting the drag coefficient

The size of the wake and the nature of the flow inside of it depend on several factors, such as fluid properties, flow speed and the geometry of the immersed body. Some species, such as *Spartina anglica* marshes can be approximated as circular vertical cylinders (Mendez and Losada, 2004). For circular cross-sections there is a strong dependency between the drag coefficient and the Reynolds number, which is illustrated in Figure 5. The magnitude of tidal currents in coastal wetlands usually ranges between $0.02 - 0.06 \text{ m/s}$ adjacent to the vegetation canopy, and $0.01 - 0.04 \text{ m/s}$ inside of it (Liu et al., 2016). Given the normally small scale of the vegetation, the associated Reynolds numbers vary between low and moderate values. For the smallest Re the flow remains attached to the surface and no separation occurs. Within the range of $5 < Re < 40$ a pair of symmetric laminar vortices form in the wake of the cylinder (Sumer and Fredsøe, 2006). With increasing flow velocity the wake becomes unstable and vortices are shed alternatively at each side of the cylinder, forming a vortex street. A further increase in Re causes a transition from the initially laminar regime to turbulence within the wake, which is complete for $Re > 200$. The drag coefficient has an approximately constant value of 1 for higher Reynolds numbers (Munson et al., 2013). Increasing surface roughness and incoming turbulence result in an earlier transition to turbulence in the boundary layer (Sumer and Fredsøe, 2006).

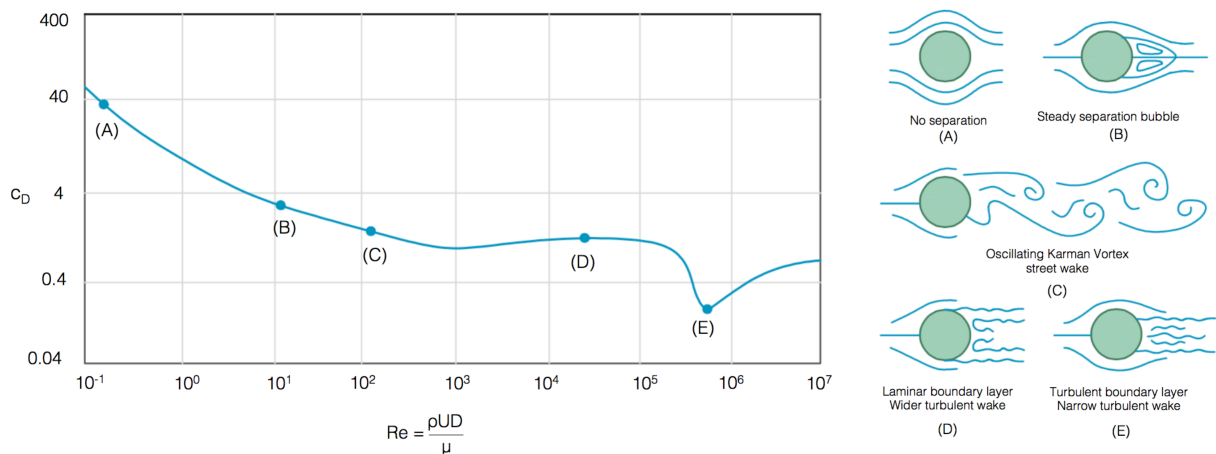


Figure 5. (a) Drag coefficient for a circular cross-section as a function of the Reynolds number. (b) Boundary layer and wake structure for different Reynolds numbers. Adapted from: (Munson et al., 2013)

For sharp-edged bodies the flow separates at the edges of the object regardless of the nature of the boundary layer, resulting in a smaller dependence on Re . Varying angles of incidence, α , are related to the movement of the corners where flow separation occurs, as shown in Figure 6. Changes in the orientation of the body may lead to asymmetries in the shear layers emanating from the two sides of the cross-section and differences in the way they interact. They can also produce variations in the wake width, the possibility of flow reattachment on one of the surfaces after separation in the leading edges, and changes in the vortex formation length among other aspects (McClellan and Sumner, 2004). Larger widths result in wider wakes and higher drag forces (Venugopal et al., 2005). Variations in any of these factors may modify the values of c_D for submerged objects.

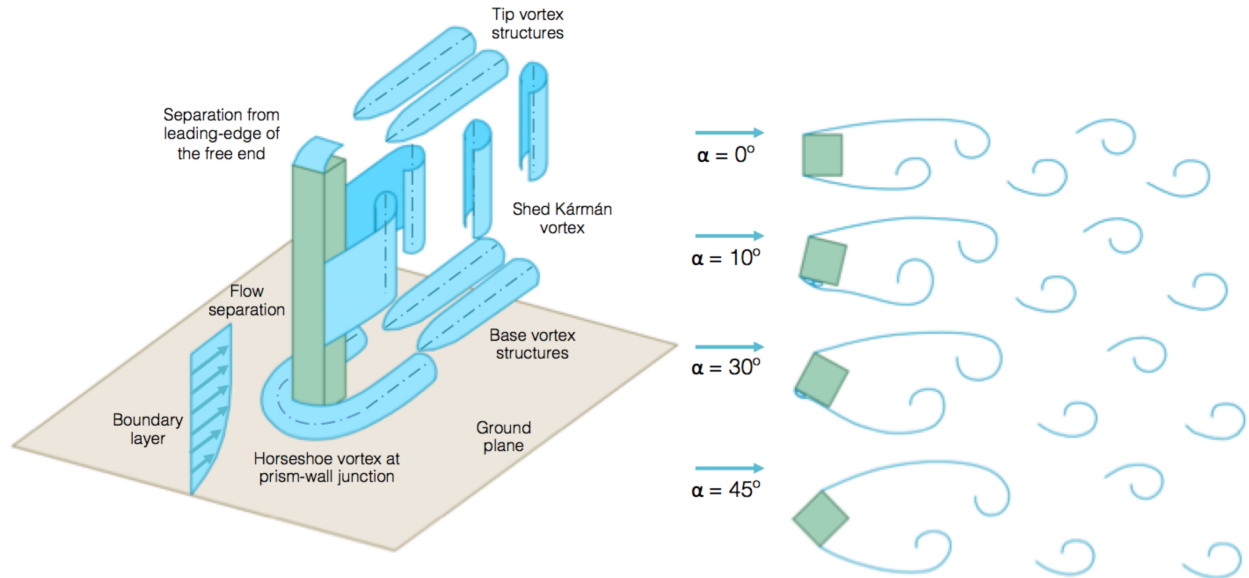


Figure 6. Structure of the wake region for a finite square prism (left). Structure of the wake region as a function of the angle of attack for a square prism (right). Adapted from: (McClellan and Sumner, 2004).

Different aspect ratios (height of the body over its width) also influence the wake structure, as shown in Figure 6. In addition to the Karman vortex street, two sets of stream-wise counter rotating vortex pairs form close to the tip and the base of a finite cylinder (McClellan and Sumner, 2014), increasing wake pressure recovery and reducing the drag force with respect to an idealized infinite prism (Nepf, 1999). This flow structure produces variations of c_D along the water column, with the lowest values of the coefficient at the extremes of the finite cylinder and larger values at the center (Ghisalberti and Nepf, 2004).

For slender sections parallel to the flow, such as flat plates, the drag is dominated by friction whereas form drag is more relevant for bluff objects. As a consequence, streamlining of a body can result in considerable drag reduction at high Re , but it can actually increase c_D for very small Reynolds numbers due to the enlargement of the area where shear forces act (Munson et al., 2013). The previously mentioned trends are summarized in Figure 7.

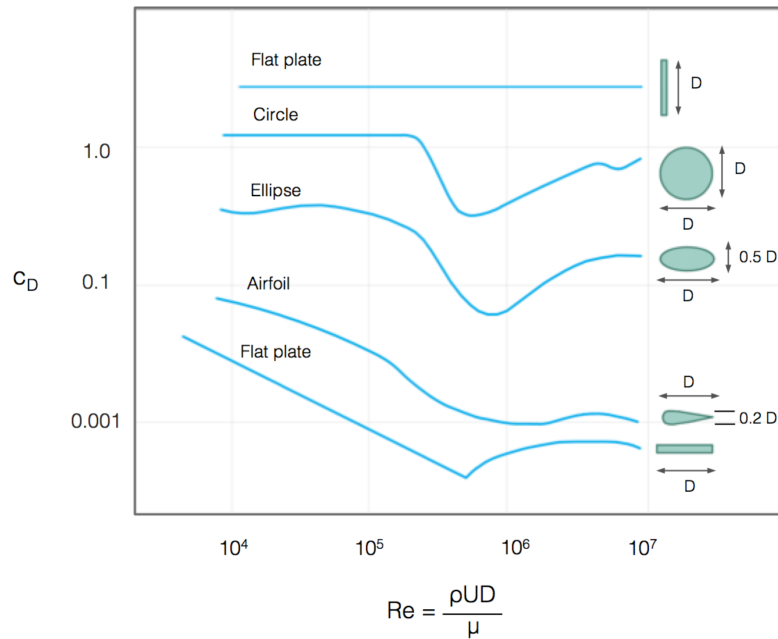


Figure 7. Character of the drag coefficient as a function of Reynolds number for objects with various degrees of streamlining, from a flat plate normal to the upstream flow to a flat plate parallel to the flow (two-dimensional flow). Adapted from: (Munson et al., 2013).

2.1.1.4. Effect of the angle of attack

Flow observations at steady flow past circular cylinders by Hoerner (1965) showed that in most cases the so-called cross flow principle is applicable and the drag coefficient can be considered independent of the angle of attack (Sumer and Fredsøe, 2006). When the angle of incidence of the flow with respect to a body, θ , is approximately larger than 35° the streamlines bend around the object in such a way that the flow incides perpendicular to it, as shown in Figure 8. Below this range of θ the streamlines do not bend and such assumption is not valid. The cross-flow principle has proven to be applicable in the subcritical range (i.e., $300 < Re < 3 \cdot 10^5$) and for post-critical flows (i.e., $3 \cdot 10^5 < Re < 1.5 \cdot 10^6$), whereas there is evidence that it may not hold true for the transcritical regime ($Re > 1.5 \cdot 10^6$) (Sumer and Fredsøe, 2006). Nevertheless, as it was explained in Section 2.1.1.3, those values are beyond the range of Reynolds' numbers associated to aquatic vegetation.

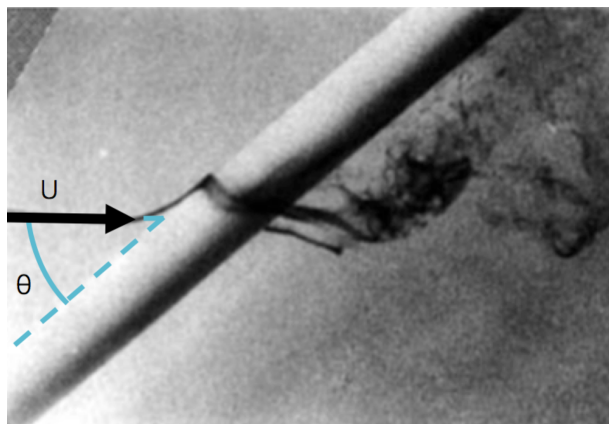


Figure 8. Bending of the streamlines as they approach a circular cylinder at oblique attack, θ . Adapted from: (Kozakiewicz et al., 1995).

According to the cross-flow principle, the friction drag coefficient c_S (parallel to the body) and the form drag coefficient c_N (perpendicular to it) for circular cylinders is given by:

$$c_S = f c_f \sin \theta \quad (2.4)$$

$$c_N = c_D \cos \theta \quad (2.5)$$

Where c_D is the drag coefficient for a body perpendicular to the flow, f is the ratio of the wet perimeter to the area of the cross section and c_f is a viscous friction coefficient.

Numerous measurements are available for flat strips perpendicular or almost parallel to the flow, but there is a limited number of experiments that analyse intermediate orientations (Dijkstra et al., 2006). Moreover, values of the drag coefficients obtained in experiments at a larger scale may not be applicable for smaller aquatic organisms because of differences in the structure of the boundary layer. Due to this uncertainty, Dijkstra et al. (2006) performed a series of experiments with rectangular plastic strips at different angles with the flow. Their dimensions were chosen to emulate the characteristics of eelgrass *Zostera Marina*. Horizontal and vertical forces on the strips were measured under a range of Reynolds numbers, resulting in the following fit:

$$c_S = 0.018 f \sin \theta \quad (2.6)$$

$$c_N = \min (2 \cos \theta + 0.1 \tan \theta, 2\pi) \quad (2.7)$$

Here c_N was limited to 2π for stability reasons, which is a characteristic value of flat plates at small angles of attack with the flow (Dijkstra et al., 2006).

2.1.2. Flow past a canopy of rigid elements in steady flow

The canopy drag coefficient varies with the density of the array, the Reynolds' number of the individual elements (based on their width) and their morphology (Nepf, 2011). Shear-layer scale turbulence (i.e. turbulence produced due to shear on top of the canopy) may sweep through the meadow and shift the transition to turbulence in the wake to lower flow velocities, with $Re < 200$ (Ghisalberti and Nepf, 2004). In analogy to isolated bluff bodies, c_D increases with decreasing Re when drag forces arise from viscous stresses. An increase in density generates a larger drag for this range (Nepf, 2011). When pressure drag dominates c_D reaches values of the order of 1. For the highest Reynolds' numbers its value decreases and falls below the value of isolated cylinders. Higher densities will result in lower c_D for this regime due to the interactions between the canopy elements (Nepf, 1999). The wakes of upstream bodies reduce the impact velocity in the neighbouring objects and incoming turbulences delay flow separation in downstream elements (Zukauskas, 1987), resulting in smaller drag forces.

2.1.3. Flow past individual rigid elements in oscillatory flow

Flow reversal under oscillatory flow results in boundary layer removal every wave period. The adjustment time-scale of the viscous and turbulent boundary layer is often sufficiently rapid (i.e. < 1 s) for steady conditions to develop even with fast changes in the background flow (Stevens and Hurd, 2001). Nevertheless, wake development depends on the ratio between the stroke of the motion and the geometry of the obstacle, which is often characterized by the Keulegan-Carpenter number, KC (Sumer and Fredsøe, 2006):

$$KC = \frac{u \cdot T}{D} \quad (2.8)$$

In which u is the maximum velocity, T is the period of the oscillatory flow and D is a length scale of the body. For very small KC separation may not even occur. When KC increases particles can travel larger distances relative to

the size of the object, resulting in separation and probably vortex shedding. As KC tends towards infinity, the flow in half a period resembles a steady current (Sumer and Fredsøe, 2006).

The values of the drag coefficient are usually higher under waves than in steady flow, since the vortices shed in one half-cycle are swept back and form pairs with successive vortices of opposite sign during the next half-cycle (Venugopal et al., 2005). The resulting vortex pairs usually convect away from the body at an angle with respect to the flow that varies with KC (Graham, 1980). Sharp-edged cross sections are associated with flow separation at the leading edges for very low KC and consequently display larger values of c_D in this range compared to smoother circular shapes, as shown in Figure 9.

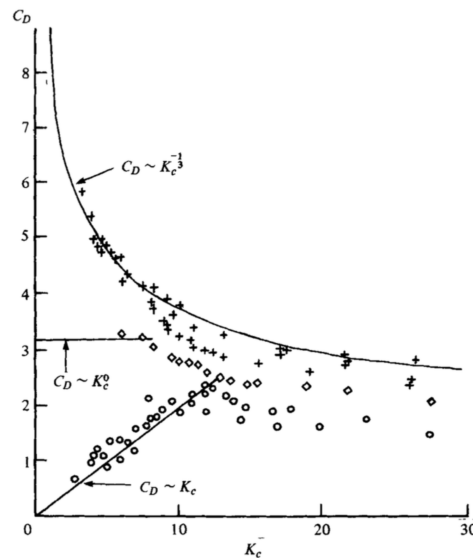


FIGURE 1. Drag coefficient at low Keulegan-Carpenter numbers. +, Flat plate (Singh 1979); ◇, square cylinder (Singh 1979); ○, circular cylinder (Sarpkaya 1975; Singh 1979).

Figure 9. Drag coefficients for low values of the Keulegan-Carpenter number. Source: (Graham, 1980).

There are two additional contributions to the in-line force (i.e., resultant force in the direction of the flow) besides the drag for oscillatory flows. When an immersed body is set into motion due to the action of pressure, the mass of fluid in the immediate neighbourhood of the object is also accelerated due to the no-slip condition and follows its movement (Sumer and Fredsøe, 2006). The volume of displaced water is denoted as hydrodynamic mass and causes additional resistance against the motion. The second contribution is the Froude-Krylov force, which arises from the unsteady pressure gradient that accelerates the fluid past an object (Batchelor, 2000).

The Morison formulation was developed for the calculation of force distributions exerted on piles by surface waves (Morison et al, 1950) and it has also been applied to define the external forces acting on a blade (Luhar and Nepf, 2016; Denny et al. 1998). Assuming that the velocity and acceleration of the body are negligible compared to that of the fluid, the total force per unit length is written as:

$$dF = \frac{1}{2} \rho c_D w u^2 + \rho c_a A \frac{du}{dt} + \rho A \frac{du}{dt} \quad (2.9)$$

The first term in equation (2.9) is the drag force, previously defined in Section 2.1.1.2 in which w is the width of the object. The second term corresponds to the hydrodynamic mass force and the third term represents the Froude-Krylov force, where A is the cross-sectional area of the body, du/dt is the acceleration of the fluid, ρ is the fluid density and c_a is the added mass coefficient. The two last terms are often combined using the inertia force coefficient c_M , defined as:

$$c_M = c_a + 1 \quad (2.10)$$

Resulting in:

$$dF = \frac{1}{2} \rho c_D w u^2 + \rho c_M A \frac{du}{dt} \quad (2.11)$$

The inertial forces are predominant in the range of relatively small KC numbers, while drag forces dominate at large KC numbers, where inertial forces are constant (Okajima et al., 1998). The application of equation (2.11) relies on the definition of the empirical coefficients c_D and c_M . The inertia coefficient is closely related to the flow volume around the body (Venugopal et al., 2005) and can also be related to the flow properties, according to relationships that depend on the shape of the cross-section, as shown in Figure 10.

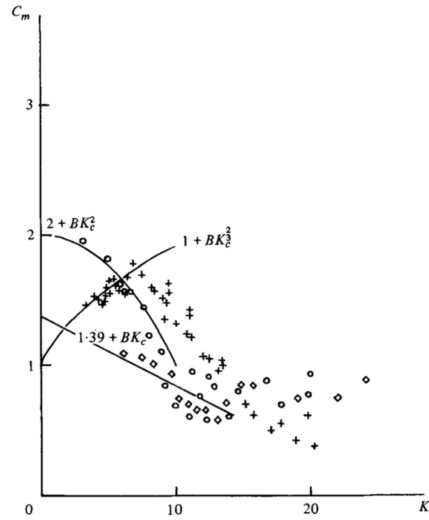


FIGURE 8. Inertia coefficients at low Keulegan-Carpenter numbers. +, Flat plate (Singh 1979); ◇, diamond square (Singh 1979); ○, circular cylinder (Singh 1979).

Figure 10. Inertia coefficients for low values of the Keulegan-Carpenter number. Source: (Graham, 1980).

In the case that the relative motion of the body with respect to the flow is not negligible, the Morison equation can be written as:

$$dF = \frac{1}{2} \rho c_D w (u - u_v)^2 + \rho c_M A \frac{du}{dt} + \rho c_a A \frac{du_v}{dt} \quad (2.12)$$

In which u_v and du_v/dt are the velocity and the acceleration of the body in the flow direction.

2.1.4. Flow past individual flexible bodies

2.1.4.1. Reconfiguration as an adaptive response to hydrodynamic loads

Plants seek to maximize their surface area to capture the most sunlight as well to facilitate the mass exchange with the surrounding fluid (Harder et al. 2004). Nevertheless, an upright posture in the water column exposes them to higher hydrodynamic forces (Stewart, 2004). Aquatic organisms have evolved a variety of strategies to survive the large loads imposed on them, such as large waves (Koehl, 1984). One of those mechanisms is drag reduction by elastic reconfiguration (de Langre et al., 2012). By bending and twisting plants reduce their projected area perpendicular to the flow, and, on the other hand, they become more streamlined, diminishing the form drag (Vogel, 1994). Laboratory experiments by Gosselin et al. (2010) showed that the effect of streamlining

is prominent at the onset of reconfiguration whereas area reduction dominates in the regime of large deformations. Moreover, bending pushes aquatic vegetation closer to the ground, where the flow velocities are lower (Etnier and Vogel, 2000). For instance individuals of certain species may avoid overcritical loads by escaping into the benthic boundary layer (Harder et al, 2004).

By swaying with the ambient flow organisms decrease their relative velocities and accelerations with respect to the fluid (Koehl, 1984). However, the effectiveness of such stress-reducing mechanism is conditioned by the morphology of the plants and their natural environment. Aquatic organisms gain momentum as they follow the fluid. At some point in their travel, plants are halted by the elastic attachment to the stationary substratum, which results in rapid deceleration and the imposition of an inertial force on their mass (Denny et al., 1998). Long and flexible organisms in rapidly accelerating flows (for instance under breaking waves) would experience strong inertia forces twice (once shoreward and once seaward) every wave cycle (Harder et al., 2004). In contrast, stiffer and smaller plants would not move substantially with the flow, which would result in lower inertia forces. Moreover, loads that result from the water's acceleration are more efficiently minimized by a small overall size rather than area reduction, since inertia forces scale with the volume, as it can be observed in equation (2.12) (Gaylord and Denny, 1997). Reconfiguration is a more efficient adaptive response in habitats associated with a less violent water motion, where drag is the main form of mechanical loading (Gaylord, 2000).

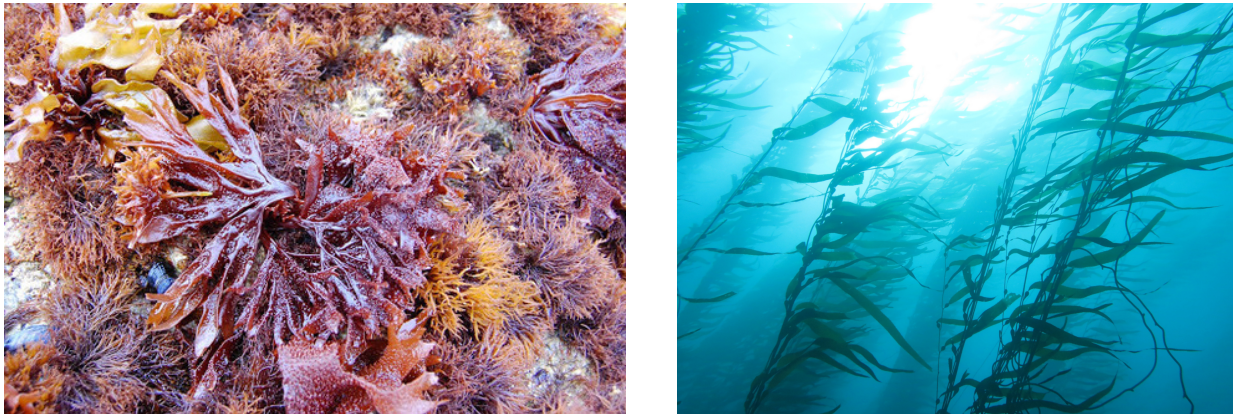


Figure 11. The left picture shows a specimen of *Mastocarpus papillatus*, characteristic of intertidal habitats. It quickly reconfigures to a more streamlined position and remains aligned with the flow during the passage of waves. Its small size minimizes inertia forces associated with the strong accelerations typical of its natural environment. The right photography portrays a giant kelp (*Macrocystis pyrifera*), which extends from depths of 30 m or more to the surface. They can be found in subtidal areas, where they are exposed to comparatively less violent hydrodynamic loads and sway with the fluid motion for most of the wave period (Gaylord and Denny, 1997).

The ability of plants to follow the fluid is conditioned by their length in relation to the size of wave-driven orbits (Luhar and Nepf, 2016). Relatively short organisms (due to their reduced dimensions or under higher waves in shallower water) quickly readjust their shape and reach their maximum deflection with the initial wave impact, remaining extended during most of the period (Gaylord and Denny, 1997). Under such conditions, the relative velocities and accelerations approach the values for rigid vegetation and drag-reduction is only due to streamlining (Bradley and Houser, 2009). A longer plant (or the same aquatic organism exposed to smaller waves in deeper water) can continue to move over a larger fraction of the wave cycle. Thus, the upper part of the plant can follow the flow whereas drag forces are mainly generated at its base (Mullarney and Henderson, 2010; Luhar and Nepf, 2016).

2.1.4.2. Modelling plant reconfiguration

Assuming that an organism extends in the direction of the flow (and that its velocities and accelerations are considerably smaller than those of the fluid) the use of a constant drag coefficient or a constant relevant area in

equation (2.11) would yield to an expected increase in the drag with the velocity squared (Denny et al., 1988). In practice the increase would be lower (de Langre et al., 2013), since as presented in the previous section, the overall shape of a flexible biological body changes under different flow regimes (Harder et al., 2004). Several options have been suggested in the existing literature to accommodate such effects:

- A number of authors (Dalrymple et al., 1984; Kobayashi et al., 1993; Mendez and Losada, 2004) have introduced the use of variable shape factors, c_D , that change with the fluid velocity while keeping the area constant (Harder et al., 2004). The effective drag coefficient is often empirically related to the Keulegan-Carpenter number or the Reynolds number, defined in terms of a length scale of the geometry (usually the width of the cross-section). This type of relationships has proven to provide reliable estimates for individual rigid cylinders. Nevertheless, drag forces in a flexible canopy depend on blade bending. Without including the effects of vegetation motion in the definitions of Re and KC , these dimensionless numbers only represent the strength of the flow. Since different species (with different mechanical properties) will react differently to the same flow conditions the fitting parameters will change in each field site (Zeller et al., 2014).
- A second option is to regard the relevant area as varying with the velocity. Losada et al. (2016) used the concept of deflected length, h , to compare the bending of *Spartina Anglica* and *Puccinellia Maritima* under waves:

$$\frac{h}{l} = \int_0^l \cos \theta \, ds \quad (2.13)$$

Where l is the total length of the blade, h its effective height, ds is a segment of the blade and θ is the angle that it forms with the vertical direction. Luhar and Nepf (2011) introduced the concept of effective length, l_e , which besides accounting for area reduction also incorporates the effect of streamlining. Assuming that the cross-flow principle is applicable, l_e is defined as:

$$\frac{l_e}{l} = \int_0^l \cos^3 \theta \, ds \quad (2.14)$$

In their study, they developed empirical relationships for unidirectional flows that related the effective length with the Cauchy number, Ca , a dimensionless parameter commonly used in the study of fluid-structure interactions (Blevins, 1984). Ca characterizes the relative importance of the bending stiffness with respect to the hydrodynamic loading and can be written as:

$$Ca = \frac{1}{2} \frac{\rho c_D w u^2 l^3}{EI} \quad (2.15)$$

In which u is the flow velocity, c_D is the drag coefficient, ρ is the fluid density, l is the length of the blade, w its width and EI its flexural rigidity. In a latter publication in 2016, they derived analogous expressions for oscillatory flows where the effective length was also a function of a second parameter, the ratio of the blade length to the orbital excursion (L).

- Another possibility is the use of expressions derived from the second power relationship between drag and velocity, through the inclusion of the Vogel exponent, b , in the quadratic law defined in Section 2.1.1.2. (de Langre, 2008):

$$F_D = \frac{1}{2} c_D \rho u^{2+b} A \quad (2.16)$$

Alben et al. (2002) developed a simplified model in which a fibre was represented as an elastic beam loaded by the pressure drag, which was balanced by the tensile and bending forces in the material. The most rigid fibres displayed a quadratic growth of the drag with the flow speed ($b = 0$). For the most flexible blades the scaling between form drag and velocity was almost linear ($b = -2/3$). The Vogel exponent varied between both extremes over a significant range of Cauchy numbers (Gosselin et al., 2010). Besides, aquatic vegetation can be positively buoyant; seagrass blades have gas-filled lacunae and kelps and other macroalgae have gas filled floats called pneumatocysts (Stewart, 2006). In those cases buoyancy acts a restoring mechanism and pushes the organisms to upright positions. Its contribution results in a sub-linear increase of the pressure drag with the flow speed (Luhar and Nepf, 2011). Faster flows could result in alignment of the fibre with the flow and dominance of skin friction. This would result in $u^{3/2}$ scaling ($b = -1/2$) instead of a near-linear growth of the drag (Alben et al., 2002).

When the motion of the plant is significant, accurate predictions of the vegetation-induced forces require modelling the dynamics of the plants. There no universally accepted methodology to account for vegetation motion (Luhar and Nepf, 2016). A brief review of some of the existing models is presented below.

2.1.4.3. Modelling plant motion

Several simple models for wave-forced vegetation motion have been proposed in the literature. Most of them are based on a balance between the hydrodynamic forces and the restoring forces in a single plant, with different simplifications of key aspects of the system. Elastic forces and buoyancy tend to keep vegetation straight. Nevertheless, the inclusion of rigidity makes the equations governing blade motion more strongly coupled and more difficult to solve (Zeller et al., 2014). As a consequence, many numerical studies have focused on cases where the flexibility of the stems was considered negligible or assumed the vegetation to be infinitely rigid. For instance, Abdelrhman (2007) developed a model for a seagrass blade under steady flow in which buoyancy was the main restoring force and the blade had no stiffness. Mullarney and Henderson (2010) derived an analytical method to reproduce the motion of a single stem exposed to oscillatory flow by linearizing the Euler-Bernoulli equation, under the assumption that the plant experiences small deflections. Nevertheless, the model did not include the effect of inertia and buoyancy. Luhar and Nepf (2011) covered intermediate rigidities in a latter study, but their model was limited to steady flow. Zeller et al. (2014) combined numerical modelling and experimental observations to simulate finite amplitude motions incorporating both drag and inertia forces. Luhar and Nepf (2016) developed a model to reproduce the motion of a stem exposed to oscillatory flow, assuming that it is inextensible and that it moves without twisting. The model results were compared to stem positions and forces measured during a series of laboratory experiments.

Different species may be associated with different schematizations and simplifications. For instance, the feather boa kelp, *Egregia menziesii* is so flexible that for small lateral motions the restoring force is negligible, and the effect of stiffness is only significant when the deflection is larger than a certain threshold. A larger number of branches or additional structural elements would increase the complexity of the system. For terrestrial vegetation such problem has been addressed by modal superposition, adding up the solution of the oscillator equation for the different components of the plant (de Langre, 2008).

2.1.5. Effects of a canopy in the hydrodynamics

The effect of one single plant on a steady flow can be considered negligible. Nevertheless, the cumulative effect of the elements of a meadow results in significant drag, which causes redirection of the fluid over the top of the canopy and a decrease of the water velocity within the vegetated region (Nepf, 1999). As a result there is strong velocity shear and greatly increased turbulent intensities at the upper part of the plants relative to undisturbed flow (Gambi et al., 1990). If the momentum absorption by the canopy is high enough, the resulting velocity profile

resembles that of a mixing layer, with two regions of constant velocity separated by an inflection point (Ghisalberti and Nepf, 2008). Such a point makes the flow susceptible to Kelvin-Helmholtz instability, i.e. wave instabilities that grow and roll up into vortices that pass on top of the meadow at a fixed frequency (Holmes et al., 1996). These coherent structures can be identified as peaks in the velocity spectrum. When the flexibility of the vegetation is high enough, the oscillations in the streamwise velocity trigger a progressive, synchronous, low amplitude waving of the plants; the so-called monami (Ghisalberti and Nepf, 2002).

There is also energy dissipation at the stem-scale within the canopy. The energy of the mean flow is converted into turbulent kinetic energy within the stem wakes when their flow structure is turbulent. When the wakes are laminar, the energy is directly dissipated into heat through viscous drag (Nepf, 1999). The latter mechanism may be dominant for the case of submerged flexible vegetation that bends in response to hydrodynamic loads (Nikora and Nikora, 2007). In principle, the determination of turbulence production would require using direct numerical simulations to fully resolve the turbulence (Zeller et al., 2014). A more simple approach estimates turbulence generation by parameterizing the forces between the vegetation and the fluid using the quadratic law.

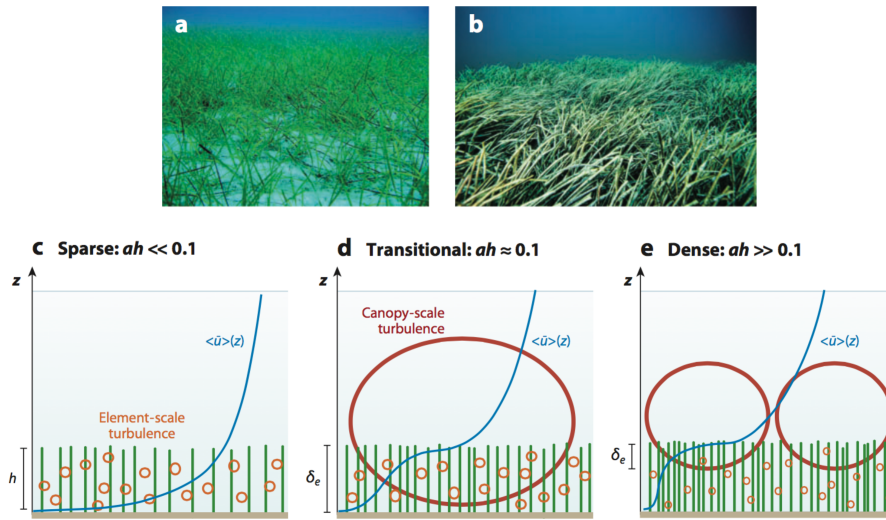


Figure 12. Effect of canopy density on the vertical profile of the mean flow. The upper plots show natural aquatic vegetation with different densities; (a) Seagrass *Cymodocea nodosa* at low stem density and (b) the seagrass *Posidonia oceanica* at high stem density. The lower plots represent the most important turbulent structures for different densities expressed in terms of ah , where a is the projected plant area per unit volume and h is the water depth. Source: (Nepf, 2012)

Energy removal under oscillatory flows results in wave height attenuation. Such removal accomplished by the work done on the fluid by aquatic plants. Mathematically, the rate of work per unit length is defined as the product between the relative velocity between the ambient flow and the vegetation ($u - u_v$) times the force that the plants applies to the fluid in the direction of the flow, dF , as shown in equation (2.9). The total work is obtained by integrating over the height of the stems, h_v . Physically, it represents how much the organisms resist the motion of the fluid, consequently removing energy from the waves (Zeller et al., 2014).

$$W = \int_0^{h_v} dF (u - u_v) dz \quad (2.17)$$

The energy dissipation over the wave phase is given by:

$$\bar{W} = \frac{1}{T} \int_0^T W dt \quad (2.18)$$

Where W is the instantaneous work and T is the wave period.

Observations and theoretical studies have shown that the periodic flow generated by surface waves is less dampened within a canopy compared to a unidirectional current of the same magnitude (Lowe et al., 2005; Luhar et al., 2010; Luhar et al., 2013). Besides this, the lower in-canopy velocities are more easily reversed in comparison with the stronger upper flow and subsequently lead it in phase, in a similar manner to the streaming phenomena within the benthic boundary layer (Döbken, 2015).

Both laboratory experiments and field measurements have suggested that waves induce a mean mass drift in the direction of wave propagation within submerged canopies. The magnitude of this current was found to be from 20% up to 40% of the near bed oscillatory velocities within the meadow (Luhar et al., 2010; Luhar et al., 2013; Pujol et al., 2013; Ma et al., 2013). Döbken (2015) related the generation of the streaming to the vertical orbital velocity of fluid particles on top of the vegetation. Fluid parcels penetrate in the meadow with the backward motion, which produces a higher drag and flow reduction compared to the forward motion under the wave crest. In a period-averaged sense, the result is a residual drift in the wave propagation direction. Observations by Pujol et al. (2013) showed that for the case of emergent vegetation, where there was no discontinuity in the drag along the water column, the drift was not present. The degree of penetration of the streaming depends on the characteristics of the vegetation such as the height of the canopy, its density and the mechanical properties of the individual elements (Döbken, 2015; Pujol et al., 2013). Luhar et al. (2010) proposed that the induced drift is responsible for the asymmetry found in plant posture under waves, with the stems lying in the propagation direction under the crest and being more upright during the trough. It was hypothesised that the larger exposed area under the wave trough could result in a larger drag for the negative oscillatory velocities and consequently further reinforce the streaming.

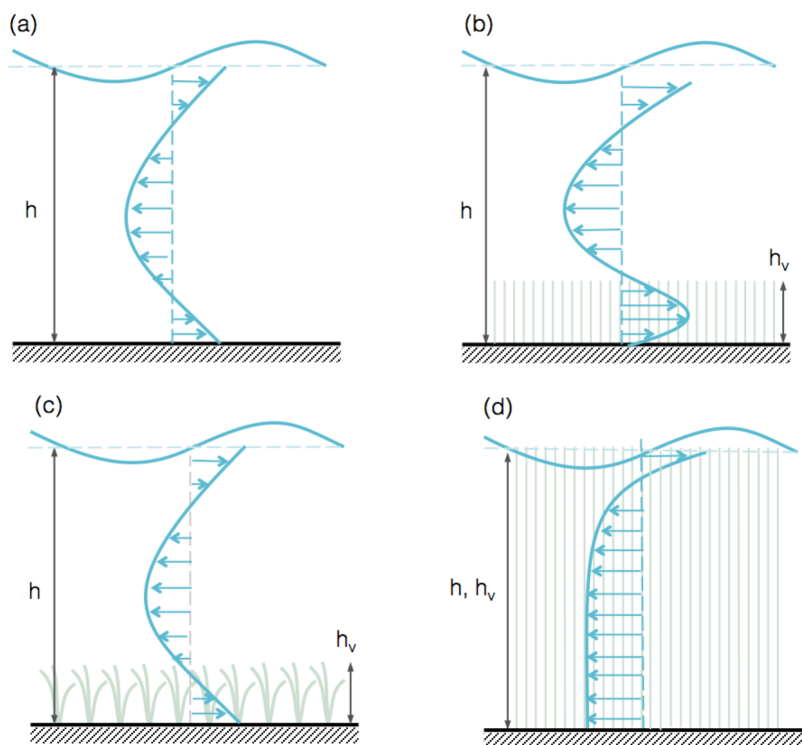


Figure 13. Eulerian velocity profile under pure oscillatory flow for three seagrass structures and two height ratios, h_v/h , where h_v is the height of the canopy and h is the water depth. Solid lines represent the mean vertical profile (a) without vegetation; (b) submerged rigid vegetation, which shifts the negative velocities upwards and produces streaming within the canopy (c) flexible submerged vegetation and (d) emergent rigid vegetation. Luhar et al. (2010) also found a current in the direction of propagation inside the canopy for case (c). Such differences were attributed to the wavemaker and the amplitude of the waves in the experiments. Source: (Pujol et al., 2013)

Dissipation induced by aquatic plants is not uniform across all frequencies; vegetation has been found to behave a low-pass filter, producing higher attenuation of short period waves (Manca et al., 2012; Jadhav et al., 2013). Lowe et al. (2007) explained such phenomenon in terms of the higher ability of flows induced by high frequency waves to penetrate into the vegetation, resulting in larger drag forces and higher wave height reduction for such components. Bradley and Houser (2009) suggested that the increased attenuation for smaller periods waves was also due to the changes of the relative motions of seagrasses with frequency and that this mechanism may be more important under low-energy conditions. They also observed that although vegetation may sway with the flow, it does not move passively for most periods.

The use of numerical models to reproduce plant motion has provided new insights to the stem response to oscillatory flows. For instance, Mullarney and Henderson (2010) modelled the motion of the sedge *Schoenoplectus americanus* under waves and compared it with field observations. They found that waves with high frequencies excited rigid vegetation modes that produced considerable dissipation. For the case of short waves, reducing the period resulted in a decrease of the effective stiffness and less attenuation. Zeller et al. (2014) also obtained higher dampening of high-frequency waves, which they associated with the ability of plants to react to changes in the flow and to move more in phase with it under long waves. Within a wave spectrum, seagrasses were observed not to move in phase with the higher peak frequency and appeared to follow less-energetic waves at a lower frequencies, resulting in less dissipation for such wave components (Bradley and Houser, 2009).

When multiple plants are combined in a canopy, the response of the individual stems is very sensitive to the arrangement of the elements and to blade-blade interactions. For instance, the collapse of the elements at the leading edge of a marsh produces a more even distribution of the hydrodynamic forces, higher stability of the community and lower wave attenuation (Fonseca et al., 2007).

2.2. Wave hydrodynamics

2.2.1. Linear wave theory

The small amplitude or linear wave theory is the simplest theory for two-dimensional progressive gravity waves. The theory is developed linearizing the equations that define the free surface boundary conditions, under the assumption that the amplitude of the wave is small compared to both the wavelength and the water depth. Its accuracy decreases for high waves at sea or waves propagating in nearshore shallow areas, where these conditions do not strictly hold (Sorensen, 2006). The various wave characteristics (i.e., surface elevation, particle kinematics, wave celerity) are derived from a velocity potential that satisfies both the requirement for irrotational flow and the boundary conditions. The horizontal and vertical components of the velocity of a water particle are defined by the following expressions:

$$u(x, z, t) = \frac{\pi H}{T} \frac{\cosh k(z+h)}{\cosh kh} \cos(\omega t - kx) \quad (2.19)$$

$$w(x, z, t) = \frac{\pi H}{T} \frac{\sinh k(z+h)}{\sinh kh} \sin(\omega t - kx) \quad (2.20)$$

Where H is the wave height, T is the wave period, k is the wave number, ω is the angular velocity, t represents time, x is the horizontal position of the particle, h is the water depth and z is the elevation in the water column. The different parameters and the reference system are shown in Figure 14.

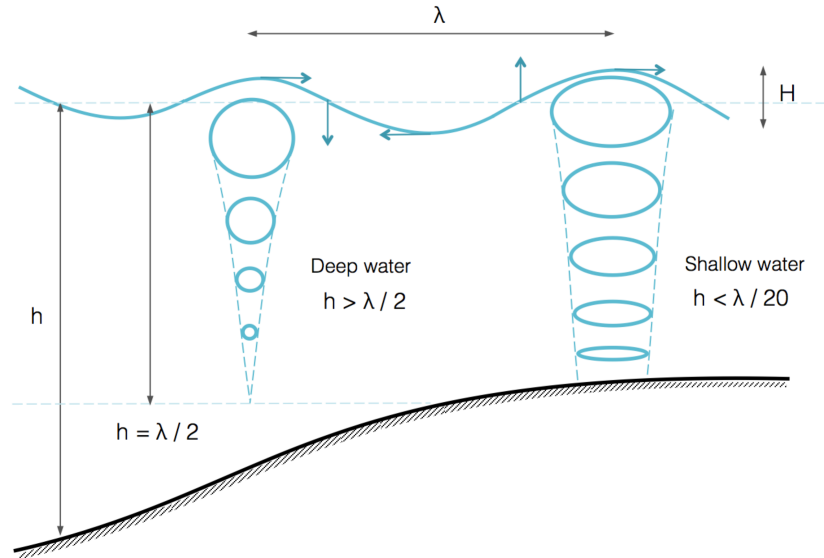


Figure 14. Surface waves propagating from deep-water conditions (orbital motion), towards shallow water conditions (elliptical motion). The criterion depends on the wavelength compared to the still water depth, h . Adapted from: (Döbken, 2015).

According to linear wave theory, the water surface is approximated as a sinusoidal wave and fluid particles describe closed elliptical paths under the free surface, with the horizontal and vertical velocities being 90° out of phase. The orbits tend to circles in deep water whereas in shallow water they degenerate into a back and forth motion along the bottom (Svendsen, 2006).

2.2.2. Undertow

The particle trajectories are only closed in the first order approximation. The contributions of higher order terms produce a larger displacement of the fluid particles in the direction of wave propagation than in the backward motion and result in a residual mass flux. The mass transport by waves can be obtained integrating the trajectory of the particles over a wave cycle, using a Lagrangian description of the motion. The vertical profile of the Lagrangian drift can be written as (Phillips, 1977):

$$u(z) = \omega k a^2 \frac{\pi H \cosh 2k(z+h)}{T \cdot 2 \sinh^2 kh} \quad (2.21)$$

In the surf zone, due to the presence of a confined boundary, the mean mass flow over the wave period must be equal to zero. This results in a return current that is equal to the amount of water carried shoreward by the breaker, known as the undertow (Svendsen, 2006). Within the breaking zone there is a vertical imbalance of the forces, which results in the mass transport by waves being dominant in the upper part of the water column and an offshore return flow underneath (Brown et al., 2014). Out of the surf zone (for instance in the inner shelf), the Eulerian return flow is defined in magnitude by the velocity profile given by equation (2.21) but directed in the offshore direction, resulting in a piecewise compensation of the drift (Monismith et al., 2000).

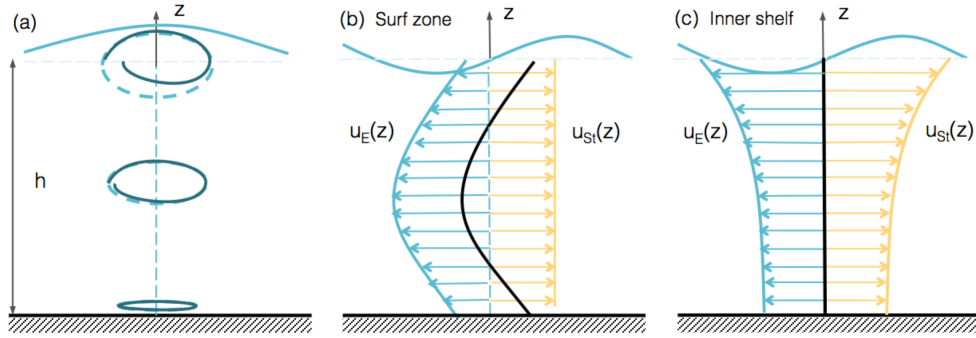


Figure 15. (a) Water particle paths over a wave period. The full curves are the paths in second order Stokes wave motion, the dashed lines the equivalent linear wave solution. Adapted from: (Svendsen, 2006). (b) Structure of the mean flow in the surf zone. The Stokes drift tends to a depth-uniform profile and the undertow is parabolic. There is an integral compensation, but a vertical imbalance (c) Structure of the mean flow in the inner shelf, where the Lagrangian Stokes drift and the wave-driven Eulerian flow cancel at every point. Adapted from: (Brown et al., 2014).

2.2.3. Stokes second order theory

Real waves at intermediate water deviate from the sinusoidal shape assumed in linear wave theory. They are characterized by shorter and higher crests and longer and shallower troughs (Sorensen, 2006). Such differences are accentuated in shallow water, where waves grow in size as they shoal. The second order Stokes theory accounts for the non-linearities by introducing a forced oscillation that propagates at the same speed than the main harmonic and with a frequency twice as large, as shown in Figure 16. The additional contribution to the velocity associated with such component is given by:

$$u_2(x, z, t) = \frac{3}{16} c(kH)^2 \frac{\cosh 2k(z+h)}{\sinh^4 kh} \cos 2(\omega t - kx) \quad (2.22)$$

$$w_2(x, z, t) = \frac{3}{16} c(kH)^2 \frac{\sinh k(z+h)}{\sinh^4 kh} \sin 2(\omega t - kx) \quad (2.23)$$

Here c is the wave celerity and u_2 and w_2 are the horizontal and vertical velocities of the higher harmonic, which add up to those calculated using small amplitude theory. The inclusion of non-linearities in the velocity field produces asymmetries in its amplitude over the wave period, with higher velocities under the wave crest and lower velocities during the trough.

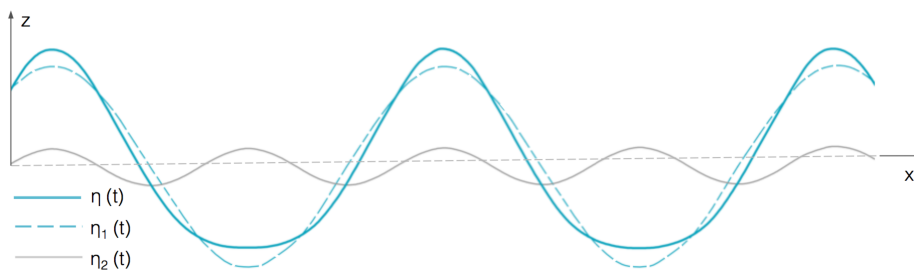


Figure 16. Second order Stokes wave. The Stokes wave, $\eta(t)$, is the result of the addition of main component $\eta_1(t)$ and the non-linear term $\eta_2(t)$. Adapted from: (Borsen, 2007)

3. Model

3.1. Dynamic blade model

The vegetation model, Dynveg, describes the two-dimensional motion of a blade, excluding elongation or folding of the plant (Dijkstra and Uittenbogaard, 2010). In order to reproduce large deflections the blades are discretized in a number of segments defined by the coordinate s , measured along the plant from $s = 0$ at the base to $s = s_{max}$ at the tip, as shown in Figure 17. The angle between the stems and the vertical direction is defined as θ . The coordinate n represents the direction perpendicular to the leaf.

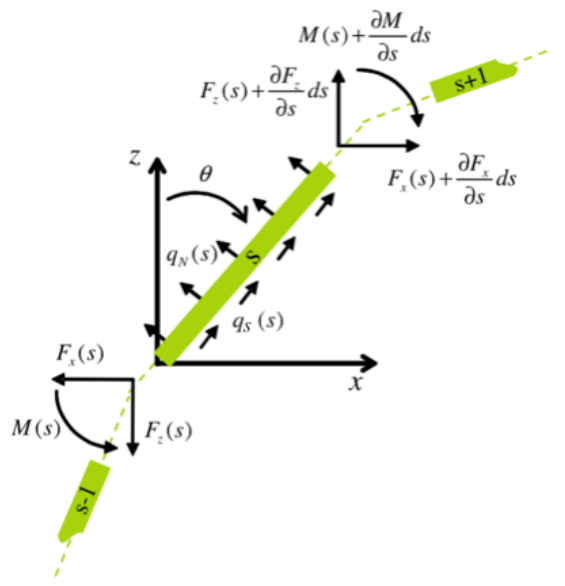


Figure 17. Balance of forces in a segment s . Source: (Dijkstra and Uittenbogaard, 2010)

For each of the partitions the balance of forces is given by:

$$\rho_t a \frac{\partial^2 x}{\partial t^2} = q_x + \frac{dF_x}{ds} \quad (3.1)$$

$$\rho_t a \frac{\partial^2 z}{\partial t^2} = q_z + \frac{dF_z}{ds} + g(\rho_v - \rho_w) \sin(\theta) \quad (3.2)$$

Where q_x and q_z are the distributed external forces along the leaf and F_x and F_z are the internal force components. The left hand terms represent the acceleration of the plant ($\partial^2 x / dt^2$ and $\partial^2 z / dt^2$), with a being equal to the cross-sectional area of the blade. The motion of the surrounding virtual water mass is included through the density, ρ_t :

$$\rho_t = \rho_v + c_a \rho \quad (3.3)$$

In which ρ_v is the density of the stem, ρ is the fluid density and c_a is the added mass coefficient. The distributed loads consist of both the drag and the inertia forces and are defined by equations (3.4)-(3.7). The inertia part of the loads corresponds to the Froude-Krylov force, resulting from the horizontal and vertical acceleration of the fluid (\dot{u} and \dot{w} respectively):

$$q_{x,I} = c_M \rho a \dot{u} \quad (3.4)$$

$$q_{z,l} = c_M \rho a \dot{w} \quad (3.5)$$

Here c_M is the inertia coefficient, previously defined in equation (2.10). The drag force is defined in the local coordinate system of the blade (s, n):

$$q_s = \frac{1}{2} \rho b c_S |u - \dot{x}| u_s \quad (3.6)$$

$$q_n = \frac{1}{2} \rho b c_N |u - \dot{x}| u_n \quad (3.7)$$

Where b is the width of the plant, u_s and u_n are the velocities parallel and perpendicular to the leaf and the drag coefficients c_S and c_N are defined using the empirical expressions presented in Section 2.1.1.4. The Cartesian and the local coordinates can be related through the transformation matrix Ω :

$$\Omega = \begin{bmatrix} \sin \theta & -\cos \theta \\ \cos \theta & \sin \theta \end{bmatrix}$$

The internal forces can be expressed as a function of hydrodynamic load and the plant acceleration by rearranging equations (3.1) and (3.2):

$$\frac{dF_x}{ds} = \rho_t a \frac{\partial^2 x}{\partial t^2} - q_x \quad (3.8)$$

$$\frac{dF_z}{ds} = \rho_t a \frac{\partial^2 z}{\partial t^2} - q_z - g(\rho_v - \rho_w) \sin(\theta) \quad (3.9)$$

On the other hand, they are also coupled to the internal moment M :

$$\frac{dM}{ds} = \frac{dx}{ds} F_z - \frac{dz}{ds} F_x \quad (3.10)$$

The internal moment is related to the leaf's curvature $\partial\theta/ds$ through the following equation:

$$M = EI \frac{\partial\theta}{ds} \quad (3.11)$$

Since the leaf does not elongate, the Cartesian coordinates can be defined as a function of the deflection angle. This allows expressing the kinematic properties of the blade in terms of the angle θ and its derivatives:

$$\frac{dx}{ds} = \sin(\theta) \quad (3.12)$$

$$\frac{dz}{ds} = \cos(\theta) \quad (3.13)$$

The tip of the plant is defined as unloaded (both forces and moments are equal to zero) and the root is fixed to the bed but allowed to rotate. Equations (3.1)-(3.13) can be combined into one integro-differential equation, which together with the boundary conditions, closes the problem and allows determining the only unknown, $\theta(s)$.

The governing equation can be written as:

$$\begin{aligned} \frac{\partial}{\partial s} \left(EI \frac{\partial \theta}{\partial s} \right) \Big|_s &= -\cos(\theta) \int_s^{smx} q_x(s') ds' + \sin(\theta) \int_s^{smx} q_z(s') ds' \quad (3.14) \\ &+ \int_s^{smx} \rho_t a(s') \int_0^{s'} \cos\{\theta(s) - \theta(s'')\} \ddot{\theta}(s'') ds'' ds' + \int_s^{smx} \rho_t a(s') \int_0^{s'} \sin\{\theta(s) - \theta(s'')\} \dot{\theta}^2(s'') ds'' ds' \\ &- \cos(\theta) \int_s^{smx} c_m \rho_w a \frac{du(s')}{dt} ds' + \sin(\theta) \int_s^{smx} c_m \rho_w a \frac{dw(s')}{dt} ds' \end{aligned}$$

3.2. Numerical implementation

The governing integro-differential equation was expressed in a dimensionless form by dividing it by the flexural rigidity of the blade, EI , and multiplying it by the leaf length, S , resulting in (Uittenbogaard, 2006):

$$\begin{aligned} \alpha \int_s^{s_{max}} \int_0^{s'} \ddot{\theta}(s'') ds'' ds' + \beta \int_s^{s_{max}} \int_0^{s'} \dot{\theta}(s'') ds'' ds' - \gamma \frac{\partial \theta}{\partial s} \Big|_s \\ = (\delta - \eta) \int_s^{s_{max}} 1 ds' \end{aligned} \quad (3.15)$$

Where $\alpha, \beta, \gamma, \delta$ and η are dimensionless coefficients, defined below:

$$\alpha = \frac{\rho_t a S^4}{EI \tau^4} \quad (3.16)$$

$$\beta = \frac{\frac{1}{2} \rho_w c_D w S^4 |u|}{EI \tau} \quad (3.17)$$

$$\gamma = 1 \quad (3.18)$$

$$\delta = \frac{\frac{1}{2} \rho_w c_D w S^3 |u| u}{EI} \quad (3.19)$$

$$\eta = \frac{(\rho_w - \rho_v) g a S^3}{EI} \quad (3.20)$$

The equation was also discretized both in space and time in order to formulate a linear set of equations given implicitly in term of θ^{n+1-j} , with new time level θ^{n+1} ($j = 0$) and previous time levels θ^n, θ^{n-1} , corresponding to $j = 1, 2$. The leaf was subdivided in $smax$ segments of length Δs . The orientation of each segment θ_s was defined at its center. The integrals were discretized in space by the application of the mid point rule. The spatial derivatives were approximated by the second order central operator. The magnitude of the relative velocity in the drag, $|u - \dot{x}|$, was defined in the previous time. The square of the angular frequency $\dot{\theta}^2$ was considered as the product of the value of the previous timestep, $\dot{\theta}^n$, times the result of the new timestep, $\dot{\theta}^{n+1}$. $\dot{\theta}$ was defined from the segment angle θ considering it slightly advanced in time (Uittenbogaard, 2006):

$$\dot{\theta}^n = \theta^{n+1} - \theta^n \quad (3.21)$$

The angular acceleration term was approximated by three temporal time levels, according to:

$$\ddot{\theta}_s^n = \theta_s^{n+1} + \theta_s^{n-1} - 2\theta_s^n \quad (3.22)$$

Lastly, the spatial derivative of θ was decomposed between the timesets θ_s^{n+1} and θ_s^{n-1} using the theta-method. The choice of the coefficient depends on the problem investigated; when the focus is the shape of the plant and there is not interest in smaller wavy motions $\sigma = 1$ provides increasing damping with larger wave numbers. A value of $\sigma = \frac{1}{2}$ results in weaker damping of such motions.

The previously exposed steps yielded the assemblage of the final matrix equation. The equation is defined as follows:

$$\sum_{s''=1}^{smax} A_{s,s''} \ddot{\theta}_{s''}^{n+1} + \sum_{s''=1}^{smax} (E_{s,s''} + B_{s,s''}) \dot{\theta}_{s''}^{n+1} + \sum_{s'=s-1}^{s+1} C_{s,s'} \theta_{s'}^{n+1} = d_s \quad (3.23)$$

Here A, B, C, E and d_s are matrices containing coefficients and values of the variables defined a previous time levels. The equation is solved by Gauss elimination with partial pivoting, leading to the solution at the new time level, θ^{n+1} (Uittenbogaard, 2006).

4. Experiments by Bakker

4.1. Set-up

Experiments with artificial plants (“mimics”) were conducted in the wave flume of the Fluid Mechanics Laboratory, at Delft University of Technology, in order to generate data to validate Dynveg. A number of individual stems were tested under varying wave conditions. For the different set-ups, both motion and forces at the base were measured (Bakker, 2015).

The wave flume is 40 m long and 0.8 m wide (Hu et al., 2014). A wave generator with an active wave absorption system is located at one side of the flume. Four rectangular mimics with different cross-sections and materials (ABS, polypropylene and polystyrene) were analysed. Two heights ($h = 0.15$ m and $h = 0.30$ m) were used for each mimic. The properties of the tested plants are summarized in Table 1. Eight different wave conditions were selected as input for wave generation, with a water depth of $h = 0.45$ m in all of them. The drag force exerted on the individual stem was measured with a force transducer (FT) mounted in the false bottom. The wave properties were recorded by a number of capacitance-type wave gauges (WG), located at different positions along the flume. The instantaneous horizontal (u) and vertical (w) velocities were measured with an electromagnetic flow meter (EMF) at a fixed elevation in the water column. Every time the mimic set-up changed (the type of mimic or its height) the elevation of the measurements was modified. Nevertheless, since the flow is considered to be undisturbed by one single stem, velocity profiles under a certain wave conditions were obtained combining data from different experiments. The motion of the stem was captured with a video camera and post-processed to obtain the shape and location of the vegetation over time.

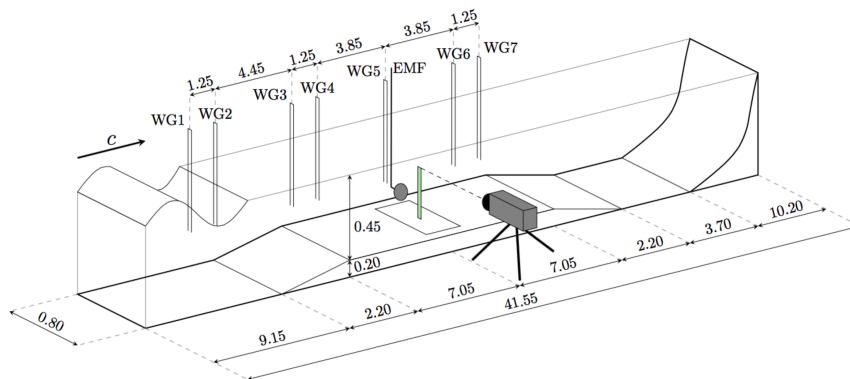


Figure 18. Schematic overview of the experimental set-up. Source: (Bakker, 2015)

Table 1. Properties of mimics that were used in the experiments, where Mimic 1 is the most flexible artificial plant and 4 the most rigid.

Mimic	Length	Width	Thickness	Young's Modulus	Density
-	h_v [cm]	b [mm]	d [mm]	E [N/m ²]	ρ [kg/m ³]
1	15/30	10.0	0.2	8.70E+08	950
2	15/30	10.0	0.5	3.30E+09	1030
3	15/30	8.0	1.6	2.20E+09	1090
4	15/30	6.0	6.0	2.20E+09	1090

4.2. Observations

The most flexible mimics followed the wave motion, with more symmetric excursions under small waves and larger excursions in the wave direction under larger waves. This asymmetry was partially explained by the non-linearity of higher waves (Bakker, 2015) but also by the reconfiguration of the stem, resulting in a streamlined and drag reducing position during the negative orbital velocity (Döbken, 2015). Periodic twisting of the mimics was recorded under the highest waves.

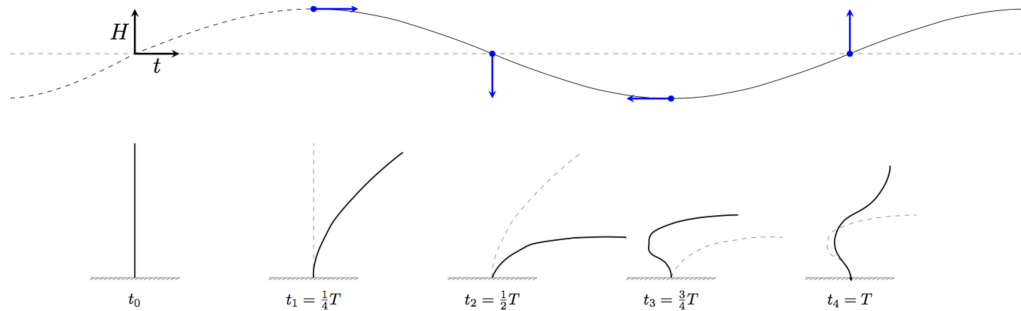


Figure 19. Sketch of the asymmetric motion of flexible vegetation under waves. Source: (Bakker, 2015)

Base forces were estimated using linear wave theory, the Morison formula and constant drag and inertia coefficients ($c_D = 2$, $c_M = 2$) and compared with the results from the experiments. The differences were greater for flexible stems, where a large part of the mimic moved with the flow and the measured forces were considerably lower than the predictions. For such cases, a reduction of mimic length did not result in appreciable changes in the forcing. The correspondence between estimations and measurements was better for rigid mimics, where decreasing the height of the plant resulted in a similar decrease in the base force. Vibrations ($3 \leq f \leq 13 \text{ Hz}$) were observed for the long stiff stems under large waves, associated with vortex shedding. The shortest and stiffest mimic experienced faster vibrations, with $f \approx 50 \text{ Hz}$, that seemed to correspond to estimates of its first natural frequency (Bakker, 2015).

5. Model validation for submerged rigid cylinders

For the most rigid stem tested by Bakker (2015) (Mimic 4) the hydrodynamic force is small compared to the mechanical restoring force and the motion of the plant is negligible ($\dot{x} \approx \dot{z} \approx 0$). The properties of the stiffest stem are summarized in Table 1. Since the plant can be assumed to remain still, the mean drag and inertia coefficients can be derived from the Morison equation directly introducing the measured velocities in equation (2.9). Values of c_D and c_M were calculated that minimized the difference between the recorded force and the estimate by the Morison formula in Section 5.1. The coefficients for each wave condition were introduced as an input in Dynveg together with the corresponding velocity records. This allowed to compute the forces at the base and to assess whether the model reproduces the results of the experiments. The comparison between the modelled and measured forces is shown in Section 5.2. Additional validations for the regime of small plant deformation are included in Appendix A.

5.1. Determination of the force coefficients

5.1.1. Method

There are various techniques to determine the force coefficients experimentally for a particular wave record (Sumer and Fredsøe, 2006). Isaacson et al. (1991) discussed the relative accuracy of different approaches for periodic flows using numerical simulations and concluded that out of the examined techniques, the least squares method applied to the force time series was the simplest and most accurate. It consists of the minimization of the mean-squared difference between the measured and predicted forces (Borgman, 1972) and assumes constant values of the inertia and drag coefficients over the wave period. The sum of the errors over the length of the record is given by:

$$\varepsilon^2 = \sum [F_p(t) - F_m(t)]^2 \quad (5.1)$$

The minimum error ε^2 corresponds to the pair of values of c_D and c_M that satisfy the following equations (Sumer and Fredsøe, 2006):

$$f_d \left(\sum u^4(t) \right) + f_i \left(\sum u(t)|u(t)|\dot{u}(t) \right) = \sum u(t)|u(t)|F_m(t) \quad (5.2)$$

$$f_d \left(\sum u(t)|u(t)|\dot{u}(t) \right) + f_i \left(\sum \dot{u}^2(t) \right) = \sum \dot{u}(t)F_m(t) \quad (5.3)$$

with:

$$f_d = \frac{1}{2} \rho c_D w \quad (5.4)$$

$$f_i = \rho c_M A \quad (5.5)$$

Here $u(t)$, $\dot{u}(t)$ and $F_m(t)$ denote the velocity, acceleration and force measured at time t , ρ is the fluid density, A is the cross-sectional area of the stem and w is its width.

It should be born in mind that the method is quite sensitive to errors in time lag between wave and force signals and subsequently requires accurate estimations of the relative phase error (Isaacson et al., 1991). It can be used both for the whole record and for each individual wave cycle (Naghypour, 2001). A moving window approach was firstly adopted in this work, in which a least-square fit was applied over successive portions of the force time

series. This provided a picture of the variability of the estimated coefficients (Isaacson et al., 1991) and allowed to assess the convergence of the conditions to a steady state. A time interval equal to twice the wave period was used instead of doing a wave-by-wave analysis in order to minimize spurious effects.

5.1.2. Time series correction

Bakker (2015) conducted a total of 24 different experiments for mimic 4. For every length ($h_v = 0 - 15 - 30$ cm), 8 wave conditions were tested resulting in 16 set-ups, i.e. combination of stem length and wave condition, from which the force coefficients can be obtained (Table 2). Data corresponding to the transient periods at the beginning and at the end of the experiments were not included in the analysis.

Table 2. Test conditions for Mimic 4 with varying wave and stem configurations

Mimic	h_v [m]	H [m]	T [s]	Experiment
4	0.3	0.04	1.0	4L30H040T10EMF025
	0.3	0.04	2.0	4L30H040T20EMF025
	0.3	0.07	1.5	4L30H070T15EMF025
	0.3	0.07	2.5	4L30H070T25EMF025
	0.3	0.11	2.0	4L30H110T20EMF025
	0.3	0.11	3.0	4L30H110T30EMF025
	0.3	0.16	2.0	4L30H160T20EMF025
	0.3	0.16	3.5	4L30H160T35EMF025
	0.15	0.04	1.0	4L15H040T10EMF050
	0.15	0.04	2.0	4L15H040T20EMF050
	0.15	0.07	1.5	4L15H070T15EMF050
	0.15	0.07	2.5	4L15H070T25EMF050
	0.15	0.11	2.0	4L15H110T20EMF050
	0.15	0.11	3.0	4L15H110T30EMF050
	0.15	0.16	2.0	4L15H160T20EMF050
	0.15	0.16	3.5	4L15H160T35EMF050

Every time a stem was tested in the laboratory the velocities were measured at a fixed height for all wave conditions. For instance, the elevation of the EMF for Mimic 4 with $h_v = 30$ cm was $z = 2.5$ cm above the bottom in all the runs. This height was changed whenever a different type of plant was analyzed; when the length of Mimic 4 was changed to $h_v = 15$ cm the velocities were recorded at $z = 5$ cm. In order to construct the complete velocity profile under a wave condition, time series for velocities from different types of stem were combined since the effect of a single plant on the hydrodynamics is considered negligible. The relative time shift between the flow measurements from different experiments was calculated in order to ensure that the velocities along the vertical coordinate corresponded to the same phase of the wave. The time shift was determined by maximizing the correlation between the surface elevation of each test case and that of the reference set-up, according to:

$$R(\eta_r(t), \eta_i(t + \Delta t_s)) = \frac{\sum_{j=1}^{T/\Delta t} \eta_{rj}(t), \eta_{ij}(t + \Delta t_s)}{\sqrt{\sum_{j=1}^{T/\Delta t} \eta_{ij}(t + \Delta t_s)^2}} \quad (5.6)$$

Where η_r and η_i are the surface elevations for the configuration of interest and for another experiment with the same wave condition, T is the wave period, Δt is the timestep and Δt_s is the time shift.

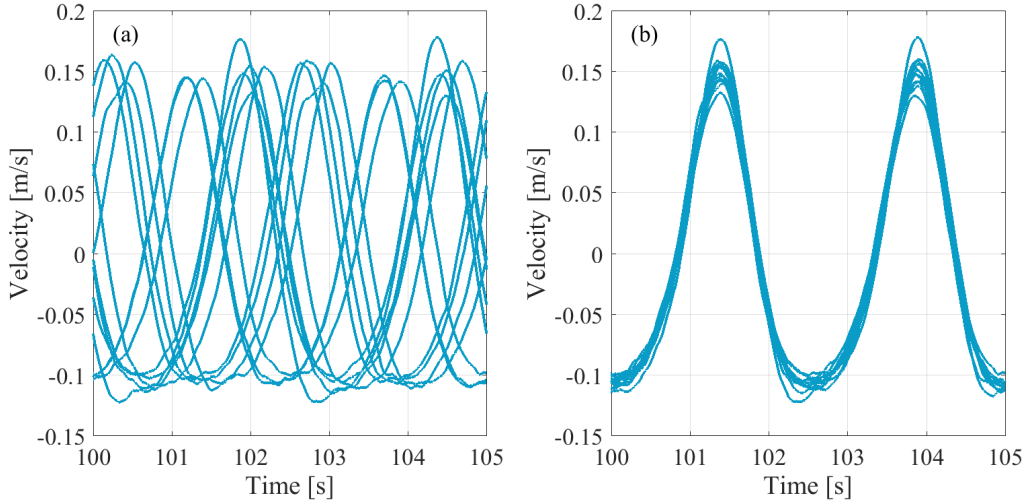


Figure 20. (a) Correlated and (b) uncorrelated velocity signals from different experiments (with different mimics and heights of the EMF) for the wave condition $H = 0.07$ m and $T = 2.5$ s

Time shifts were also observed in the measured velocity, force and surface elevation signals caused by the low-pass pre-filter in the EMF and wave gauges. The delay with respect to the force transducer was of 80 ms for the velocity and 30 ms for the surface elevation (Döbken, 2015), and these offsets were corrected for. For each mimic, depth-integrated values of the squared horizontal velocity were used to estimate the force coefficients:

$$\overline{u^2(t)} = \frac{1}{N} \sum_{i=1}^{i=N} u_i^2(t) \quad (5.7)$$

Where N is the number of elevations where the velocities were recorded and $u_i(t)$ is the velocity time-series at a height z_i .

5.1.3. Evolution of the coefficients

The coefficients obtained from fitting successive intervals of 2 wave periods displayed a similar temporal behaviour in all cases. The time evolution of c_D for the longest mimic under the most energetic wave condition is shown in Figure 21.

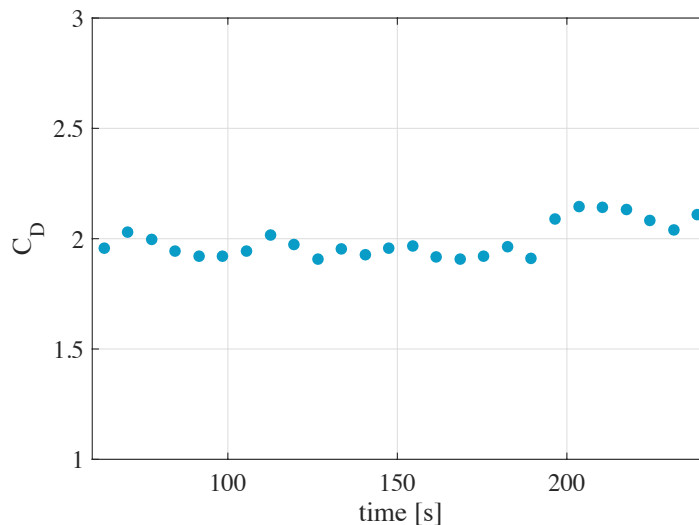


Figure 21. Time-varying estimated drag coefficient estimated for mimic 4 with $h_v = 0.3$ m, $H = 0.16$ m and $T = 3.5$ s

As it can be observed in Figure 21, the wave-averaged drag coefficient fluctuates over time and does not converge to a steady value. Within a shorter adjustment period, a quasi-steady free surface elevation was reached in the experiment, as shown in Figure 22, for which the wave surface profile at contiguous periods was almost the same. Nevertheless, the convergence to the steady state is governed by a longer timescale, representative of the time required by the energy of the group to travel over the flume along the rays (Waseda et al., 1992). Wave harmonics produced by wave generators superimpose forming a wave train. Wave energy travels with the envelope of the free surface at a propagation speed that is lower than that of the individual waves, i.e. the wave celerity (Fredsoe and Deigaard, 1992). It is not known from either theory or experiments how much time is required to establish steady state dynamic conditions in a wave flume (Nath, 1978). Furthermore, laboratory measurements are affected by harmonic contamination by the wave maker, resonant modes within the flume and long bound wave motion among other effects that violate the assumption of steady flow (Tørum and Gudmestad, 2012).

5.1.4. Convergence to steady state

The undertow is an offshore-directed current that compensates for the shoreward mass of water in the presence of a confined boundary. Considering a Eulerian mass balance in the water column, it can be related to the wave energy density (Stive and Wind, 1986). As a consequence, the development of the undertow has been analysed to gain a better insight of the evolution of the wave energy during the experiments.

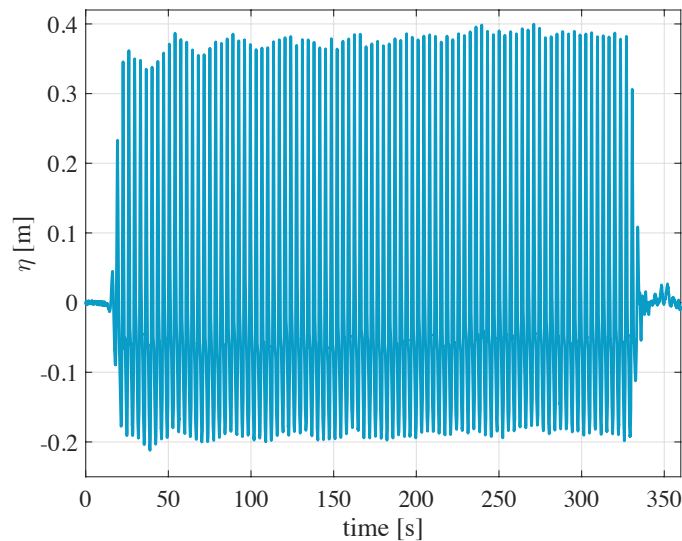


Figure 22. Measured surface elevation for Mimic 4 with $h_v = 0.3$ m, $H = 0.16$ m and $T = 3.5$ s.

The time-evolution of the wave-averaged velocity at a fixed elevation below the wave trough is shown in Figure 23. Velocity profiles of successive time intervals do not coincide, neither the magnitude of the undertow reaches a constant value until the end of the time series. Moreover, a positive drift is observed around $z = 0.27$ m although the Eulerian flow at such elevation should be negative according to the explanation given in Section 2.2.2. The steady state was not achieved during most of the duration of the experiment, which may be a possible explanation for the variations of the wave-averaged force coefficients over time.

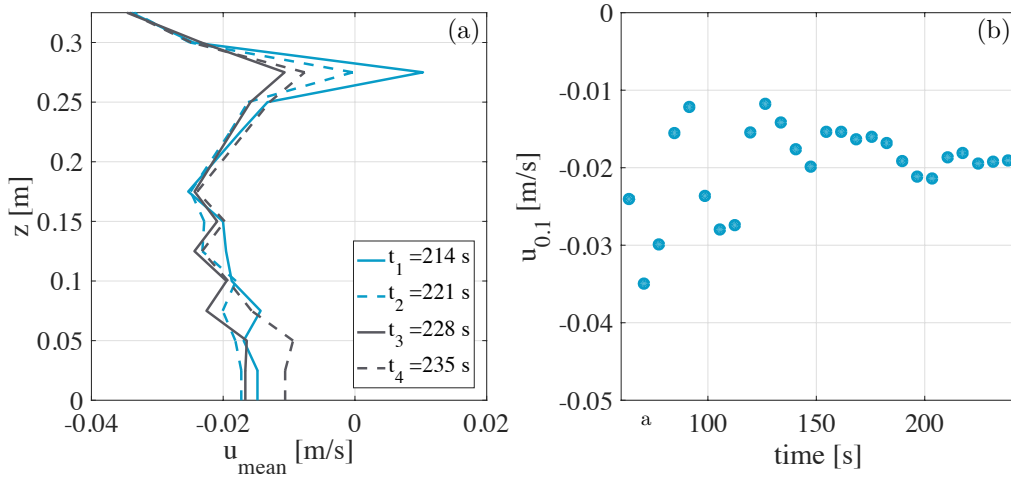


Figure 23. Development of the undertow for mimic 4 with $h_v = 0.3$ m, $H = 0.16$ m and $T = 3.5$ s. (a) Successive vertical mean velocity profiles. (b) Time evolution of the undertow at $z = 0.1$ m with respect to the bottom.

Since the coefficients oscillate around approximately mean values along the time series (Figure 22), time intervals were selected for each test case excluding the transient parts of the record for which average coefficients were calculated. The estimated force coefficients are plotted against the Keulegan Carpenter number in Figure 24.

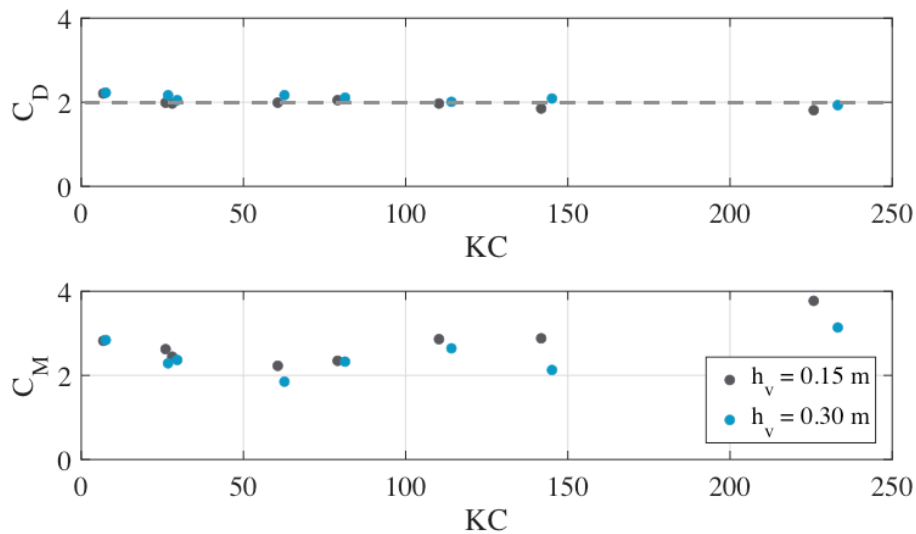


Figure 24. Estimated force coefficients for all the experiments with mimic 4 as a function of Keulegan-Carpenter number. The theoretical curve of c_D suggested by Graham (1980) for squared cross-sections at low KC numbers ($c_D \approx KC^0$) is shown in a black dashed line.

5.1.5. Comparison with the existing literature

Despite the limited number of cases for which mimic 4 was tested, the force coefficients display a good correspondence with the trends found in other experiments conducted with squared cross-sections under waves. The drag coefficient decreases with increasing KC within a narrow range of values in accordance with studies by Okajima et al. (1998) and Graham (1980) among others. The highest values of c_D (of around 2.2) are within the range of values reported in the literature ($c_D = 2 - 3$). Such values are obtained at low KC numbers, associated with early flow separation and vortex shedding at sharp-edged bodies (Venugopal et al. 2008). The rate of decrease slows down at $KC \approx 20$, which approximately corresponds to the transition from the symmetric

to the asymmetric vortex shedding regime at the edges of the cylinder, as reported by Okajima et al. (1998) and Keulegan and Carpenter (1958). Heideman and Sarpkaya (1985) observed that c_D converges to the steady state value of 2 for KC numbers larger than 150, with the formation of the Von Karman vortex street and an approximately constant wake width.

The evolution of the inertia coefficient over KC also reproduced the trends found in the literature. At low KC , c_M is close to its potential flow value of around 2.8 (Bearman et al., 1984), decreases with KC until $KC \approx 80$ (Bearman et al., 1984; Graham, 1980) and increases with KC beyond this point (Okajima et al., 1998).

The force coefficients are more sensitive to the length to width ratio for higher values of KC , as found by Nakamura et al. (1991). A larger difference is obtained for different mimic lengths in such range due to the higher importance of end effects. In accordance to observations McClean and Sumner (2014), higher-pressure recovery for the shorter mimic resulted in a smaller value of c_D and a larger inertia coefficient c_M in comparison to the longer stem.

5.2. Validation of Dynveg

5.2.1. Validation

Before conducting the validation of the model, the code was analyzed in detail to ensure that the equations had been correctly implemented. It was found that the work of Döbken (2015) did not include the Froude Krylov force and therefore this load was incorporated in the model. Once the modification was done, the velocity time series recorded during the experiments were introduced as an input in Dynveg and interpolated linearly in space, so that the flow was defined at every stem segment. The accelerations were computed from the measurements using backward differentiation. The force coefficients were given the values calculated from the measurements. The motion of the leaf was obtained solving the integro-differential equation introduced in Section 3 at every timestep, in which the unknown was the bending angle θ of each segment. The position, velocities and accelerations of the stem were derived from the angle θ making use of the compatibility equations and the boundary conditions, resulting in the following expressions:

$$x(x, z) = \int_0^s \sin \theta \, ds' \quad (5.8)$$

$$z(x, z) = \int_0^s \cos \theta \, ds' \quad (5.9)$$

$$\dot{x}(x, z) = \int_0^s \cos \theta \, \dot{\theta} \, ds' \quad (5.10)$$

$$\dot{z}(x, z) = \int_0^s -\sin \theta \, \dot{\theta}(s') \, ds' \quad (5.11)$$

$$\ddot{x}(x, z) = \int_0^s (-\sin \theta \, \dot{\theta}^2 + \cos \theta \, \ddot{\theta}) \, ds' \quad (5.12)$$

$$\ddot{z}(x, z) = \int_0^s (-\cos \theta \, \dot{\theta}^2 - \sin \theta \, \ddot{\theta}) \, ds' \quad (5.13)$$

Where x and z indicate the position of the stem and \dot{x} and \dot{z} and \ddot{x} and \ddot{z} are the horizontal and vertical velocities and accelerations respectively.

The force at the base of the plant was obtained through two alternative procedures.

- The integrated force was calculated applying Morison's equation, using the force coefficients derived from the measurements in Section 5.1 the interpolated measured flow velocities and the kinematic properties computed with Dynveg.
- The force was also determined from the moment balance at the root of the plant. Considering that the stem remains still at its base:

$$\frac{dx}{ds} = \sin(\theta) \approx 0 \quad (5.14)$$

$$\frac{dz}{ds} = \cos(\theta) \approx 1 \quad (5.15)$$

Introducing (5.14) and (5.15) in equation (2.6), the following expression is obtained:

$$F_x = -EI \frac{\partial^2 \theta}{\partial s^2} \quad (5.16)$$

Where the horizontal base force is directly related to the flexural rigidity and the curvature of the stem.

The second definition allows to directly assess if the internal forces in Dynveg agree with the data produced in the experiments instead of comparing the measurements with a post-processed force. The latter may lead to a good correspondence with the results even if the movement of the plant is not reproduced accurately, due to the use of fitted force coefficients and given the small magnitude of the motion, which was assumed negligible in Section 5.1.

5.2.2. Results

Experiment and model results are shown below for the cases of the shortest stem under the less energetic wave condition (inertia dominated case, Figure 25) and for the longest mimic with the highest wave height (drag dominated case, Figure 26).

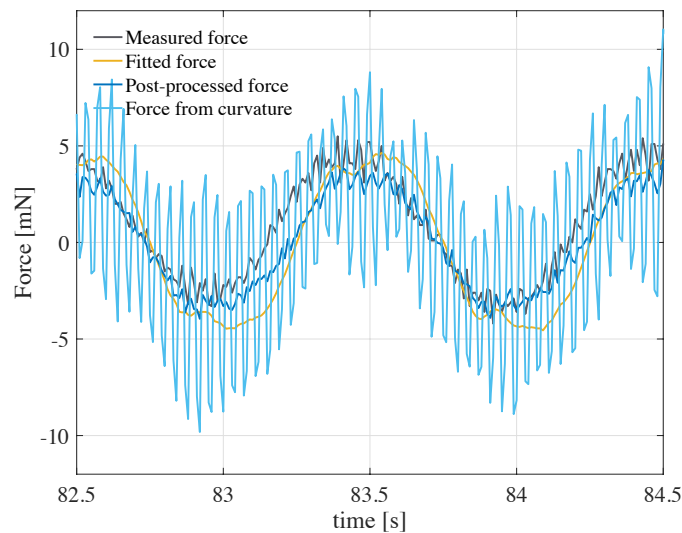


Figure 25. Comparison of the horizontal forces at the base for Mimic 4 with $h_v = 0.15 \text{ m}$, $H = 0.04 \text{ m}$ and $T = 1 \text{ s}$.

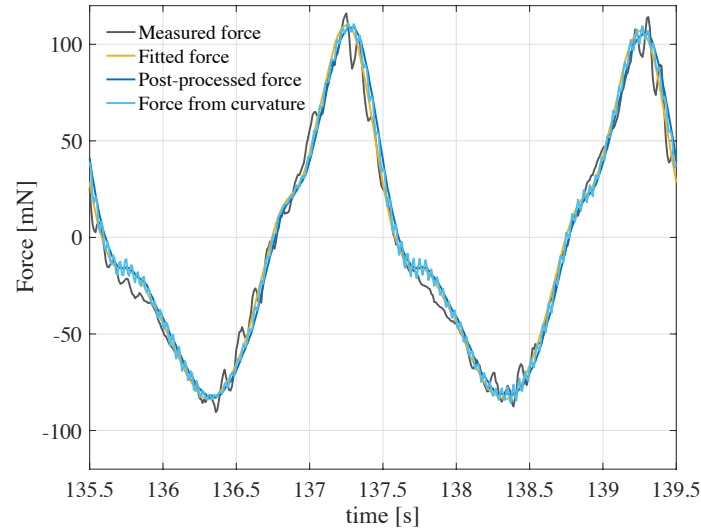


Figure 26. Comparison of the horizontal forces at the base for Mimic 4 with $h_v = 0.3$ m, $H = 0.16$ m and $T = 2$ s.

A good correspondence was found between the post-processed forces and the fitted forces (calculated using the Morison equation neglecting the motion of the plant). The latter deviates from the measured force time series at some points, at least partially due to the use of constant force coefficients. In practice, both the Reynolds number and the Keulegan Carpenter number change with the orbital velocities during the wave cycle, as shown in Figure 24, and this would result in different values of c_D and c_M over the wave period.

The force calculated from the curvature of the stem at its base displayed fluctuations that had higher amplitude for the inertia dominated cases. Such oscillations were introduced through the time-differentiation of the recorded velocity signals, and propagated in Dynveg through the computed inertia forces. A low-pass filter function was applied to the acceleration time-series, as explained in Appendix B. The comparison of the measured and calculated forces after filtering is shown in Figure 27.

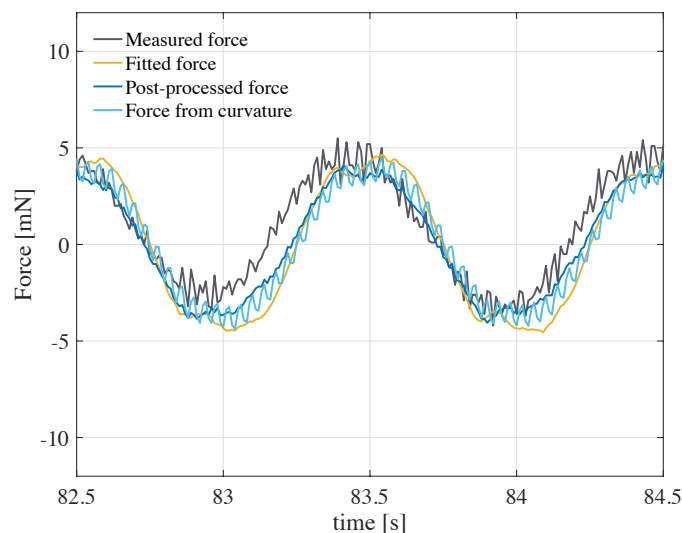


Figure 27. Comparison of the horizontal forces at the base computed using velocities from the linear wave theory with the recorded forces after applying a low-filter function for Mimic 4 with $h_v = 0.15$ m, $H = 0.04$ m and $T = 1$ m.

As it can be observed in Figure 27, Dynveg reproduced the results from the experiment with high accuracy and the large fluctuations were not present in the computed forces when continuous acceleration time-series were

implemented in the model. The complete analysis of the oscillations is presented in Appendix B. Additional checks of Dynveg, making use of the Morison formulation and the differential equation for the deflection of a cantilever beam, are included in Appendix A. The effect of the timestep and the integration method was also analyzed in Appendix C. Since the performance of the model was considered satisfactory, Dynveg was further used to study the interaction between wave hydrodynamics and flexible vegetation, developed in Section 6.

6. Analysis of plant dynamics under wave loading with Dynveg

In the present section, the motion and forces on a single stem under different wave conditions were modelled using Dynveg. The reference set-up is schematized in Figure 28. The characteristics of the stem were initially set equal to those of Mimic 2 from the laboratory experiments by Bakker (2015). Mimic 2 experienced significant deflections and moved with the flow during the tests, but it did not twist out of its plane (unlike Mimic 1, the most flexible plant), remaining within the assumptions of the model (Section 3). Its properties are summarized in Table 1. The force coefficients were given constant values of $c_D = 2$ and $c_M = 2$ and the influence of the angle of attack was accounted for using the formulation by Dijkstra et al. (2006). The water depth was equal to $h = 0.45$ m during the runs. The simulations were carried on until converging to a steady state, where the motion of the tip was the same in successive wave periods.

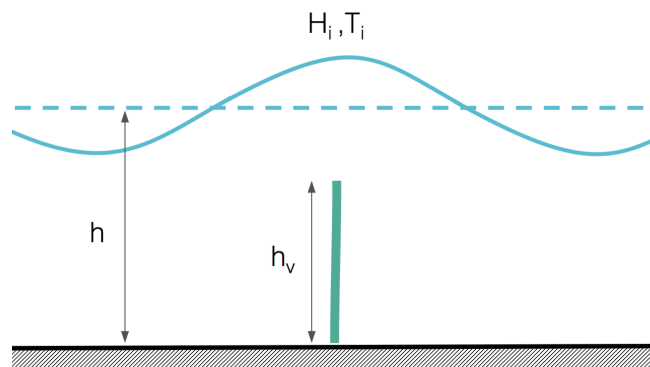


Figure 28. Reference set-up for the runs, where h is the water depth, h_v is the height of the stem and H_i and T_i are the wave height and wave period of the considered wave condition.

Wave hydrodynamics were represented by different theories. The analysis started implementing a depth-uniform velocity profile that oscillates with the wave period, which is studied in Section 6.1. The depth-dependency of the oscillatory flow was firstly introduced through the use of linear wave theory, in which velocities decrease in deeper parts of the water column according to hyperbolic functions. The corresponding analysis is developed in Section 6.2. The influence of varying the geometry and mechanical properties of the plant is evaluated in Section 6.2.4. The effect of using different formulations for the drag is addressed in Section 6.2.5. Previous sections defined the velocities at the same horizontal position for every height over the bed. Variations in the velocity field with the horizontal coordinate were incorporated in Section 6.3. Besides the oscillatory flow, mass transport by waves results in a mean return current that was implemented in Section 6.4. As it was explained in Section 2, the surface elevation for steeper waves deviates from the sinusoidal form described by the linear wave theory and results in asymmetries in the water particle velocities. Higher order effects were studied in Section 6.5. The analysis of the results presented below is discussed in more detail in Section 7.

6.1. Depth-uniform oscillatory flow

6.1.1. Method

The simplest type of oscillatory flow consists of a sinusoidal current with a constant magnitude along the water column. The corresponding velocity profile would be represented by:

$$u(x, z, t) = u_m \cos \omega t \quad (6.1)$$

$$w(x, t) = 0 \quad (6.2)$$

Where u_m is the maximum horizontal velocity, ω is the angular frequency and t represents the time. In the present study, the amplitude of the velocity was set equal to the value given by linear wave theory at the bottom ($z = -h$):

$$u_m = \frac{\pi H}{T} \cdot \frac{1}{\sinh kh} \quad (6.3)$$

Where H is the wave height, T k is the wave number and h is the water depth. In order to evaluate the behaviour of a stem a series of runs were carried out in Dynveg introducing different combinations of H and T .

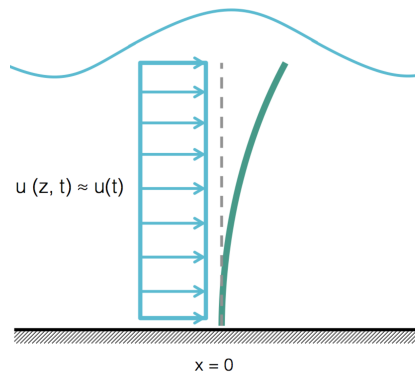


Figure 29. Velocity profile under the simulated depth-uniform periodic flows at a timestep t . The velocities at every segment were defined at $x = 0$. The magnitude of the flow varied between $-u_m$ and u_m over the period.

The plant response was evaluated in terms of its trajectory and the horizontal hydrodynamic forces at the base.

6.1.2. Plant motion

The motion of the plant over a wave period showed similar behaviour for all the wave conditions tested, and is illustrated for two different wave heights in Figure 30.

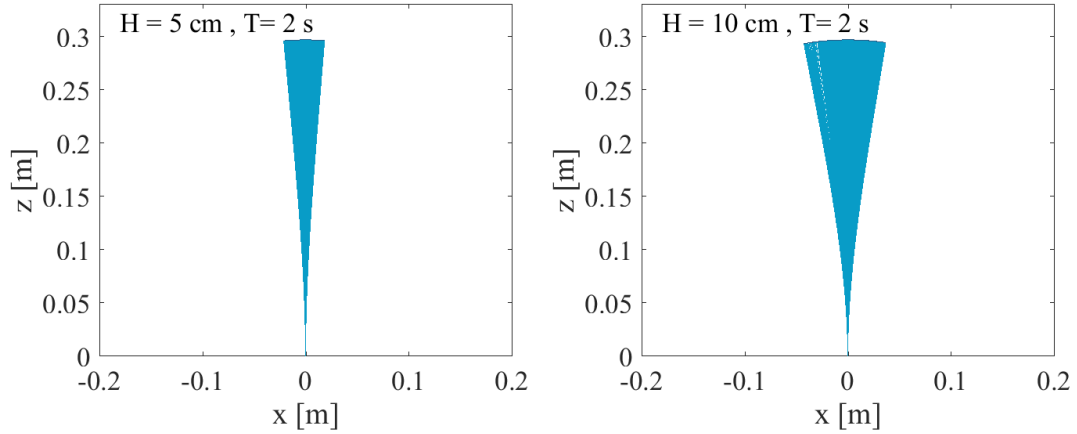


Figure 30. Plant trajectory under oscillatory flow for $H = 0.05$ m and $T = 2$ s (left) and for $H = 0.10$ m and $T = 2$ s

The stem followed the water motion during each half of the period. Larger deflections were obtained under higher velocities. The amplitude of the excursion was equal during both phases of the wave.

6.1.3. Horizontal base forces

Due to the symmetrical behaviour of the plant, the wave-averaged values of the forces at the base were equal to zero, as shown in Figure 31.

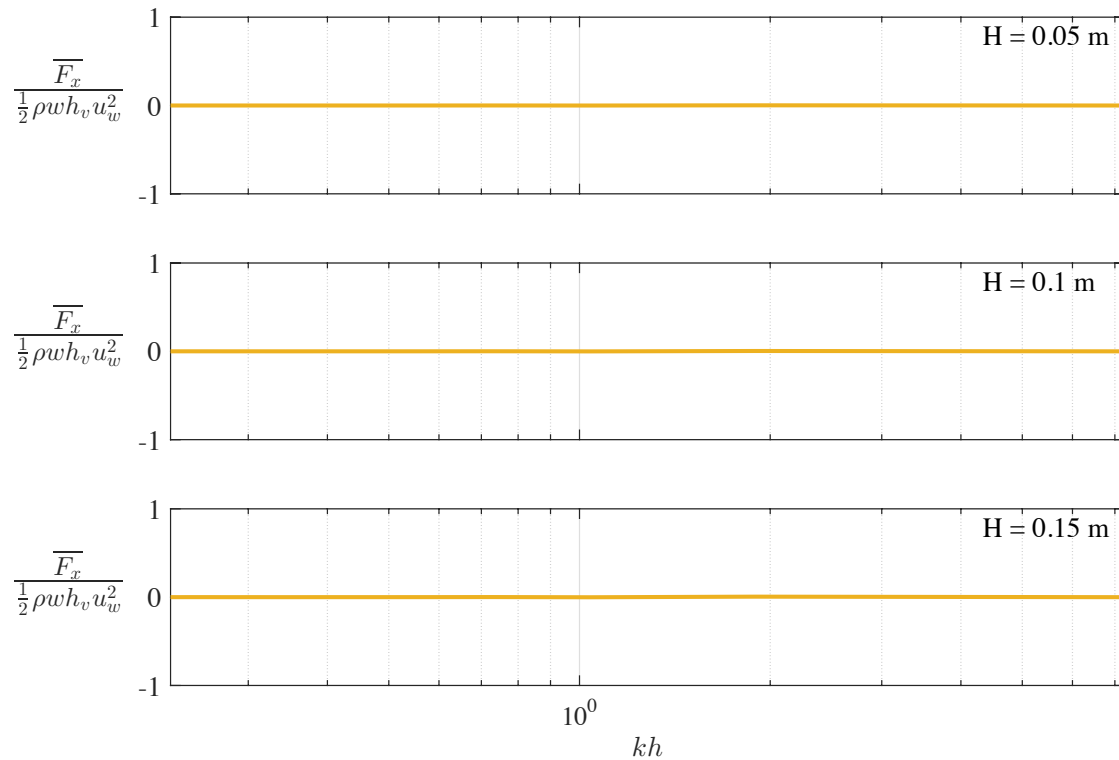


Figure 31. Period-averaged dimensionless forces at the base, given by equation (6.4), as a function of the relative depth kh for depth-uniform oscillatory flow. The force was computed from the curvature, as indicated in Section 5 and kh is defined as the product of the wave number k and the depth h

6.2. Linear wave theory

The effect of depth-variations in the velocity profile was implemented using linear wave theory, initially assuming that the horizontal position of the stem segments was equal to zero regardless of their actual location, i.e. $x_v(s, t) = 0$, where s is the coordinate along the stem.

$$u(x, z, t) = \frac{\pi H \cosh k(z + h)}{T \cosh kh} \cos(\omega t) \quad (6.3)$$

$$w(x, z, t) = \frac{\pi H \sinh k(z + h)}{T \sinh kh} \sin(\omega t) \quad (6.4)$$

Different wave heights were used as an input, covering the range of small linear waves, high non-linear waves and intermediate heights in between both extremes (from $H = 0.01$ m to $H = 0.2$ m). The model was run for wave periods between $T = 0.1$ s and $T = 12$ s seconds at intervals of $T = 0.1$ seconds for each of those wave heights. The comparison of the results is shown below.

6.2.1. Base forces

The forces at the base were calculated using the computed curvature, as indicated in Section 5. The wave-averaged value of the load was determined according to:

$$\bar{F}_x = \frac{1}{T} \int_0^T F_x(t) dt \quad (6.5)$$

Where T is the wave period and $F(t)$ is the instantaneous force at the base. The forces were expressed as dimensionless scaling force coefficients, using the exposed area of the stem and the orbital velocities at the bottom:

$$F_{dim} = \frac{\bar{F}_x}{\frac{1}{2} \rho w h_v u_w^2} \quad (6.6)$$

Where h_v is the stem length, w is its width, u_w is the orbital velocity at $z = -h$ and ρ is the fluid density. The dimensionless base force was plotted against the relative depth, defined as the product of the wave number, k , and the water depth, h . A comparison of the results obtained for different values of the wave height is shown in Figure 32.

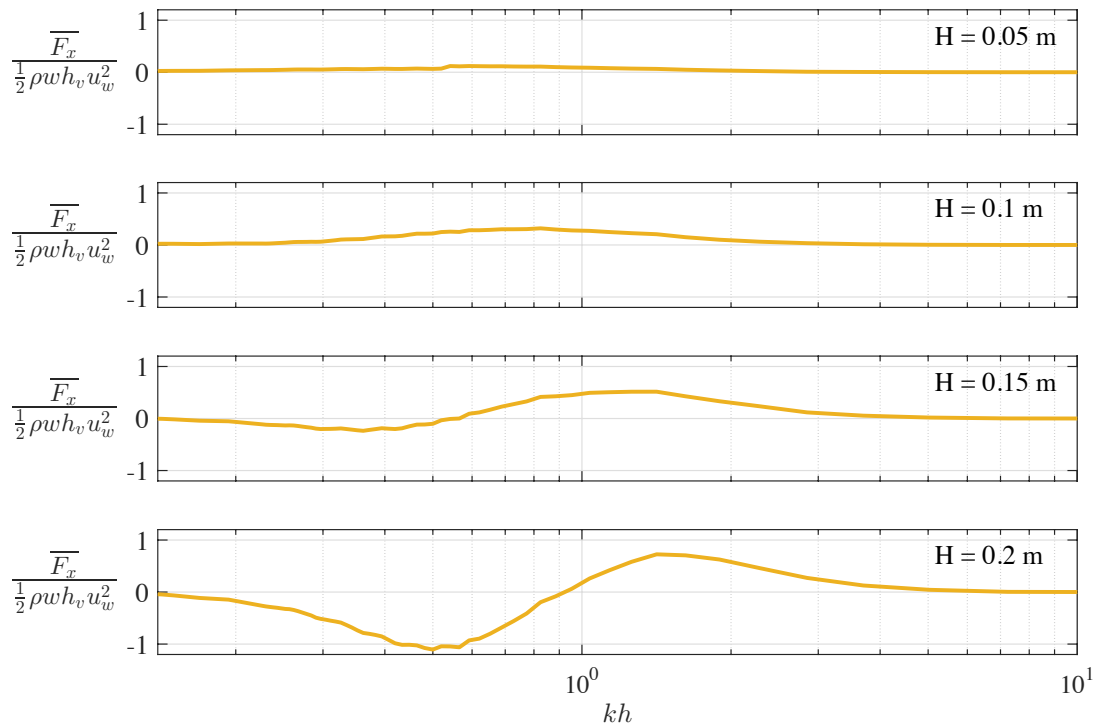


Figure 32. Dimensionless horizontal base forces over the relative depth, kh , expressed as the product of the wave number k and the depth h

The evolution of the dimensionless mean base force as a function of the frequency displayed similar trends for the different modelled wave heights. Nevertheless, the magnitude of the loads and the transition between different behaviours varied depending on the value of H . Four regimes are recognized in the curves, which are schematized in Figure 33:

- The base force was equal to zero for the highest frequencies.
- As the period increased, a second region appeared where the base force had positive values.
- When the periods increased even further, the force at the base decreased in magnitude until it became negative.
- A fourth region existed for wave heights larger than $H = 0.1$ m, where the dimensionless forces were very small and larger than zero for very long periods. For the lowest frequencies the flow resembled a unidirectional current, and the mean force at the base over the wave cycle was equal to zero.

Larger wave heights resulted in higher loads and shifted the transitions between the regions to higher frequencies. The motion and the distributed forces along the stem were analyzed for the case of $H = 0.15$ m, selecting wave conditions representative of the different parts of the graph.

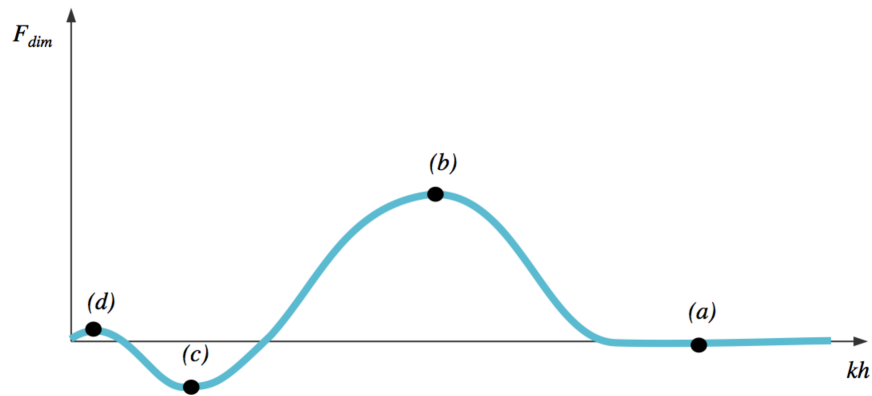


Figure 33. Different regimes found in the dimensionless force using linear wave theory. (a) Region of high frequency waves, associated to zero wave-averaged forces at the base. (b) Region of intermediate frequencies and positive mean base forces. (c) Region of long waves, associated to negative mean base forces over the wave cycle. (d) Very long waves, with very small and positive wave-averaged forces at the base.

6.2.2. Stem motion

The stem excursion over a wave period is plotted in Figure 34 for $H = 0.15 \text{ m}$ and $T = 0.7 \text{ s}$ (wave condition representative of the high-frequency region), $T = 2 \text{ s}$ (corresponding to the region of intermediate frequencies and positive base forces), $T = 5 \text{ s}$ (which belongs to the low frequency part of the curve, with negative values of the load at the base) and $T = 9 \text{ s}$ (representing the very low frequency waves, which for the highest waves produced a small region with very small positive base forces). The relative velocities for the different cases are shown in Figure 35.

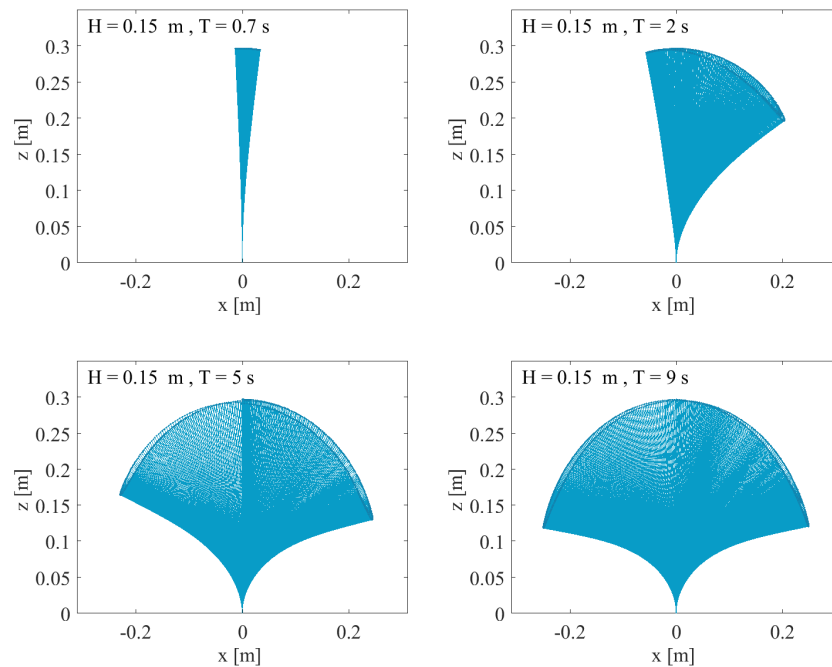


Figure 34. Stem motion over one wave period for different wave conditions.

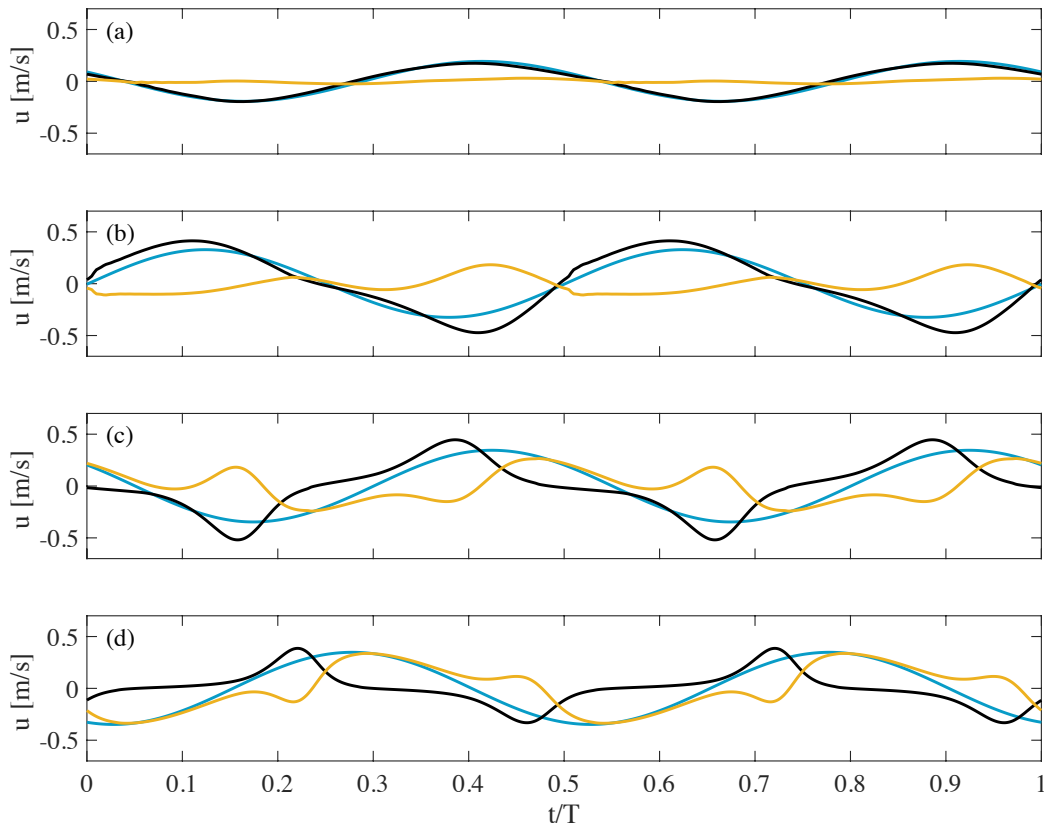


Figure 35. Time series of the flow velocity (—), plant velocity (—) and relative velocity (—) at the tip of the stem. Subplot (a) corresponds to $H = 0.15$ m and $T = 0.5$ s. Subplot (b) represents $H = 0.15$ m and $T = 2$ s. Subplot (c) displays the case of $H = 0.15$ m and $T = 5$ s. Subplot (d) was obtained for $H = 0.15$ m and $T = 7$ s

The stem displayed small trajectories under the high frequency waves (Figure 34 a). The total horizontal excursion at the blade tip ($x_{tip} = x_{max} - x_{min}$) was equal to 1.2 cm over a wave period, and the plant stood upright in the water column. As the period increased (Figure 34 b), the stem motion became more asymmetric, and the plant assumed more streamlined positions in the direction of wave propagation while remaining more upright in the backwards motion. The total excursion of the tip became longer, and reached values of around $x_{tip} = 20$ cm. The plant moved slightly advanced in time with respect to the flow (Figure 35 b) and its velocity had a higher magnitude, resulting in relative velocities and drag forces acting in the opposite direction of the flow.

A further increase of the period increased the time available for the plant to adjust to the flow (Figure 34 c), which caused a more symmetric displacement with a total amplitude of $x_{tip} = 40$ cm. Nevertheless the blade still bent slightly more in the downstream direction. As it can be observed in Figure 35 c, there is a part of period in which the plant remained pronated and still, and the relative velocity is approximately equal to the oscillatory velocity. For the longest periods the flow resembled a unidirectional current and the motion became symmetrical. Plants remained extended over a longer fraction of the wave period where the plant velocity is equal to zero.

The influence of the initial phase of the wave at the beginning of the simulation was also explored. The model was run for a wave condition with different phases ranging from $\varphi = 0^\circ$ to $\varphi = 180^\circ$ at intervals of 45° . The motion of the stem converged after approximately five wave periods in all cases and no hysteresis effects were found. The results are shown in Appendix D.

6.2.3. Distributed forces

The distributed forces along the segments of the stem are represented in Figure 36 for four different wave conditions.

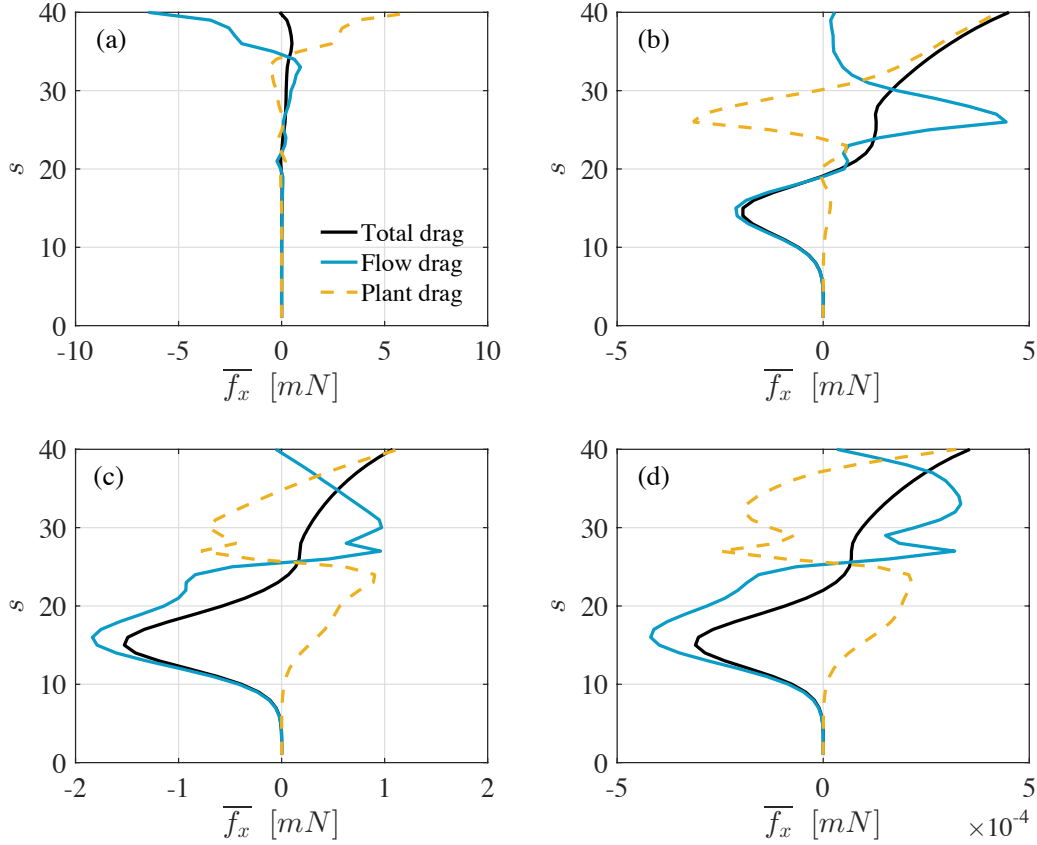


Figure 36. Wave-averaged distributed drag force along the stem segments from $s = 1$ at the bottom until $s = 40$ at the tip. Figure (a) corresponds to $H = 15$ cm and $T = 0.7$ s. Figure (b) represents $H = 15$ cm and $T = 2$ s. Figure (c) displays the case of $H = 15$ cm and $T = 5$ s. Figure (d) was obtained for $H = 15$ cm and $T = 9$ s

For the shortest waves, the velocities were approximately zero at the lowest half of the stem, since the waves were effectively in deep water (Figure 36 (a)). The drag was only significant in the upper part of the plant and it was one order of magnitude smaller than inertia forces. Since the latter were considerably symmetrical over the period, the resulting wave-averaged force at the base was very small. Larger periods resulted in a region of positive drag forces close to the tip, and negative distributed forces at lower positions, as shown in Figure 36 (b) and Figure 36 (c). For the largest wave period the distributed forces were an order of magnitude smaller and had an opposite sign compared to smaller periods, as represented in Figure 36 (d).

6.2.4. Effect of the length and the stiffness

The effect of varying the length and the flexural rigidity of the plant was analyzed in a number of runs. The model was run for $H = 10$ cm and $T = 3.5$ s in all the simulations. The value of the Young's Modulus was changed for the different cases, with values ranging from $1.5 \cdot 10^7$ to $6 \cdot 10^{12}$ N/m². The stem density (ρ_v) and the geometry of the cross-section were kept constant. The simulations were performed for two lengths of the stem; $h_v = 10$ cm and $h_v = 30$ cm. The work was expressed in a dimensionless form, according to:

$$W_{dim} = \frac{\bar{W}}{\rho w h_v u_w^3} \quad (6.6)$$

The dimensionless work was plotted against the flexural rigidity, EI , in Figure 37 a. The ratio between the total excursion of the tip and the length of the stem is represented as a function of EI in Figure 37 b.

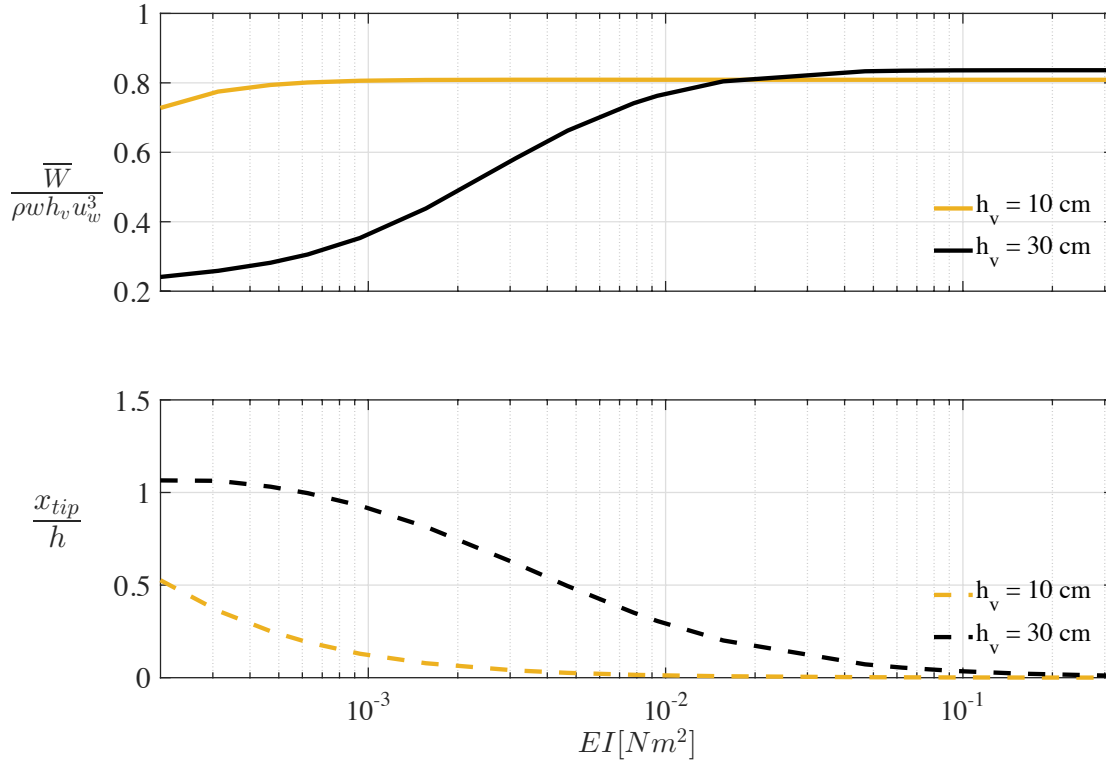


Figure 37 (a) Dimensionless work against the flexural rigidity. (b) Dimensionless tip excursion over a wave period, where $x_{tip} = x_{max} - x_{min}$ and h is the length of the stem. Both graphs correspond to $H = 10$ cm and $T = 3.5$ s.

For the largest values of the elastic modulus ($E > 9.6 \cdot 10^{11} N/m^2$) the motion of the plant was negligible and the relative velocities were equal to the flow velocities. A decrease in the length resulted in slightly less dissipation for such range of stiffness. A further reduction of the rigidity led to appreciable tip motions, as shown in Figure 37. Nevertheless, the dissipation was still equal to that of a completely stiff plant. As the plant became more flexible, the upper part of the stem followed the waves for a longer time, whereas the base remained still. Since the largest contribution of the drag was generated at the lower part of the plant the effect of a longer stem produced a smaller increase in the dissipation compared to rigid case. The short and the long stem generated the same amount of work for $E = 1.92 \cdot 10^{11} N/m^2$. For the lowest flexibilities, both the motion and the work showed a stronger dependence on the vegetation height. The longer stem was able to sway with the flow under a larger fraction of the period before being limited by its size. The shorter stem reached sooner its maximum deflection, and remained extended and aligned with the flow during most of the passage of the wave, subsequently producing more work.

The dimensionless attenuation was also plotted in Figure 38 against the Cauchy number, previously defined in equation (2.19), which resulted in a convergence of the behaviour of stems with different lengths.

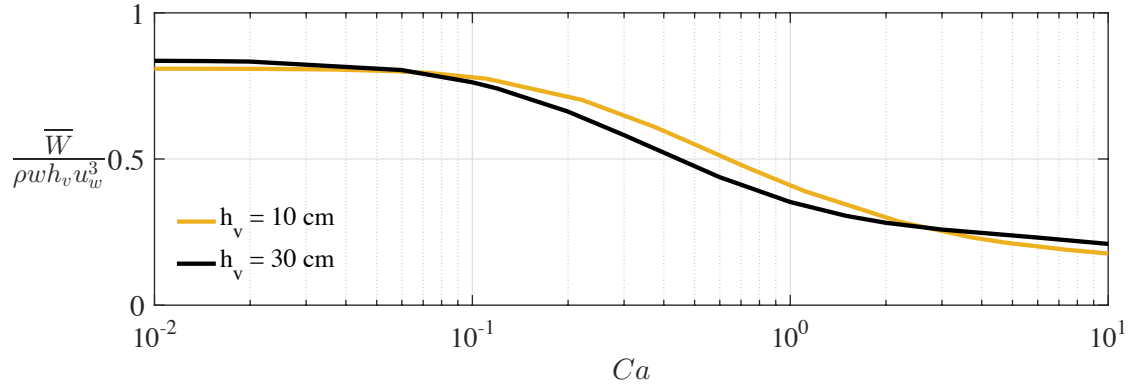


Figure 38. Dimensionless work against the Cauchy number for $H = 10 \text{ cm}$ and $T = 3.5 \text{ s}$.

The relationship between dissipation and flexural rigidity was compared for three different wave periods, for the case of $h_v = 30 \text{ cm}$, as shown in Figure 39.

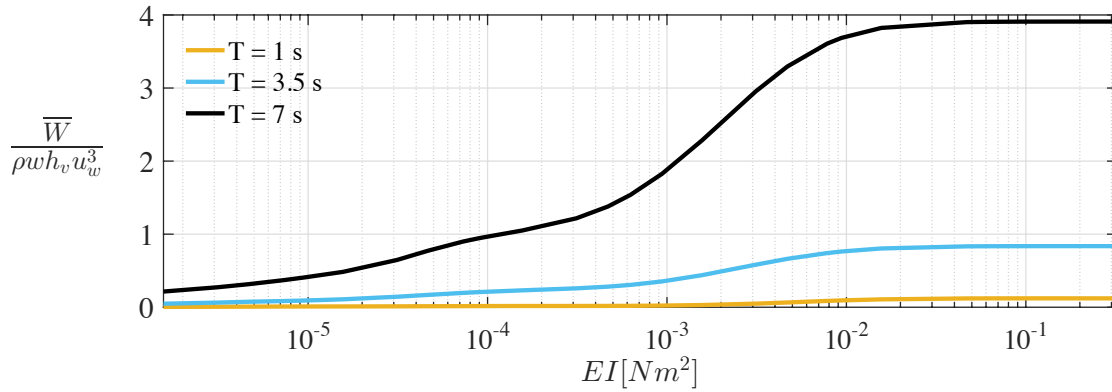


Figure 39. Dimensionless work against the flexural stiffness for $H = 10 \text{ cm}$ and $T = 1, 3.5$ and 7 s

6.2.5. Effect of the formulation for the drag coefficient

In order to evaluate the influence of the incidence angle on the drag coefficient three formulations were compared:

- (1) The use of constant value through the water column, regardless of the orientation of the segments.

$$c_D = 2 \quad (6.7)$$

- (2) The formulation by Hoerner (1965) for circular cylinders, which included the influence of the angle of attack.

$$c_D = 2 \cos \theta \quad (6.8)$$

- (3) The formulation by Dijkstra et al. (2006) for thin strips, which besides accounting for the angle of attack introduced an enhancement of c_D when the plants lie parallel to the flow.

$$c_D = 2 \cos \theta + 0.1 \tan \theta \quad (6.9)$$

The analysis was done for Mimic 2, with $h_v = 30 \text{ cm}$, $H = 0.15 \text{ m}$ and $T = 3.5 \text{ s}$ in which the drag was the dominating load. Both the deflection of the stem and the orientation of the fluid particles vary over the wave

cycle, which result in changes in the value of c_D over time. The wave-averaged distribution of c_D is shown in Figure 40 (a). The mean distributed drag load at every segment is represented in Figure 40 (b). The mean position of the stem is plotted in Figure 41.

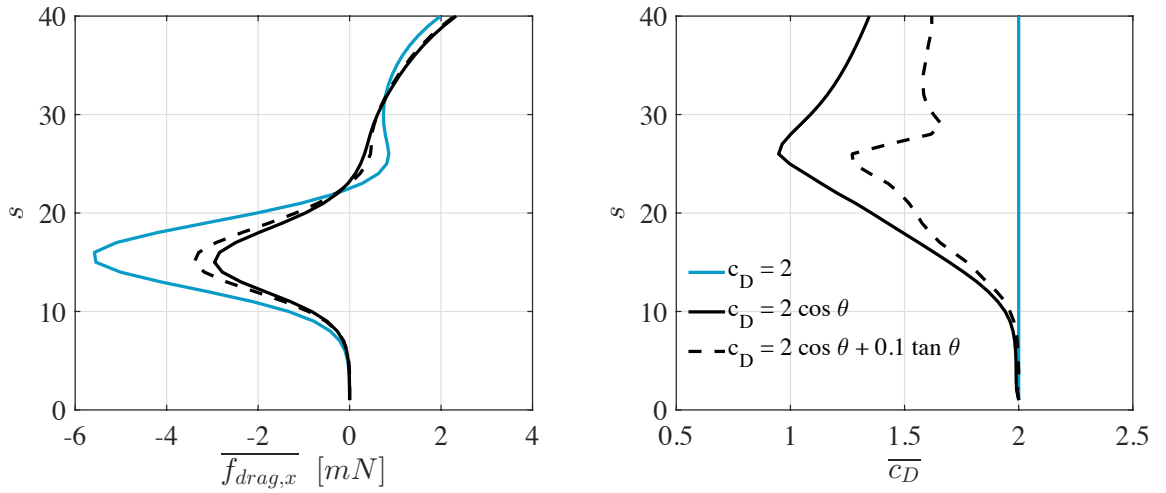


Figure 40. (a) Wave-averaged distribution of the distributed flow drag along the stem segments, from $s = 1$ at the bottom until $s = 40$ at the tip. (b) Wave averaged distribution of the drag coefficient over time.

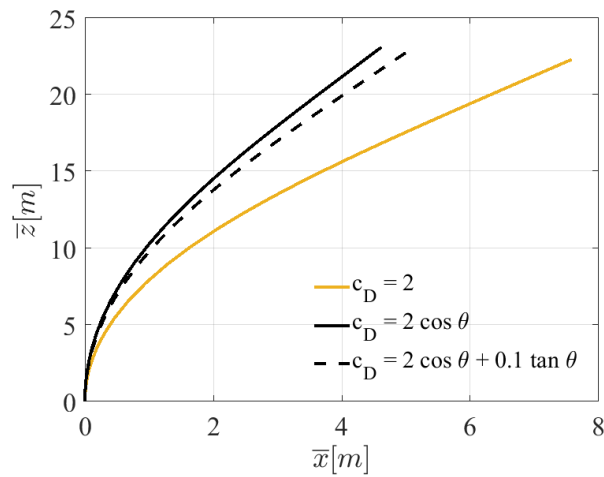


Figure 41. Wave-averaged stem position for the different formulations of the drag coefficient, c_D . The angle between a stem segment and the vertical is represented by θ .

The use of a constant drag coefficient led to higher values of the hydrodynamic forces and a larger downstream position of the stem; the mean deflection of the tip was approximately a 25% longer when the influence of the angle of attack was not incorporated. The difference between formulations (2) and (3) was relatively smaller, of a 12.5%.

6.3. Linear wave theory including horizontal variations of the velocity field

In order to evaluate how spatial variations affect the computed forces and motion, the same wave conditions were run using linear wave theory, defined by equation (2.19) and equation (2.20) in Section 2, firstly assuming that $x = 0$ for all the segments of the stem, and secondly calculating the flow velocity in each of them as a function of their actual horizontal coordinate, $x = x_v$.

6.3.1. Flow velocity

The flow velocities experienced by the individual segments during a wave period, with and without the inclusion of the spatial variations, are shown in Figure 42 for $H = 0.1$ m and $T = 2$ s. The comparison was done at the tip of the plant in Figure 42 a and for a segment located in the middle of the stem in Figure 42 b.

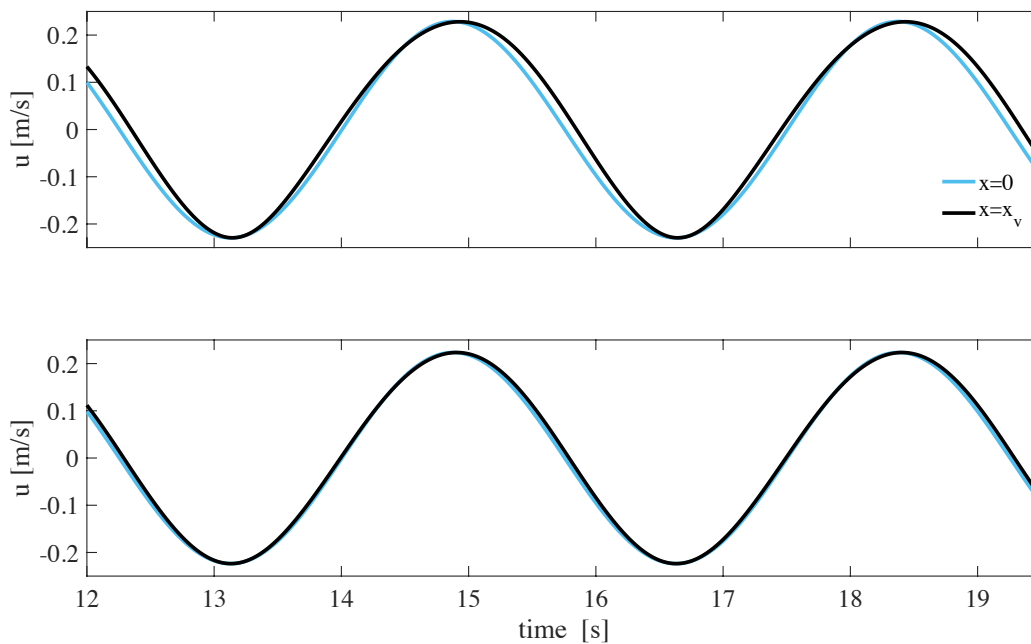


Figure 42. Flow velocity at the stem segments for (a) the tip of the plant $s = s_{max}$ (b) the middle of the stem $s = s_{max}/2$. The blue line represents the velocities calculated using linear wave theory without spatial variations (assuming $x = 0$ for every point) and the black line corresponds to the results obtained using linear wave theory as a function of the horizontal coordinate of the segments ($x = x_v$).

The curves of the velocities as a function of time were similar in the accelerating phase of the wave cycle, while the flow velocities increased in the propagation direction until reaching the maximum velocity of the oscillatory flow. However, since the tip swayed with the fluid and followed the wave during its forward motion, the region of positive velocities in Figure 42 a extends over an interval longer than half of the wave period. Similar effects can be observed in Figure 42 b. Nevertheless, the differences between the curves are smaller at the middle of the stem, given the decrease of the plant motion in lower positions in the water column towards the base, which is fixed to the bottom.

6.3.2. Base forces

The inclusion of the spatial variations in the velocity resulted in larger positive forces at the base, due to higher duration of the positive velocities experienced by the stem, as shown in Figure 44.

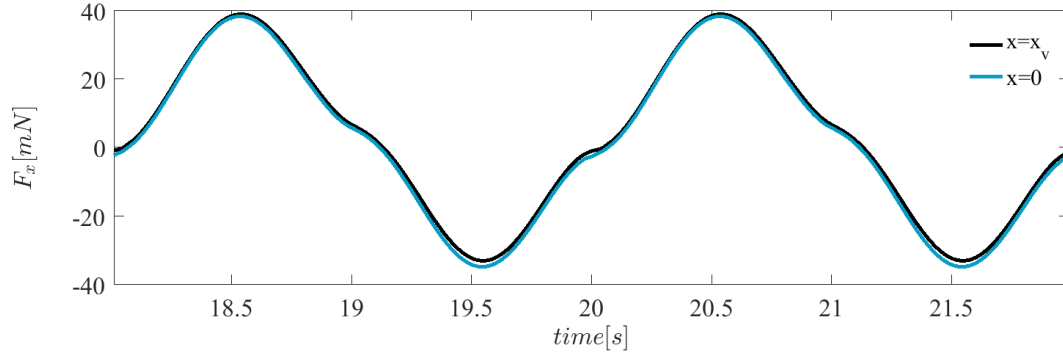


Figure 43. Comparison of the horizontal base force as a function of time for $H = 0.1$ m and $T = 2$ s calculating the velocities at $x = 0$ (blue line) and at the position of the segments, $x = x_v$ (black line).

The trends found in the base load are analogous to those previously identified for the flow velocities. The period of the forcing changed when the phase-lag was incorporated. Negative base forces occurred later in time and positive forces were experienced for a longer fraction of the wave period. When the force was integrated over the wave-cycle, this resulted in higher positive mean values at the base, as observed in Figure 44.

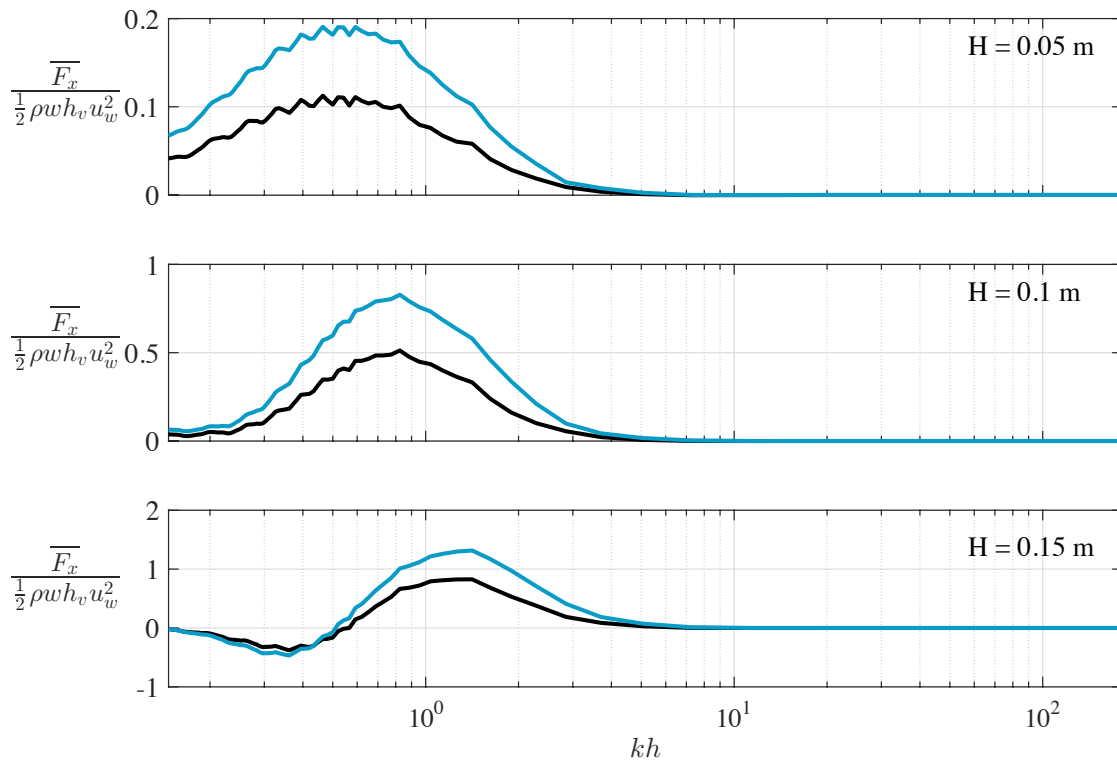


Figure 44. Wave-averaged dimensionless horizontal base force as a function of the relative depth, kh (where k is the wave number and h is the water depth) for three different wave heights. The blue line was computed using linear wave theory with $x = 0$ for every segment. The black line was modelled using linear wave theory with the actual coordinate of the segments ($x = x_v$).

The deviation in the computed loads was evaluated calculating the difference between the wave-averaged values modelled assuming $x = 0$ and those obtained using $x = x_v$ ($\Delta \bar{F}_x = \bar{F}_{x,v} - \bar{F}_{x,0}$), relative to the force computed including the phase lag, $\bar{F}_{x,v}$. The loss of accuracy was not uniform for the different wave heights. For the highest wave ($H = 0.15$ m) the largest differences were obtained for the highest frequencies. For the smallest wave,

$H = 0.05$ m, the differences were larger for the longer waves. The relative error had maximum values of 40% for the dimensional mean values.

The instantaneous base forces were one order of magnitude larger than the period-averaged values since the force signals were oscillatory and produced very small mean values. The relative error of the instantaneous forces was one order of magnitude smaller and did not exceed the 2%.

6.3.3. Plant motion

When the dependence on the horizontal coordinate was incorporated, the stem experienced a larger displacement in the direction of propagation and a smaller backwards motion, as illustrated in Figure 45. The second effect was dominant, which resulted in smaller plant excursions over a wave period.

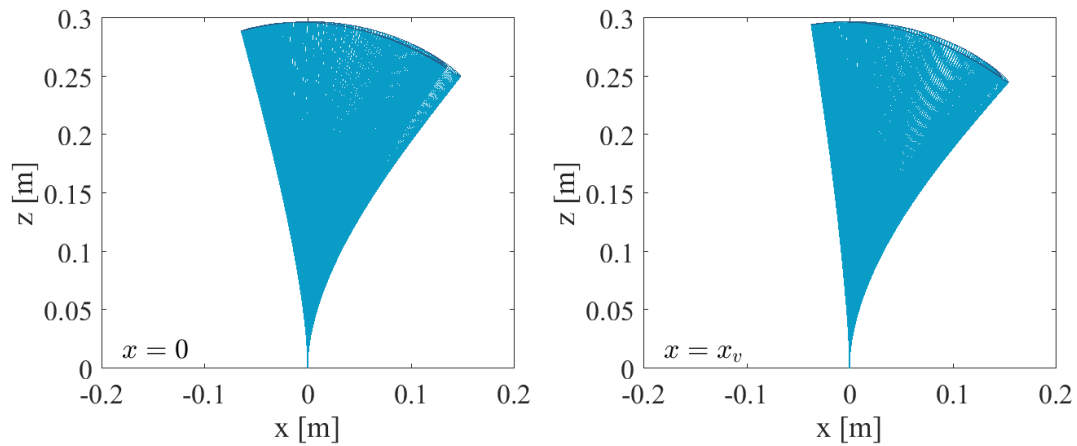


Figure 45. Plant motion for $H = 0.1$ m and $T = 2$ s computed using linear wave theory without horizontal variations in the velocity field (left) and calculating the velocities as a function of the position of the stem segments (right).

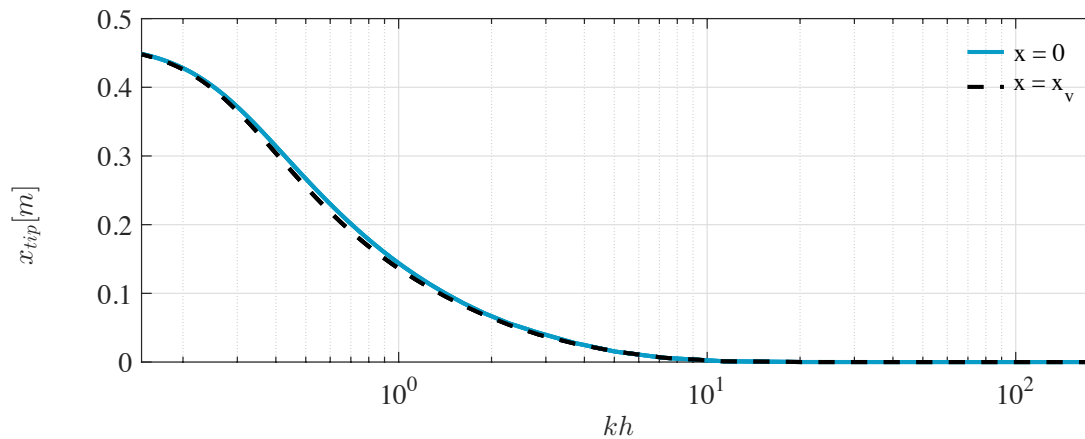


Figure 46. Total amplitude of the horizontal motion of a stem, $x_{tip} = x_{max} - x_{min}$ as a function of kh for $H = 0.1$ m.

The differences in the predicted motion were analyzed for $H = 0.1$ m and a number of wave periods ranging from $T = 0.5$ s to $T = 7$ s, as shown in Figure 46. For the shortest waves the stem motion was practically zero and all the segments were exposed to the velocity field at $x = 0$. Therefore, neglecting the horizontal coordinate did not introduce significant errors in the computations. The dependence of the flow on the horizontal coordinate also had a negligible effect for the largest periods, since the velocity variations occurred over distances that were considerably longer than the plant displacement. The most important discrepancies were obtained for intermediate frequencies.

The relative error was analyzed in order to quantify the magnitude of the differences for different wave frequencies. The error was evaluated calculating the difference in the predicted tip excursion with and without including the horizontal coordinate, $\Delta x_{tip} = x_{tip,v} - x_{tip,0}$, and dividing such value by excursion modelled using $x = x_v$. As it can be observed in Figure 47, for the shortest waves there is an increase in the error with decreasing relative depth up to a value of $kh = 0.8$ ($T = 1.85$ s), where there is a maximum relative error approximately equal to 6%. For longer waves there is a reduction of the relative error with decreasing kh .

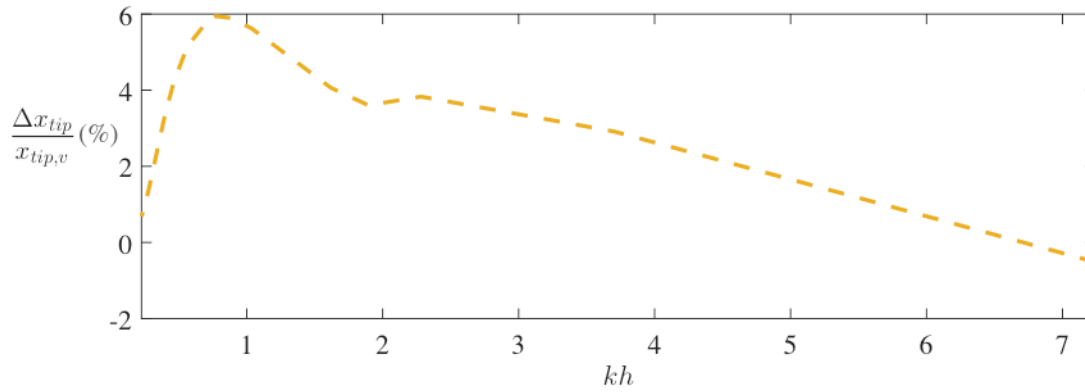


Figure 47. Ratio (%) of the difference between the maximum excursion for linear wave theory with $x = x_v$ compared to $x = 0$, relative to prediction including spatial variations for $H = 0.1$ m.

6.4. Eulerian flow

The effect of the mean return flow was incorporated adding the mean current defined by equation (2.21) to the velocities obtained using linear wave theory.

$$u(x, z, t) = \frac{\pi H \cosh k(z+h)}{T \cosh kh} \cos(kx - \omega t) \quad (6.10)$$

$$w(x, z, t) = \frac{\pi H \sinh k(z+h)}{T \sinh kh} \sin(kx - \omega t) - \omega k a^2 \frac{\pi H \cosh 2k(z+h)}{2 \sinh^2 kh} \quad (6.11)$$

6.4.1. Base forces

The influence of the Eulerian flow on the computed base forces is illustrated in Figure 48.

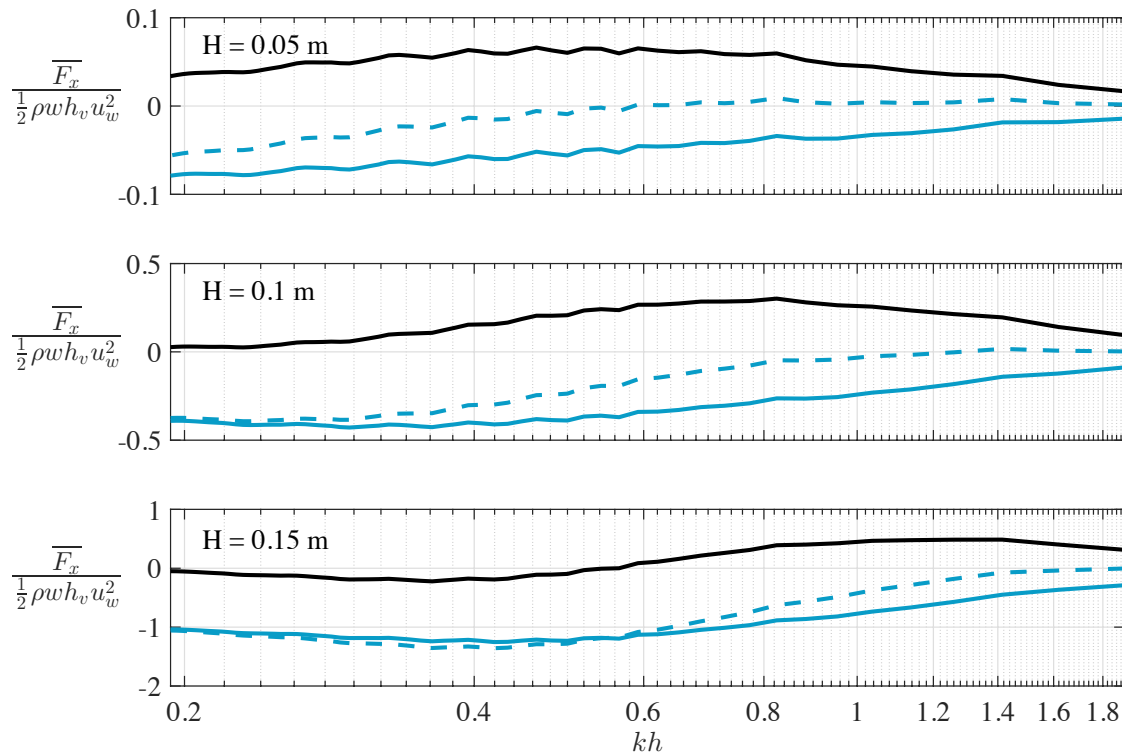


Figure 48. Wave-averaged dimensionless base force as a function of kh for $H = 0.05$ m (top), $H = 0.10$ m (center) and $H = 0.15$ m (bottom). The result of linear wave theory with $x = 0$ and $\bar{u} = 0$ is represented by a black line (—). The result of linear wave theory with $x = 0$ and $\bar{u} = u_e$ (including Eulerian flow) is plotted in a solid blue line (—). The result of linear wave theory with $x = x_v$ and $\bar{u} = u_e$ (including both the horizontal coordinate and the Eulerian flow) is represented by the blue dotted line (---).

The dimensionless mean force was one order of magnitude larger when the mean flow was implemented. Unlike the oscillatory motion, the return current did not reverse its direction over the wave cycle and produced larger and negative period-averaged values. The strength of the current increased with larger wave heights and longer periods.

The inclusion of the variations of the flow velocity along the horizontal coordinate had a relatively lower effect than the mean flow. The error associated with the assumption of $x = 0$ showed a weaker dependency on the frequency for the lowest wave height. For the largest waves, the resulting base force had similar values with or

without including spatial variations of the flow field for the highest periods. Nevertheless, the relative importance of the variations of the flow along stem increased with the frequency. Calculating the velocity at the actual position of the segments for short waves produced larger loads in the direction of propagation, which compensated the effect of the return current and reduced the magnitude of the negative base forces.

6.4.2. Plant motion

The Eulerian flow increased the displacement of the stem against the direction of wave propagation and resulted in more symmetric trajectories over the wave cycle, as it can be observed in Figure 49.

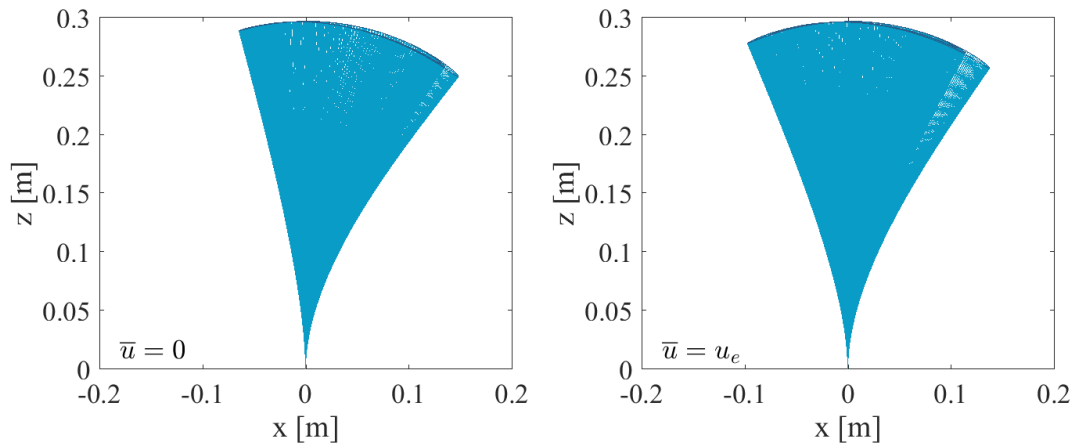


Figure 49. Stem trajectory over a wave period for $H = 0.1$ m and $T = 2$ s, without Eulerian flow ($\bar{u} = 0$) and modelling the return current \bar{u}_e using equation the expression by Phillips (1977).

6.5. Second order Stokes waves

The velocities associated with higher harmonics were calculated using equation (2.22) and equation (2.23) and adding the non-linear terms to results of linear wave theory.

$$u(x, z, t) = \frac{\pi H \cosh k(z+h)}{T \cosh kh} \cos(kx - \omega t) + \frac{3}{16} c(kH)^2 \frac{\cosh 2k(z+h)}{\sinh^4 kh} \cos 2(\omega t - kx) \quad (6.13)$$

$$w(x, z, t) = \frac{\pi H \sinh k(z+h)}{T \sinh kh} \sin(kx - \omega t) + \frac{3}{16} c(kH)^2 \frac{\sinh k(z+h)}{\sinh^4 kh} \sin 2(\omega t - kx) \quad (6.14)$$

6.5.1. Base forces

The effect of including higher-harmonics on the modelled base forces is illustrated in Figure 50.

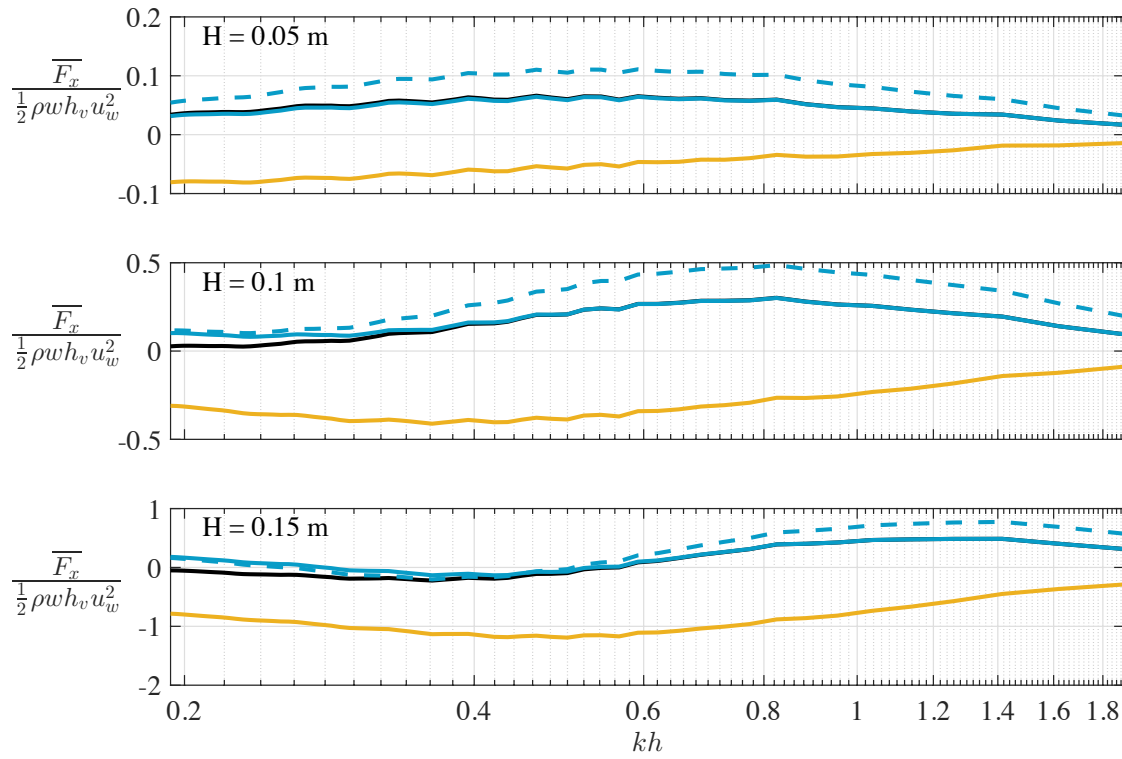


Figure 50. Wave-averaged dimensionless base force as a function of the kh for $H = 0.05$ m (top), $H = 0.10$ m (center), $H = 0.15$ m (bottom). The result of linear wave theory with $x = 0$ and $\bar{u} = 0$ (without horizontal variations or Eulerian flow) is represented in a black line (—). The base-force produced by a Stokes wave with $x = 0$ and $\bar{u} = 0$ is represented in a solid blue line (—). The result for a Stokes wave with $x = x_v$ and $\bar{u} = 0$ is shown in a dotted blue line (---). The base-force produced by a Stokes wave with $x = x_v$ and $\bar{u} = u_e$ is plotted in a solid yellow line (—).

The addition of the non-linear terms had a negligible effect for the smallest wave. Nevertheless it produced larger positive base forces for the lowest frequencies when the wave height increased. Conversely, the effect of including the dependency on the horizontal coordinate was negligible for the longest periods and became more significant for the largest values of kh , in accordance to the results of the previous sections. When all the effects were combined (return current, variations along the horizontal and wave-non linearities), the Eulerian flow was dominant and produced negative mean forces at the base.

6.5.2. Plant motion

The inclusion of higher-harmonics in the velocity enhanced the asymmetric motion of the plants in the direction of propagation of the waves, as it can be observed in Figure 51.

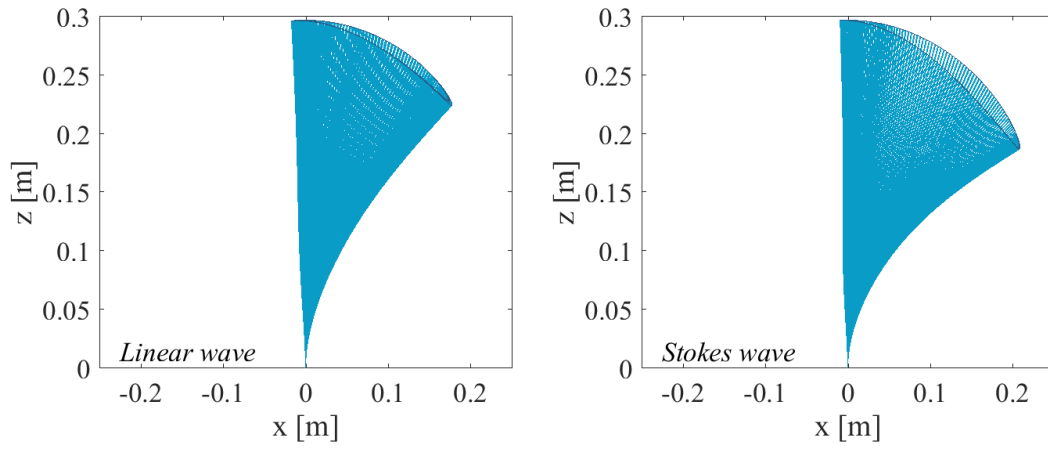


Figure 51. Stem trajectory over a wave period for $H = 0.15$ m and $T = 2$ s, for a linear wave (left) and for a Stokes wave (right), without accounting for the variations of the velocity over the horizontal coordinate or the Eulerian flow.

7. Discussion

7.1. Plant posture and stem excursion

For the case of a depth-uniform oscillatory flow the computed trajectory of the plant was symmetric over the wave period. The effect of varying the velocity over the water column, with faster flow motion near the surface and lower speed close to the bottom, was introduced using linear wave theory. For short periods and small and moderate wave heights the plant motion was symmetric. However, a residual displacement in the propagation direction appeared when waves became longer and higher. This effect was present in spite of the symmetry of the velocity profile over the wave period and without including non-linear effects in the flow velocities. The total excursion over the wave cycle tended to become symmetric again when the periods became very long and the flow during each half period resembled a uni-directional current.

The initial phase of the wave at the first timestep was also modified in a series of runs. This resulted in differences in the modelled plant motion at the beginning of the simulations, but the solutions converged to the same behaviour after a few wave periods, as shown in the Appendix D. This result seems to support the idea that the asymmetrical plant excursion was being driven by the orbital motion (Döbken, 2015). The concept is illustrated in Figure 52.

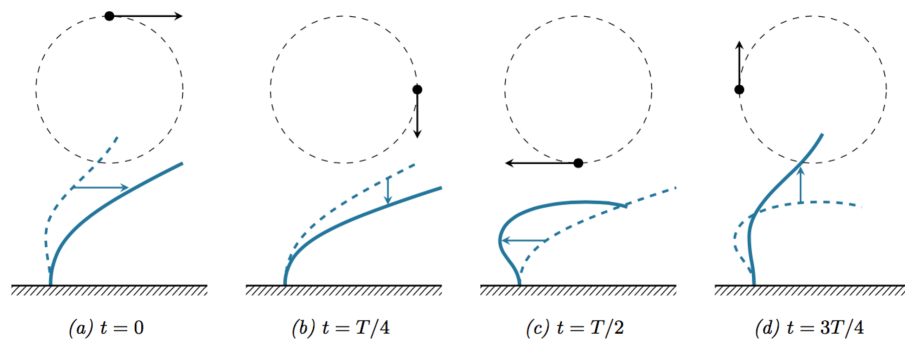


Figure 52. Asymmetric motion of flexible vegetation under waves. Source: (Döbken, 2015)

Assuming an initial phase of $\varphi = 0^\circ$ and drag-dominated conditions, positive velocities and the associated drag forces in the first part of the cycle would extend the plant in the forward direction (Figure 52 a). Downwards directed orbital velocities would subsequently push the vegetation into lower elevations in the water column (Figure 52 b). Therefore, the elliptical path of the flow would result in streamlined and drag reducing positions when the orbital velocities were negative (Figure 52 c). The negative drag forces would not be as high as the positive loads, which would produce a smaller horizontal displacement against the direction of propagation, and a more upright position of the plant under the wave trough compared to the crest (Figure 52 d). Considering $\varphi = 180^\circ$ (i.e. negative velocities at the beginning of the simulation), the initial flow would move the plant against the travelling wave, but it would be followed by upwards directed water motion that would extend the stem to a more vertical position. This would increase the area exposed to the positive orbital velocities and after a few wave cycles the excursion would also be asymmetric in the direction of the waves.

The highest modelled waves were steep and non-linear and their associated velocity field would differ from that derived using linear wave theory. The behaviour of a stem under the same wave condition would also change, since different loads would act on it. In order to represent the flow kinematics when higher order effects become important, the velocities were calculated in Dynveg using 2nd order Stokes Theory. The inclusion of wave non-linearity enhanced the asymmetry of the modelled trajectory, especially for the highest waves. The residual motion was also more pronounced for higher periods when non-linear waves were used as an input.

The described behaviour is consistent with the findings of laboratory experiments and field observations. The results of these simulations cannot be directly compared to the experiments conducted by Bakker (2015) with flexible vegetation, in spite of using the geometrical and mechanical properties of Mimic 2 as an input in the model. The drag and inertia coefficients were given typical values for rectangular cross-sections from the literature and were kept constant during the runs, with $c_D = 2$ and $c_M = 2$. However, their actual values and dependence on flow properties was unknown. Force coefficients had already been shown to vary with the Keulegan Carpenter number for the most rigid mimic, as indicated in Section 5. The calculated drag coefficients remained relatively constant, with $c_D = 2$, while the inertia coefficients varied between $c_M = 2$ for low Keulegan Carpenter numbers until $c_M = 4$ for the highest values of KC (Figure 24). Even though inertia forces are smaller than the drag for the latter case, a different value of c_M could result in considerable differences in the predicted stem deflection during flow reversals, when flow acceleration becomes important and inertial loading is dominant. Deriving drag and inertia coefficient for the flexible mimics would require additional procedures, which are explained in the recommendations section and in Appendix E. However, despite the difference in the coefficients, the modelled trajectories of Mimic 2 displayed the same trends than the experimental results. Symmetrical motions were reproduced for lower wave heights and periods. Longer deflections under the wave crest and more upright positions under the trough were experienced under the largest wave heights and periods.

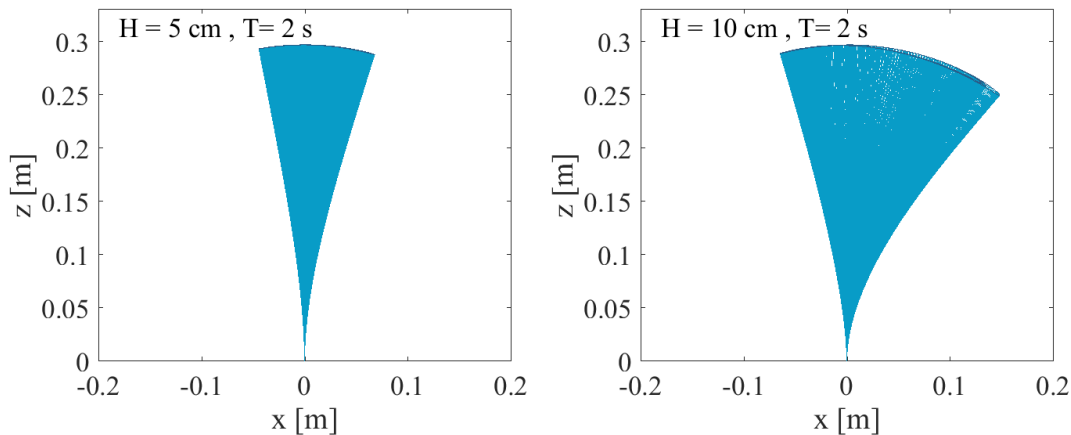


Figure 53. Comparison of the motion of the stem over the wave period modelled with Dynveg using linear wave theory with $x = 0$ without including the effect of the Eulerian flow or higher harmonics. The smaller wave (left) produced a more symmetric trajectory, whereas a residual displacement in the direction of wave propagation was obtained for the higher wave (right).

Luhar et al. (2010) associated the observed asymmetry in blade posture under waves to the drift induced by the canopy (introduced in Section 2, and further discussed in Section 7.5). Both experimental and numerical model results by Luhar and Nepf (2016) showed an asymmetrical plant excursion in the direction of wave propagation under high waves, without including the effect of the Eulerian flow within the vegetation. They attributed such behaviour to the forward velocities under the crest being larger than the backward velocities due to the presence of higher harmonics in the velocity signal. Nevertheless, the results obtained with Dynveg seem to suggest that the residual displacement is already present when the velocities are symmetric, although it is enhanced by non-linearities in the velocity profile.

The dependency of the plant behaviour on the vertical variation of the flow field may have important implications on both experimental studies and numerical models of plant motion. U-tubes have been widely used as a tool to study oscillatory forces on cylinders, for instance in laboratory experiments by Sarpkaya and Isaacson (1981) or Bearman et al. (1984) among others. A U-tube is a structure consisting of two vertical limbs at the sides and a horizontal section at the middle, where the object to be tested is attached. Water is forced to oscillate within the

tube at the resonant frequency by a horizontal plate or by a cylinder moving up and down at one of the lateral limbs (Williamson, 1984). The corresponding set-up is shown schematically in Figure 54.

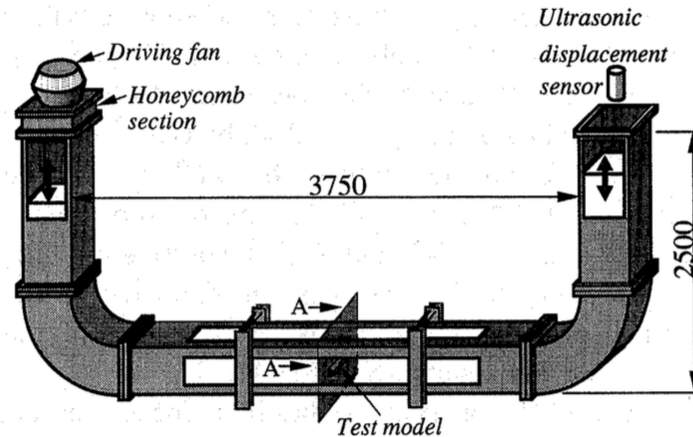


Figure 54. Schematic representation of a U-tube. Source: (Okijima, 1998)

Flow visualization tests, such as Laser Doppler Velocimetry or Particle Image Velocimetry, are easier to perform in U-tubes in comparison to an open wave flume (Faltinsen, 1993) and this feature may turn them into attractive candidates to obtain simultaneous measurements of flow velocities and plant posture. Nevertheless, they generate velocity profiles with a constant magnitude along the water column.

Since they do not reproduce the orbital motion of the water particles neither the variations of the velocity along the vertical coordinate, the tested stems would be exposed to forcing conditions that would not correspond to those generated under waves in the field (except under the shallow water regime, where the trajectories of the particles consist on a back and forth current), and the associated plant behaviour would not be the same either. Similar considerations can also be applied to the use of depth-averaged flow models to compute plant motion under wave-induced oscillatory flows.

7.2. Relative plant velocity

The motion of the stem was not in phase with the flow periods for most cases. The upper part of the plants was slightly advanced in time with respect to the water motion, and it displaced at a higher speed (Figure 35). Lower segments of the plant had smaller velocities, tending to zero towards the base. Bradley and Houser (2009) had already suggested that in spite of the widely-accepted idea that plants passively follow the flow, plant motion was observed not to be passive in most of the cases. Moreover, the phase-lead by plant motion has also been identified by other authors (Mullarney and Henderson, 2010; Zeller et al., 2014).

In a number of field experiments, Mullarney and Henderson (2010) measured water velocities using a velocimeter and plant posture was simultaneously captured with a video camera. Measurements under low energy wind waves (with $T = 2$ s) displayed the previously exposed behaviour. They also compared the field observations with the results of an analytical model based on the linearized Euler-Bernoulli equations. Model results showed that plants led water motion with phase differences decreasing from 90° to 0° with increasing wave frequency. Their field observations revealed that the relative phases could actually be larger than 90° , up to 120° .

The dependence of the phase difference between water and plant velocities on the wave period was not investigated in detail in the present study, and is discussed in more depth in the recommendations section. Nevertheless, a direct comparison would not be possible for the present velocity field, neither with the model nor the experimental results. Mullarney and Henderson (2010) recorded field velocities that include Eulerian flow and

the superposition of different wave components. Besides, their model is based on the assumption of small deformations, which is violated in most of the runs with $T = 2 \text{ s}$.

Stevens et al. (2001) obtained field measurements of the movement of subtidal kelp fronds under waves of $T = 2.8 \text{ s}$. The relative motion was always non-zero in their observations. The plants followed the water flow during the rising velocity phase until just prior the crest, when the limitation associated with their tether slowed down the plant. This resulted in wave and kelp motion being slightly out of phase. Plant velocity was also larger than water velocity according to their measurements. Again, accurate comparisons are not possible since their measurements contained additional effects (non-zero mean flow, etc.) and the geometric and mechanical properties of a kelp deviate to those of the sea grass-like mimic that was modelled with Dynveg. But the main trends in relative plant motion described above were also reproduced by the model, which provides confidence in its performance.

The present work also analyzed periods higher than those measured in the field by the previous authors. For the longest waves, plants also accelerated with the flow until they started to be limited by their attachment and slowed down. But longer periods resulted in stems reaching their maximum deflection and staying still during part of the wave cycle, with the relative velocity being equal to the flow velocity and the plants behaving as effectively rigid. For this portion of the wave phase, the reduction in exposed area was considerable. This occurred until flow reversal took place, when plants accelerated in the opposite direction and moved again leading the flow. Bradley and Houser (2009) analyzed vegetation height in the field, and found that under high-energy conditions the canopy is extended and streamlined in the direction of the flow for a longer part of the wave-cycle. Such observations correspond to the region of zero plant motion in the velocity time-series modelled with Dynveg for very long waves.

7.3. Base forces

The wave-averaged dimensionless base forces were also analyzed for a series of wave conditions, initially using linear wave theory and then adding second order effects in a later step. The shortest modelled waves were effectively in deep water. Under such waves, the drag force on the stem was comparatively smaller than inertia, and its effects were restricted to the upper part of the water column (Figure 36). The resulting mean force at the base was approximately equal to zero for this case (Figure 32). Longer periods resulted in asymmetric plant posture, as exposed in Section 4. The asymmetry in stem motion was associated with small and positive base forces over the wave cycle, with a maximum (dimensionless) value of 0.2 for waves with $H = 0.1 \text{ m}$ and 0.5 when the wave height was $H = 0.15 \text{ m}$. A further increase of the period showed a region of negative base forces for the higher and non-linear waves. In those cases, the distributed forces in the upper part of the plant were positive.

It was previously explained that plants moved faster than the flow. Such motion was faster when the oscillatory velocities were negative. Therefore, the positive relative velocities had a higher magnitude than the negative ones and produced net positive distributed forces at the upper part of the plant. In the lower positions, the fact that the deflection was larger when the flow moved in the direction of propagation resulted in (1) lower elevation of a stem when the velocities were positive and (2) smaller values of the drag coefficient given the larger deflection angle during the forward motion. As a consequence, the wave-averaged distributed force was negative at the lower region of the stem. Since the distributed loads of the lower positions had a higher magnitude, the integrated value of the force was negative.

When second order Stokes waves were introduced in the model, the effect of the larger flow velocities during the wave crests in comparison to the slower water motion during the trough produced drag forces with a higher magnitude in the forward wave phase, and a positive mean value at the base except for a small range of periods between $T = 1.47 \text{ s}$ and $T = 1.53 \text{ s}$. This suggests that the negative average base forces that were previously

obtained for the lowest frequencies were the mathematical response of the system to a prescribed velocity field that did not properly represent the properties of the flow under non-linear waves. When their characteristics were appropriately incorporated, the negative values disappeared.

For the longest waves, the behaviour of the plant during each half period was very similar (the conditions resembled a unidirectional current) and the base forces tended to zero phase-averaged values.

7.4. Effect of spatial variations in the velocity field

As a stem extends in the direction of the flow, the segments along its length are exposed to different flow speeds due to the spatial variations in the velocity field. This effect is illustrated in Figure 55. The dashed blue line represents the surface elevation at $t = t_0$ and the solid blue line corresponds to $t = t_1$. The initial position of the plant $x(t_0) = 0$ is shown by a dashed green line and the position at $t = t_1$, $x(t_1) = x_v$ is represented by a solid green line. Since the hydrodynamic loads push the plant in the direction of wave propagation, the upper part of the stem is still exposed to positive velocities at $t = t_1$, whereas at its initial horizontal position flow reversal is taking place, and the flow velocity is equal to zero. This effect reduces down in the water column, when the amplitude of the motion decreases and the position of the stem does not change significantly over time ($x(t_1) \approx x(t_0) \approx 0$).

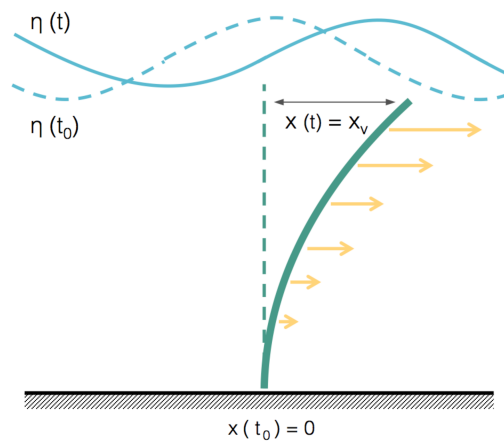


Figure 55. Schematized illustration of the phase lag effect. The dashed blue line represents the initial surface elevation ($t = t_0$), the solid blue line corresponds to the surface elevation at the present time ($t = t_1$). During the time interval $\Delta t = t_1 - t_0$ the plant moves from $x(t_0) = 0$ to $x(t_1) = x_v$. The difference between the velocity computed keeping $x(t) = 0$ compared to using $x(t) = x_v$ is representing using yellow arrows. The size of the arrows reduces down in the water column, where the motion of the plant is smaller.

In order to evaluate how spatial variations affect the computed forces and motion, the same wave conditions were run using linear wave theory, firstly assuming that $x = 0$ for all the elements and secondly calculating the flow velocity at the stem segments as a function of their horizontal coordinate, $x = x_v$. The properties of the vegetation were kept equal to those of Mimic 2. As it was observed in Figure 43, the curves of the velocities as a function of time were similar in the accelerating phase of the wave cycle, where the flow velocities increased in the propagation direction until reaching a maximum value. However, since the tip swayed with the flow and followed the wave during its forward movement, it continued experiencing positive velocities up to the point of maximum deflection, where the stem stopped and finally experienced the flow reversal. As a consequence, the area of positive velocities in extended over an interval larger than half of the wave period when the velocities were calculated using $x = x_v$. The associated drag forces were also larger with respect to linear wave theory with $x = 0$. The difference was on the order of 40% in a wave-averaged sense, but the deviations of the instantaneous value of the force did not exceed 2%. The incorporation of the spatial variations of the velocity

along the stem produced larger deflections in the direction of wave propagation. Such differences were also small and were lower than 6% of the total excursion for the modelled runs.

According to the previous results, the variation of the velocity field along the horizontal coordinate had a smaller influence on plant behaviour compared to the depth-dependency of the oscillatory flow. This implies that neglecting changes in the horizontal coordinate (for instance, using 1DV models to compute the hydrodynamics, or measuring the velocities at one single location in laboratory experiments) may be a valid assumption as long as the velocity profile is defined over the water column. The inclusion of spatial variations, with a three dimensional (3D) model, a laterally averaged two-dimensional (2DV) hydrodynamic model or measuring the flow velocities at several horizontal locations along a deflected stem in the laboratory, would increase the complexity of the problem without leading to a significant increase of accuracy.

Nevertheless, the previous conclusion can only be applied to the tested conditions. Variations of the velocity along the horizontal coordinate may have a higher importance for more flexible plants or under more energetic wave conditions, and more complex methods would be required for those cases.

7.5. Eulerian flow

As it was indicated in Section 2, water particles under waves describe orbital motions that are not closed resulting in a residual mass transport in the direction of wave propagation. In the presence of a confined boundary, the Lagrangian drift is compensated by a mean return flow in the opposite direction. The Eulerian flow was implemented in Dynveg using the expression by Phillips (1977).

The inclusion of a negative mean current enhanced the displacement of the stems against the direction of wave propagation, compensating the effect of the orbital motion on plant posture. The base forces over a wave cycle were negative and considerably larger when the Eulerian flow was included, since unlike the pure oscillatory flow, the mean current did not change its direction over the wave period.

Such a description of the vertical velocity profile is applicable for the set-up considered, when one single stem is modelled and its effect on the hydrodynamics can be considered negligible. However, the cumulative effect of a community of plants results in additional drag within the canopy, which produces a mass drift in the direction of wave propagation as explained in Section 2. Such current can be present at the top of the meadow or all over its height, depending on plant and flow properties. The streaming would expose aquatic vegetation to forces acting in the opposite direction than those obtained using equation (2.21). Therefore, the results of this Section do not represent the behaviour of a community of macrophytes in the field and cannot be compared with empirical observations.

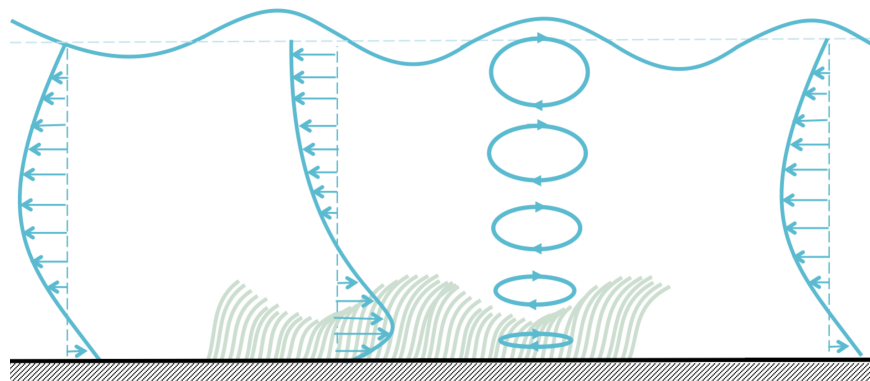


Figure 56. Comparison of the mean velocity profile inside and outside of a meadow. The undisturbed profile shows the effect of the boundary layer streaming close to the bottom. Adapted from: (Luhar et al., 2010).

7.6. Formulation of the drag

Several studies in the literature have modelled the motion of a blade using values of the drag coefficient derived for cylinders under steady flow (Mullarney and Henderson, 2010) or for smooth infinite flat plates (Abdelhrman, 2007; Luhar and Nepf, 2011; Luhar and Nepf, 2016). As it was already mentioned in Section 2, drag coefficients obtained from large-scale objects may not be applicable to aquatic vegetation of smaller dimensions due to differences in the way that they interact with the flow. Besides, some of those models cited above neglected the influence of the angle of attack on the drag. For instance, very flexible vegetation may remain extended in the direction of the flow during most of the passage of the waves, and in that case the drag would be predominantly viscous (Nikora and Nikora, 2007). Dijkstra et al. (2006) conducted a series of experiments using plastic strips, with properties similar to those of eelgrass *Zostera Marina*. Such experiments were described in Section 2 and they allowed accounting for both plant deflection and differences in scale. In order to evaluate the relative importance of the described effects three formulations were compared, (1) a constant value of the drag, (2) the same value of drag coefficient projected according to the cross-flow principle (formulation by Hoerner (1965) in Section 2) and (3) the empirical formulation by Dijkstra et al. (2006). The main difference between (2) and (3) was that the expression by Dijkstra et al. (2006) incorporated the enhancement of the drag as the elements lie parallel to the flow for very large deflections.

The multiplication of the drag coefficient by a cosine term introduced a reduction of its value for segments at upper positions of the water column. Larger deflection angles resulted in lower values of hydrodynamic forces. Since the constant formulation of the drag did not experience such a decrease, it produced larger forces and more pronounced deflections of the stem than the other two. For $H = 0.1 \text{ m}$ and $T = 3.5 \text{ s}$ mean horizontal position of the tip was a 25% larger when c_D was kept constant in comparison with the expressions that depended on the incidence angle. These results suggest that neglecting the variations of the drag coefficients with the angle of attack can lead to considerable differences in the predicted plant motion. The difference between the projected c_D and the empirical formulation from plastic strips was comparative smaller, of 12.5%. The effect of the tangent term in the formulation by Dijkstra et al. (2006) was only relevant for the moments of maximum excursion over the wave period. Nevertheless, the present result shows that its influence is not negligible and that not introducing it could lead to significant errors in the predictions of the motion, especially under large waves and with low plant stiffness.

Several additional considerations must be borne in mind. Formulations (2) and (3) include the relative orientation between the flow and the plant assuming that the cross-flow principle is valid in all cases, neglecting those values of θ which are out of the range of applicability. Besides, for oscillatory flows with $8 < KC < 20$ even small deviations from $\theta = 90^\circ$ result in the disruption of the vortex street and considerable changes in the force coefficients (Sumer and Fredsøe, 2006).

Although the coefficients were implemented as a function of the angle of attack, variations of the flow structure along the stem were neglected. Pressure recovery near the tip (already presented in Section 2) results in lower values of c_D at such position. Using the same value at every location would produce an overestimation of the forces and the associated motions at the tip (Luhar and Nepf, 2016).

The influence of the Keulegan Carpenter number and the Reynolds number was not analyzed or incorporated in any of the runs. Nevertheless, Dijkstra et al. (2006) concluded that for the rectangular plastic strips tested under steady flow the dependence of c_D on Re was very small, with $c_D \cong 2$. The coefficients derived for Mimic 4 (the stiffest stem analyzed by Bakker, with a squared cross-section) under oscillatory flow also remained approximately constant and equal to $c_D = 2$ over the range of KC considered, as shown in Figure 24. A procedure to derive force coefficients for the tested flexible mimics is suggested in Section 8 and applied in

Appendix E. This would provide information on the behaviour of flexible stems under waves with varying cross-sectional shapes.

The adjustment scale of the turbulent and viscous boundary layer over macrophytes occurs sufficiently rapid (i.e. 1 s) for steady state conditions to develop even with rapid change in the background flow (Stevens and Hurd, 1997). The smallest period tested in the experiments was $T = 1$ s. Lower periods were modelled in Dynveg, starting with $T = 0.1$ s, for which values of c_D derived from experiments where the boundary layer was fully developed are not applicable, and deviations from the computed behaviour can be expected.

Unsteady vortex shedding cannot be reproduced in the present set-up. Resonance could be triggered if the frequency of such events was equal to the natural frequency of the stem (Luhar and Nepf, 2016). The undamped natural frequency f_n for Mimic 2 can be estimated using the following expression (Blevins, 1984):

$$f_n = C_n \sqrt{\frac{EI}{h_v^4(\rho_v w t + \rho c_M(\pi w^2/4))}} \quad (7.1)$$

Where EI is the flexural strength, h_v is the length of the stem, w is the width, t is the thickness, ρ_v is the density of the vegetation, ρ represents the density of the fluid and $C_n = 0.56$ is a constant. The application of equation (7.1) results in a resonance frequency of $f_n = 0.39$ Hz. Vortex shedding for steady flows occurs for values of the Strouhal number of around 0.2 (White, 2008). The Strouhal number represents the normalized shedding frequency and is given by:

$$St = \frac{f w}{u_w} \quad (7.2)$$

Where f is the frequency of vortex shedding, u_w is the orbital velocity and w is the width of the cross-section. Assuming $0.1 < u_w < 0.4$ m/s and with $w = 0.01$ m for Mimic 2, the frequency of the vibrations ranges between $2 \leq f \leq 12$ Hz. This interval is far from the fundamental frequency of the stem. Inclusion of the effect of damping would shift the natural frequencies of the plant to lower frequencies, which would make the separation even larger. Nevertheless, the previous value of St corresponds to steady unidirectional flows. Since the Keulegan-Carpenter number is the inverse of the Strouhal number, the analysis of the force coefficients as a function of KC for Mimic 2 could provide a better insight on the values of St for which vortex shedding was relevant during the experiments (Luhar and Nepf, 2016).

7.7. Wave dissipation

The wave-averaged dimensionless dissipation, defined in equation (6.5), was evaluated for a stem under the same wave condition and geometry but varying its stiffness (Figure 37). For the highest values of the elastic modulus the motion of the plant was negligible, and the relative velocities were equal to the flow velocities. This resulted in the largest values of dissipation. A further reduction of the rigidity led to appreciable tip motions, of the order of the 20% of the plant height for a stem of $h_v = 30$ cm. Nevertheless, the dissipation was the same to that of a completely stiff plant; for the sake of wave attenuation the stem was effectively rigid. The previous result seems to support the assumption that, under certain conditions, the motion of the plant can be disregarded and vegetation can be assumed to be rigid. Bradley and Houser (2009) had already justified the idea based on empirical results, since plants were observed to be effectively rigid for high Reynolds numbers. As the plant became more flexible, the upper part of the stems swayed with the waves for a longer time, diminishing its relative motion with respect to the water and consequently reducing the work.

As it was explained in Section 2, wave attenuation depends on the flexibility of the vegetation and on the relative scale of the geometry of the plant with respect to the orbital excursion (h_v/A). When the effect of the length of the

vegetation was incorporated, small differences in the dimensionless work arose for the highest rigidities. A shorter stem produced slightly less dissipation. Even though the work was divided by the height of the vegetation, a smaller plant is exposed to lower velocities in the water column that do not relate linearly to its size. For the largest flexibilities, a longer stem was able to sway with the flow and reduce the relative velocity over a larger fraction of the wave period, resulting in larger excursions and less attenuation. A shorter plant reached its maximum deflection sooner, and remained extended and aligned with the flow during most of the passage of the wave, subsequently producing more work over the period. Such trends were in accordance with the existing literature, for instance with observations by Gaylord and Denny (1997) and Luhar and Nepf (2016).

The representation of the dimensionless mean dissipation against the Cauchy number resulted in the convergence of the curves of different stem lengths. The collapse was not perfect; the dimensionless dissipation was approximately a 10% larger for the shorter plant for intermediate values of Ca . Nevertheless, the similarity of the curves seems to support the role of Ca dictating plant reconfiguration (Luhar and Nepf, 2013). It should be taken into account that there is some ambiguity in the definition of the Cauchy number used in the present work. Ca was defined using the orbital velocity at the bottom. Different combinations of a and T could produce the same value of u_w at the base of the stem but would result a different variation of the velocity profile and the induced drag forces along its height (Luhar and Nepf, 2016).

Several conclusions can be extracted from the previous analysis. In the first place, a considerable number of studies have analyzed wave attenuation neglecting plant motion and approximating vegetation stems as rigid cylinders (for instance, Dalrymple et al., 1984; Kobayashi et al., 1993, among others). Such approach has often been considered inappropriate for highly buoyant and/or flexible vegetation, where a more complex modelization of the forces would be required (Seymour, 1996). Nevertheless, the previous results seem to support that the effect of plant motion on wave dissipation can be negligible even with appreciable tip excursions approximately equal to a 20% of the stem length. Besides, the relationships between vegetation-induced work and the Cauchy number suggest that there may be more simplified ways to account for plant dynamics without solving the non-linear equations of plant motion. For instance, outside of the regime of effectively rigid vegetation in Figure 38, an increase of Ca with a factor of 10 produces approximately a 50% decrease in wave attenuation. Such result cannot be generalized and it is restricted to the set-up of the runs. But similar and more general simplified expressions could be derived conducting a large number of simulations, with varying hydrodynamic conditions and plant properties.

The influence of the buoyancy was not investigated in the present study. Its effect as a restoring force would shift the onset of plant reconfiguration to higher values of the Cauchy number (Luhar and Nepf, 2011) and increase the region of values where the assumption of effective rigid plant is valid.

8. Conclusions and recommendations

8.1. Conclusions

The conclusions of the present work have been summarized in terms of answers to the research objectives, presented in Section 1.

- (1) *Validation of Dynveg for the small deformation regime. Evaluation of the model capability to reproduce the measured forces obtained by Bakker (2015) in a set of laboratory experiments using a stiff mimic. Analysis of the performance of the model predicting tip motion making use of the equation of a cantilever beam.*

Dynveg was used to model the base forces for a rigid stem under a number of wave conditions that had been tested in a series of experiments conducted by Bakker (2015). A good correspondence was found between computed and measured forces for the drag-dominated cases. Nevertheless, the modelled force signal displayed considerable noise for the wave conditions where the flow acceleration was significant. The use of a low-pass filter function removed the noise and showed that it was not being introduced by the model. The computed tip motion was also compared to the result of the expression for the deflection at the end of a cantilever beam, under a number of uniform velocity profiles. The value of the displacement was similar in both cases and only differed in the third significant digit. It was concluded that Dynveg reproduced satisfactorily both motion and base forces in the small deformation regime.

- (2) *Description of the physical processes experienced by vegetation under wave hydrodynamics using Dynveg. Analysis of how changes in the wave properties and the associated flow kinematics affect the response of a stem. Evaluation of the influence of the characteristics of the vegetation (geometry, rigidity) on wave dissipation. Qualitative comparison of the results and trends reproduced by the model with the existing literature.*

Small waves with short periods generated symmetric stem motions over the wave period. An increase of the wave height and the period resulted in a residual displacement of the plant in the direction of the wave propagation. The asymmetry in the stem excursion was obtained before including non-linear effects and without incorporating the effect of the Eulerian flow, and it disappeared when a depth-uniform oscillatory flow was modelled. The inclusion of higher-harmonics enhanced the asymmetry of the motion even further.

The modelled behaviours corresponded well with the laboratory observations by Bakker (2015) and Luhar and Nepf (2016). Luhar et al. (2010) had previously associated the observed asymmetry in plant motion to the streaming induced by the canopy. Luhar and Nepf (2016) explained it in terms of the velocities being higher under the wave crest compared to the trough for the higher and non-linear waves. Nevertheless, the results of Dynveg suggest that the residual motion is associated with the orbital motion and the variations of the velocity profile over the water column, as previously indicated by Döbken (2015).

The modelled motion of the stem was faster and advanced in time with respect to the flow in accordance to field observations by Mullarney and Henderson (2010) and Stevens et al. (2001). The value of such phase difference and its dependence on the wave frequency was not studied in further detail and it is discussed further in the recommendations section. The wave-averaged base force was also analyzed. Its value was approximately zero for the shortest waves, associated with symmetric tip excursions. Longer waves, with more asymmetric trajectories, resulted in a positive residual value at the base. A negative mean base force was initially obtained for high and very long waves, which disappeared when the effect of higher harmonics was included.

The dependence of the wave dissipation on plant stiffness was also evaluated by varying the flexural stiffness of one stem and calculating the dimensionless work under the same wave condition. Beyond a certain value of

rigidity the dissipation was the constant regardless of the value of the stiffness. Nevertheless, it was observed that the stem motion could be significant for the effectively rigid regime, with total tip excursions approximately equal to the 20% of the plant height. This implies that the assumption of negligible plant motion can be valid even for appreciable plant displacements, which could allow to simplify considerably wave attenuation models. For higher flexibilities, shorter stems produced more work due to their lower capacity to follow the waves, in accordance to the observations by Gaylord and Denny (1997) and Luhar and Nepf (2016) among others. When the dimensionless work was plotted against the Cauchy number the curves corresponded to different stem lengths converged, with maximum discrepancies of around 10% for intermediate values of Ca . Such relationships could be applied to develop simplified expressions to account for wave attenuation in computationally demanding large-scale models, where it would not be feasible to solve stem-scale processes.

(3) *Evaluation of the suitability of the use of U-tubes to study plant motion under wave hydrodynamics*

U-tubes have been widely used in laboratory studies of wave forces on cylinders and the fact that flow visualization tests are easy to conduct in them may turn them into good candidates to study plant motion under waves. Nevertheless, they reproduce depth-uniform oscillatory flows that do not allow incorporating the effect of the orbital motion and the vertical variation of the velocity profile. Simulations using Dynveg suggest that the latter effect drives plant response to wave action and that the asymmetric behaviour of the vegetation observed in the field cannot be reproduced without including it.

(4) *Analysis of the limitations associated with the use of velocity profiles computed at one single location instead of a spatially varying velocity field.*

Flexible plants may follow the waves and extend in the propagation direction until being limited by their attachment to the substratum. Since different segments of the same stem would have different horizontal locations, they would not be exposed to the same flow velocities. This effect was evaluated in a series of runs, comparing the results using linear wave theory with and without including horizontal variations in the velocity field. The difference in the instantaneous base forces and horizontal position of the tip was smaller than the 2% for all the wave conditions considered. The inclusion of the dependency of the flow on the horizontal coordinate had considerably less influence in plant motion than the variations along the vertical. For the analyzed conditions, the use 1DV models would not lead to a significant loss of accuracy. Nevertheless, the variations of the velocity along the horizontal coordinate may have a higher importance for very flexible vegetation (with rigidities smaller than the tested value) or for more energetic wave conditions.

8.2. Recommendations

Validation of the model for the experiments using flexible vegetation

The performance of Dynveg has already been validated for one single stem experiencing small deformations, both against experimental data (comparing computed and measured forces using the data-set of Bakker (2015) in Section 5) and also contrasting the modelled plant displacement with the maximum deflection at the end of a cantilever beam (using uniform distributed loads as indicated in Appendix A). An additional step could be the validation of the model for the regime of large plant motions, using the experiments conducted by Bakker (2015) with flexible mimics. A possible approach would consist of obtaining force coefficients for each of the experiments, and using those together with the recorded velocity time-series to reproduce the plant dynamics with Dynveg. The comparison of the results of the model with the laboratory measurements would allow to evaluate the quality of the predictions. The procedure is schematized in Figure 57.

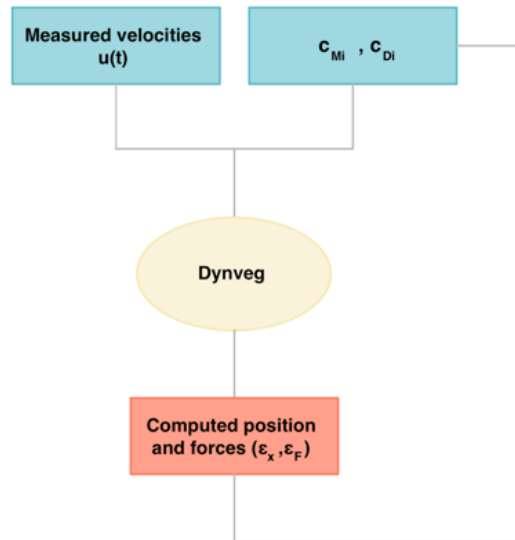


Figure 57. Flow chart representing the procedure of non-linear calibration of mean force coefficients for flexible vegetation consisting on (1) Implementing a number of coefficients (2) determining the errors (3) Calculating the error functions and (4) obtaining the pair of coefficients that minimizes the error.

For the most flexible plants, stem motion is significant and cannot be assumed to be negligible. Therefore, the mean drag and inertia coefficients cannot be directly calculated from the experimental data set as it was done in Section 3. Dynveg could be used for as a non-linear fitting tool for each of the test cases, inputting iteratively the measured velocities together with different values of the force coefficients. Error functions could be developed in order to select the pair of c_M and c_D that minimizes the difference with the computations and the measurements. The evaluation of the predictions obtained with the optimum force coefficients would allow to assess if Dynveg accurately captures the dynamics of the response of a single vegetation stem under waves. The first steps in the validation of the model using the experimental data obtained with flexible mimics are presented in Appendix E.

Validation of the model for flexible vegetation using in-canopy flow

As it has been previously mentioned, waves drive a mean mass drift in the direction of wave propagation through submerged canopies (Lowe et al., 2007). Such streaming was not generated in the experiments since they tested one-single stem in the wave flume, which had negligible influence on the flow. In the present study, Dynveg computed plant motion in response to a prescribed wave-induced velocity field. Reproducing the mean current driven by the waves within a meadow would require capturing the impact that plants have on the flow. One possibility to account for such feedback would be to measure fluid velocities inside a physical canopy and input those in Dynveg rather than using measurements for undisturbed waves. This would allow to mimic the natural system in a more realistic manner and to validate the model against field observations. Measurements of water and plant motion could also be obtained testing an artificial seagrass canopy in the laboratory. Another option would be to couple Dynveg with the momentum equations for the fluid and solve iteratively for plant and water motion. Such approach could be used to compute multiple wave conditions and different plant characteristics, and to develop more simple and less-computationally expensive frameworks to account for plant motion in large-scale hydrodynamic models.

Analysis of the eigenmodes of the vegetation in relation to wave dissipation

The passage of waves exerts oscillating stresses on the vegetation. Moreover, there is also potential for resonance phenomena if the wave frequency matches one of the natural frequencies of a plant. A stem (characterized as a structure) has a series of resonance frequencies, each of which is associated with a specific

mode of vibration. Since wave dissipation depends on the relative motion between the flow and the stem, the different fundamental shapes would result in different rates of energy loss. Mullarney and Henderson (2010) analyzed the normal modes of stems with different geometries. They computed plant motion and wave dissipation, and obtained larger attenuation when the waves excited higher and effectively more rigid modes of vegetation motion. Their results are restricted to the assumptions of their model and the cases that they tested. Nevertheless, a dynamic analysis of the modelled plants would provide a better understanding of their response under different wave conditions and help interpreting the results of the model. A way to achieve this would be to compute an oscillatory velocity signal with constant amplitude and increase its frequency at a sufficiently slow rate over time. Every time the frequency matched one of the fundamental frequencies, the amplitude of the motion would increase considerably due to dynamic effects. Besides, as it was indicated in Section 7.6, a dynamic amplification phenomenon may also be triggered if the frequency of vortex shedding matches one of the natural frequencies of the stem (Luhar and Nepf, 2016). The study of this effect would require the combination of Dynveg with a hydrodynamic model solving for the turbulent motions in the fluid. However, the comparison of the natural frequencies of the vegetation with expressions for the Strouhal number from the literature could provide a first estimate for the potential of such effect.

Analysis of wave dissipation for irregular wave spectra

Monochromatic waves have been studied in the present work. Nevertheless, the actual sea surface is the result of the superposition of multiple wave components. Bradley and Houser (2009) conducted a series of field measurements using a digital video camera to capture plant motion and an ADV velocimeter. Cospectral analysis between recorded flow and blade velocities suggested that seagrass moved in phase with the current at a lower secondary frequency and out of phase with the higher peak frequency. Since the relative velocities were larger for the latter component, short-period waves experienced more dissipation. The response of the vegetation to different periods is also linked to the natural frequencies of the plant in relation to the frequencies of the spectrum, as explained in the previous section. A dynamic enhancement of plant motion can occur for certain frequencies. This effect could be studied using the velocity field produced by the superposition of several wave components as an input of Dynveg. Relative plant motion appears to drive frequency-dependent dissipation under low energy conditions (Bradley and Houser, 2009). However, for high-energy conditions the behaviour of the vegetation as a frequency-filter seems to be more related to the degree of penetration of the oscillatory flow within the canopy. Shorter-period waves are more effective driving flow within the vegetation, since given the same wave height they generate a larger pressure gradient in the canopy compared to a longer wave. This produces larger drag forces on the stems and more attenuation for high-frequency components. The latter phenomenon could be further studied coupling Dynveg with a hydrodynamic model that solves the momentum equations including the feedback between vegetation behaviour and flow properties.

Conditions of the present study

The present work has analyzed the behaviour of stems with seagrass-like properties. Nevertheless, there is considerably diversity in the characteristics and behaviour of aquatic organisms. For instance, an alga such as the feather boa kelp, *Egregia menziesii* is so flexible that small lateral deflections result in negligible restoring forces, and the blade can move unimpeded for a wide range of motion. Not until the blade is fully extended does further deflection result in an elastic restoring force (Denny et al., 1998). Different plant properties (constant or varying along the stem) could be inputted in the model in order to evaluate the performance of Dynveg predicting the motion of different vegetation species. Moreover, the height of the plant was smaller than the water depth in all the runs. As it can be observed in Figure 13, emergent rigid vegetation results in a strong current against the direction of wave propagation inside the vegetation (Pujol et al., 2013). Such a velocity profile would exert loads

on a stem of opposite sign to those produced in a submerged canopy. The response of emergent vegetation to wave hydrodynamics could also be investigated with Dynveg under wide range of wave conditions.

Variability of vegetation properties

The attenuation of waves by vegetation is a complex process involving the coupled dynamics of water and plant motion (Zeller et al., 2014). Further complexity is introduced due to the variability in vegetation morphology, canopy heterogeneity and bottom topography among other aspects. Besides, individual plants of the same species differ mechanically from one another even when they grow in a well-controlled environment (de Langre, 2012). Given the uncertainty in the boundary conditions, even direct numerical simulation could not provide definitive results (Zeller et al., 2014). Conducting multiple field experiments could be used to derive probability distributions and typical parameters in different species of vegetation. Given the computational efficiency of Dynveg, the vegetation model could be combined with a statistical approach (i.e. Monte-Carlo simulations), to derive the probability density function of plant response for a certain plant type from the characteristics of the population obtained during field measurements (de Langre, 2012). The variability in the response would also indicate the suitability of using an average plant to represent a canopy.

Camus et al. (2011) used cluster analysis for processing large wave datasets: such a tool may also be useful for examining the outputs of the Monte-Carlo simulation to identify trends or patterns in the results, for instance, several plant typologies within the same species that display common behaviours. These kinds of studies could be also done to analyze long-term ecological effects. For instance, they could allow identifying the rate of gap formation within a meadow (de Langre et al., 2012).

As it was mentioned in the beginning of the present work, the function of coastal vegetation as a shoreline defence has gained strong interest since it can offer sustainable and cost-effective coastal protection solutions (Borsje et al., 2011). In current-dominated environments, such as a tidal region, a canopy can reduce considerably the near-bed velocities and hence the bed shear stresses (Luhar et al., 2010). Nevertheless, excessive drag can lead to stem rupture or dislodgement from the substrate (Luhar and Nepf, 2013). If a local area of meadow is lost, the diversion of the flow from the vegetated area to the adjacent bare bed can result in a feedback mechanism that maintains the fragmented structure and inhibits vegetation regrowth (Luhar et al., 2008). Such effect is not that significant for wave-dominated environments, because of the lower reduction of the oscillatory velocities by a meadow in comparison to a unidirectional flow. Studying gap formation with a Monte-Carlo analysis could have important implications to the success of future restoration attempts of ecosystem engineering species.

The use of statistical methods in combination with Dynveg could have additional practical applications, such as in the planning of field measurement campaigns. They could provide information on which vegetation parameters require a more accurate measurement because of their influence in wave dissipation. For instance, a higher sensitivity to changes in the cross-section could imply that it is necessary to take samples at several locations to characterize the geometry of the plants. The influence of the stiffness would determine if there is a need to evaluate the effective flexural rigidity of the stems using bending tests in the laboratory. If the results were only sensitive to the stem length, it could be sufficient to collect information about the vegetation height using sonar techniques and estimate the remaining parameters from the existing literature.

9. References

- Abdelrhman, M.A., 2007. Modeling coupling between eelgrass *Zostera marina* and water flow. *Marine Ecology-Progress Series* 338, pp 81–96.
- Alben, S., Shelley, M. & Zhang, J., 2002. Drag reduction through self-similar bending of a flexible body. *Nature* 420 (6915) pp.479–481.
- Batchelor, G.K., 2000. *An Introduction to Fluid Dynamics*. Cambridge University Press.
- Bakker, W., 2015. The wave-forced motion of submerged flexible vegetation. Laboratory experiment. Internship report. Deltares. TU Delft.
- Barko, J. W., Adams, M. S., Clesceri, N. L., 1986. Environmental factors and their consideration in the management of submersed aquatic vegetation: A review. *Journal of Aquatic Plant Management* 24, pp. 1-10.
- Bearman, P.W., Graham, J.M.R., Obasaju, E.D., Grossopoulos, G.M., 1984. The influence of corner radius on the forces experienced by cylindrical bluff bodies in oscillatory flow. *Applied Ocean Research* 6(2), pp. 83–89.
- Blevins, R.D., 1984. *Fluid Dynamics Handbook*.
- Borgman, L.E., 1972. Statistical Models for Ocean Waves and Wave Forces. *Advances in Hydrosience* 8, pp. 139-181.
- Borsje, B.W., Van Wesebeeck, B.K., Dekker, F., Paalvast, P., Bouma, T.J., Van Katwijk, M.M., de Vries, M.B., 2011. How ecological engineering can serve in coastal protection. *Ecological engineering* 37, pp.113–122.
- Bradley, K. and Houser, C., 2009. Relative velocity of seagrass blades : Implications for wave attenuation in low-energy environments. *Journal of Geophysical Research, Earth surface* 114 pp.1–13.
- Brosen, M., 2007. *Non-linear Waves*. Aalborg: Department of Civil Engineering, Aalborg University. (DCE Lecture Notes; No. 9)
- Brown, J.A., MacMahan, J.H., Reniers, A.J.H.M., Thornton, E.B., 2015. Field Observations of Surf Zone–Inner Shelf Exchange on a Rip-Channeled Beach. *Journal of Physical Oceanography*, 45 (9).
- Dalrymple, R.A., Kirby, J.T., Hwang, P.A., 1984. Wave diffraction due to areas of energy dissipation. *J. Waterw. Port Coast. Ocean Eng.* 110, pp 67–79.
- Denny, M. et al., 2012. The Menace of Momentum : Dynamic Forces on Flexible. *Limnology and Oceanography* 43(5), pp.955–968.
- Callaghan, D.P, Bouma, T.J., Klaasen, P., Van der Wal, P., Stive, M.J.F., Herman, P.M.J., 2010. Estuarine, Coastal and Shelf Science Hydrodynamic forcing on salt-marsh development : Distinguishing the relative importance of waves and tidal flows. *Estuarine, Coastal and Shelf Science* 89 pp.73–88.
- Capobianco, M. and Stive, M.J.F., 2000. Soft intervention technology as a tool for integrated coastal zone management. *Journal of Coastal Conservation* 6, pp.33–40.
- Chakrabarti, A., Chen, Q., Smith, H.D., Liu, D., 2016. Large Eddy Simulation of Unidirectional and Wave Flows through Vegetation. *Journal of Engineering Mechanics* , p. 04016048. doi: 10.1061/(asce)em.1943-7889.0001087.
- Day, M.A., 1990. The non-slip boundary condition in fluid mechanics. *Erkenntnis* 33, pp. 285-296.
- Denny, M., Gaylord, B., Helmuth, B., Daniel, T., 1998. The menace of momentum: dynamic forces on flexible organisms. *Limnology and Oceanography* 43 (5), pp. 955–968.

- De Langre, E., 2008. The effects of wind on plants: A review. *The Annual Review of Fluid Mechanics*, 40: pp 141–168.
- De Langre, E., Gutierrez, A., Cossé, J., 2013. On the scaling of drag reduction by reconfiguration in plants. *Comptes Rendus Mécanique* 340, pp.35–40.
- De Langre, E., 2012. Methodological advances in predicting flow-induced dynamics of plants using mechanical-engineering theory. *Journal of Experimental Biology*, Cambridge University Press 215, pp. 914-921.
- De Langre, E., Gutierrez, A., Cossé, J., 2013. On the scaling of drag reduction by reconfiguration in plants. *Comptes Rendus Mécanique* 340, pp. 35-40.
- Dijkstra, J.T., 2006. Macrophytes in estuarine gradients Flow trough flexible vegetation. Delft University of Technology. (PhD Thesis)
- Dijkstra, J.T., Uittenbogaard, R., Stive, M.J., 2006. Modelling hydrodynamics in eelgrass (*Zostera Marina*) beds. Delft University of Technology.
- Dijkstra, J.T. & Uittenbogaard, R.E., 2010. Modeling the interaction between flow and highly flexible aquatic vegetation. *Water Resources Research*, 46 pp.1–14.
- Döbken, J.W., 2015. Modeling the interaction of wave hydrodynamics with flexible aquatic vegetation. Master thesis. Deltares. TU Delft.
- Erduarn K.S., Kutija V., 2003. Quasi-3D numerical model for flow through vegetation. *Journal of Hydroinformatics* 5(3), pp. 189–202.
- Etnier, S.A., Vogel, S. 2000. Reorientation of Daffodil (*Narcissus: Amaryllidaceae*) Flowers in Wind: Drag Reduction and Torsional Flexibility. *American Journal of Botany*, 87(1) pp. 29-32.
- Faltinsen, O., 2013. *Sea Loads on Ships and Offshore Structures*. Volume 1 of Cambridge Ocean Technology Series. Cambridge University Press.
- Fonseca, M.S., Fisher, J.S, Zieman, J.C., Thayer, G.W., 1982. Influence of the Seagrass *Zostera marina* on Current Flow. *Estuarine, Coastal and Shelf Science* 15, pp. 351–364.
- Fonseca, M.S., Koehl, M.R.A., Kopp, B.S., 2007. *Journal of Experimental Marine Biology and Ecology* 340, pp. 227-246.
- Fredsøe, J. and Deigaard, R., 2006. *Mechanics of coastal sediment transport*. Singapore: World Scientific.
- Gallagher, E.L., Thornton, E.B., Stanton, T.P., 2003. Sand bed roughness in the nearshore. *Journal of Geophysical Research: Oceans* 108, pp.1–2.
- Gambi, M. C., Nowell, A. R. M., Jumars, P. A., 1990. Flume observations on flow dynamics in *Zostera marina* (eelgrass) beds, *Marine Ecology Progress Series* 61, pp. 159-169.
- Gaylord, B., 2000. Biological implications of surf-zone flow complexity. *Limnol. Oceanogr.* **45**, pp. 174–188.
- Gaylord, B. and Denny, M.W., 1997. Effects of size, shape and stiffness in determining wave forces on the stipitate. *The Journal of Experimental Biology* 200, pp. 3141–3164.
- Ghisalberti, M., and Nepf, H. M., 2002. Mixing layers and coherent structures in vegetated aquatic flows. *Journal of Geophysical Research: Oceans*, 107(2), pp 3-1-3-11.
- Ghisalberti, M., and Nepf, H. M., 2004. The limited growth of vegetated shear layers. *Water Resour. Res.*, 40, W07502.
- Ghisalberti, M., and Nepf, H. M., 2008. Flow and transport in channels with submerged vegetation, *Acta Geophysica* 56 (3), pp. 753-777.

- Gosselin, F., de Langre, E., Machado-Almeida, B.A., 2010. Drag reduction of flexible plates by reconfiguration. *Journal of Fluid Mechanics* 650, pp. 319–341.
- Graham, J.M.R., 1980. The forces on sharp-edged cylinders in oscillatory flow at low keulegan-carpenter numbers. *Journal of Fluid Mechanics* 97 (3), pp. 331–346.
- Greenberg, R., Maldonado, J., Droege, S. and McDonald, M.V., 2006. Tidal marshes: a global perspective on the evolution and conservation of their terrestrial vertebrates. *Bioscience* 56 (8), pp. 675-85.
- Harder, D.L., Speck, O., Hurd, C.L., Speck, T., 2004. Reconfiguration as a Prerequisite for Survival in Highly Unstable Flow-Dominated Habitats. *Journal of Plant Growth Regulation* 23, pp.98–107.
- Heideman, J. and Sparpkaya, T., 1985. Hydrodynamic forces on dense arrays of cylinders. OTC1985.
- Hemminga, M. A. and Duarte C. M., 2000. *Seagrass Ecology*, Cambridge University Press.
- Hook, D.D., McKee, W. H., Smith, H. K., James Gregory, V. G. Burrell Jr, M. Richard DeVoe, R. E. Sojka, Stephen Gilbert, Roger Banks, L. H. Stolzy, Chris Brooks, Thomas D. Matthews, T. H. Shear (1988) *The Ecology and Management of Wetlands. Volume 1: Ecology of Wetlands*, 1st edn., : Springer US.
- Hook, D.D., McKee Jr, W. H., Smith, H. K., James Gregory, V. G., Burrell Jr, M. DeVoe, R., Sojka, R. E. Gilbert, S., Banks, R., Stolzy, L. H., Brooks, C., Matthews, T.D., Shear, T. H. (1988) *The Ecology and Management of Volume 1: Ecology of Wetlands*, 1st edn., : Springer US.
- Hu, Z., Suzuki, T., Zitman, T., Uijtewaal, W., Stive, M., 2014. Laboratory study on wave dissipation by vegetation in combined current – wave flow. *Coastal Engineering* 88, pp.131–142.
- Hurd, C.L., Harrison, P.J., Druehl, L.D., 1996. Effect of seawater velocity on inorganic nitrogen uptake by morphologically distinct forms of *Macrocystis integrifolia* from wave-sheltered and exposed sites. *Marine Biology* 126, 205-214.
- Ikeda S, Yamada T, Toda Y., 2001. Numerical study on turbulent flow and honami in and above flexible plant canopy *International Journal of Heat and Fluid Flow* 22(3), pp. 252–258.
- Isaacson, M., Subbiah, K., Baldwin, J., 1991. Force coefficient Estimation from Random Wave Data. *International Journal of Offshore and Polar Engineering* 1(4), pp. 255-263.
- Jadhav, R.S., Chen, Q., Smith, J.M., 2013. Spectral distribution of wave energy dissipation by salt marsh vegetation. *Coast. Eng.* 77, pp. 99–107.
- Karleskint, G., Turner, R., Small, J.W. and SM, K.T. (2012) *Introduction to marine biology*. 4th edn. United States: Brooks/Cole, Cengage Learning.
- Keulegan, G.H. and Carpenter, L.H., 1958. Forces on Cylinders and Plates in an Oscillating Fluid. *Journal of Research of the National Bureau of Standards*, 60(5).
- Knutson, P.L., Brochu, R.A., See, W.N., 1982. Wave damping in spartina alterniflora marshes, *Wetlands* 2 pp.87–104.
- Kobayashi, N., Raichle, A.W., Asano, T., 1993. Wave attenuation by vegetation. *J. Waterw. Port Coast. Ocean Eng.* 119 (1), pp. 30–48.
- Koehl, M. A. R., 1984. How do benthic organisms withstand moving water? *Am. Zool.* **24**, pp. 57–70.
- Kozakiewicz, A., Fredspe, J. and Sumer, B.M., 1995. Forces on pipelines in oblique attack. Steady current and waves. *Proc. 5th Int. Offshore and Polar Engineering Conf.*, The Hague, Netherlands, June 11-16, 1995, 11: 174- 183.

- Kutija V, Hong H.T.M., 1996. A numerical model for assessing the additional resistance to flow introduced by flexible vegetation. *Journal of Hydraulics Research* 34(1), pp. 99–114.
- Lamberti-Raverot, B. and Puijalon, S., 2012. Nutrient enrichment affects the mechanical resistance of aquatic plants. *Journal of Experimental Botany*, 63 (127), pp. 6615–6123.
- Li, C.W. and Xie, J.F., 2011. Numerical modeling of free surface flow over submerged and highly flexible vegetation. *Advances in Water Resources* 34, pp.468–477.
- Liu, D., Zhang, Y. Chen, Q., 2016. Simulation of flow around rigid vegetation stems with a fast method of high accuracy. *Journal of Fluids and Structures* 63, pp. 1-15.
- Losada, I.J., Maza, M., Lara, J.L., 2016. A new formulation for vegetation-induced damping under combined waves and currents. *Coastal Engineering*, 107, pp.1–13.
- Lowe, R.J., Koseff, J.R., Monismith, S.G., 2005. Oscillatory flow through submerged canopies: 1 . Velocity structure. *Journal of Geophysical Research* 110, pp.1–17.
- Lowe, R.J., Falter, J.L., Koseff, J.R., Monismith, S.G., Atkinson, M.J., 2007. Spectral wave flow attenuation within submerged canopies: Implications for wave energy dissipation. *Journal of Geophysical Research* 112 C05018.
- Luhar, M., and Nepf, H. M., 2011. Flow-induced reconfiguration of buoyant and flexible aquatic vegetation. *Limnology and Oceanography*, 56(6), pp 2003-2017.
- Luhar, M., and Nepf, H. M., 2013. From the blade scale to the reach scale: A characterization of aquatic vegetative drag. *Advances in Water Resources* 51, pp. 305-316.
- Luhar, M. and Nepf, H.M., 2016. Wave-induced dynamics of flexible blades. *Journal of Fluids and Structures*, 61, pp. 20–41.
- Luhar, M., Rominger, J. and Nepf, H.M., 2008. Interaction between flow, transport and vegetation spatial structure. *Environmental Fluid Mechanics* 8.5-6, pp. 423-439.
- Luhar, M., Coutu, S., Infantes, E., Fox, S., Nepf, H., 2010. Wave-induced velocities inside a model seagrass bed 115, pp. 1–15.
- Luhar, M., Infantes, E., Orfila, A., Terrados, J., Nepf, H.M., 2013. Field observations of wave-induced streaming through a submerged seagrass (*Posidonia oceanica*) meadow. *Journal of Geophysical Research* 118, pp. 1955-1968.
- Ma, G., Kirby, J.T., Su, S.F., Figlus, J., Shi, F., 2013. Numerical study of turbulence and wave damping induced by vegetation canopies. *Coastal Engineering*, 80, pp.68–78.
- Manca, E., Cáceres, I., Alsina, J.M., Stratigaki, V., Townend, I., Amos, C.L., 2012. Wave energy and wave-induced flow reduction by full-scale model *Posidonia oceanica* seagrass. *Continental Shelf Research* 50-51, pp. 100–116.
- McClellan, J., & Sumner, D., 2014. An experimental investigation of aspect ratio and incidence angle effects for the flow around surface-mounted finite-height square prisms. *Journal of Fluids Engineering, Transactions of the ASME*, 136(8).
- Mendez, F.J. and Losada, I.J., 2004. An empirical model to estimate the propagation of random breaking and nonbreaking waves over vegetation fields. *Coastal Engineering* 51, pp.103–118.
- Möller, I., Spencer, T., French, J.R., Leggett, D.J., Dixon, M., 1999. Wave Transformation Over Salt Marshes: A Field and Numerical Modelling Study from North Norfolk, England, *Estuarine, Coastal and Shelf Science*, 49(3), pp 411-426.

- Morison, J.R., O'Brien, M.P., Johnson, J.W. and Schaaf, S.A., 1950. The forces exerted by surface waves on piles. *J. Petrol. Technol., Petroleum Transactions, AIME, (American Inst. Mining Engrs.)*189, pp.149-154.
- Munson, B., Okiishi, T., Huebsch, W., Rothmayer, A., 2013. *Fundamentals of fluid mechanics*, seventh edition.
- Naghypour, M., 2001. Large scale experiments data analysis for estimation of hydrodynamic force coefficients part 1 : time domain analysis. *International Journal of Engineering*, 14(4), pp.323–332.
- Nath, J.H., 1978. *Drift Speed of Buoys in Waves*, with Appendix by M. S. Longuet-Higgins. *Coastal Engineering*. Pp 859-877
- Nakamura, M., Koterayama, W., Hoshino, K., 1991. Three dimensional effects on hydrodynamic forces acting on an oscillating finite-length circular cylinder. In: *Proceedings of the First International Offshore and Polar Engineering Conference*, UK, 11–16 August, 1991.
- Nepf, H. M.,1999. Drag, turbulence, and diffusion in flow through emergent vegetation. *Water Resources Research*, 35(2), pp. 479-489.
- Nepf, H.M., 2011. Flow over and through biota. In: Wolanski, E., McLusky, D. (Eds.), *Treatise on Estuarine and Coastal Science*. Academic Press, Waltham, pp. 267–288.
- Nepf, H.M., 2012. Flow and Transport in Regions with Aquatic Vegetation. *The Annual Review of Fluid Mechanics* 44(1), pp. 123-142.
- Nepf, H.M., Mugnier, C.G. & Zavistoski, R.A., 1997. The Effects of Vegetation on Longitudinal Dispersion. pp.675–684.
- Nepf, H.M. and Vivoni, E.R., 2000. Flow structure in depth-limited, vegetated flow. *Journal of Geophysical Research: Oceans*, 105(C12), 28547-28557.
- Nikora, N., Nikora, V., 2007. A viscous drag concept for flow resistance in vegetated channels. *Proceedings of the 32nd IAHR Congress*, Venice, 1–6 July.
- Okajima, A., Matsumoto, T., Kimura, S., 1998. Force measurements and flow visualization of bluff bodies in oscillatory flow. *Journal of Wind Engineering and Industrial Aerodynamics* 34, pp. 213-228.
- Peterson, C. H., Summerson, H. C. ,Duncan, P. B. , 1984. The influence of seagrass cover on population structure and individual growth rate of a suspension-feeding bivalve, *Mercenaria mercenaria*, *Journal of Marine Research*, 42(1), pp 123-138.
- Phillips, O., 1977. *The dynamics of the upper ocean*. Cambridge University Press.
- Pujol, D., Serra, T., Colomer, J., Casamitjana, X., 2013. Flow structure in canopy models dominated by progressive waves. *Journal of Hydrology* 486, pp. 281-292.
- Sarpkaya, T., Isaacson, M., 1981. *"Mechanics of wave forces on offshore structure"*. Van Nostrand Reinhold Company, New York.
- Seymour, R.J., 1996. Discussion of "Effects of southern California kelp beds on waves", Elwany, H.S., O'Reilly, W.C., Guza, R.T., Flick, R.E.. *J. Waterw. Port Coast. Ocean Eng.* 122 (4), pp. 207 – 208.
- Shi, B.W., Yang, S.L., Wang, Y.P., Bouma, T.J., Zhu, Q., 2012. Geomorphology Relating accretion and erosion at an exposed tidal wetland to the bottom shear stress of combined current – wave action. *Geomorphology*, 138(1), pp.380–389.
- Sorensen, R.M., 2006. *Basic Coastal Engineering*. Springer. Third edition.
- Stevens, C.L., Hurd, C.L. and Smith, M.J., 2001. Water motion relative to subtidal kelp fronds. , 46(3), pp.668–678.

- Stewart, H.L., 2006. Morphological variation and phenotypic plasticity of buoyancy in the macroalga *Turbinaria ornata* across a barrier reef. , pp.721–730.
- Stewart, H.L., 2004. Hydrodynamic consequences of maintaining an upright posture by different magnitudes of stiffness and buoyancy in the tropical alga *Turbinaria ornata*. , 49, pp.157–167.
- Stive, M.J.F., Wind, H.G., 1986. Cross-shore mean flow in the surf zone. , 10, pp.325–340. *Coastal Engineering*. 10, pp 325-340.
- Sumer, B.M. and Fredsoe, J., 2006. *Hydrodynamics around cylindrical structures*. World Scientific.
- Suzuki, T., and Arikawa, T., 2011. Numerical analysis of bulk drag coefficient in dense vegetation by immersed boundary method. *Coastal Engineering Proceedings*, 1(32), waves.48.
- Svendsen, I.A., 2006. *Introduction to Nearshore Hydrodynamics*. World Scientific.
- Tørum, A. and Gudmestad, O.T., 2012. *Water Wave Kinematics*. Volume 178 of *Nato Science Series E*. Springer Science & Business Media
- Uittenbogaard, R. 2006. Dynamic model of vegetation motions; derivations and solution procedure. Memorandum, Delft Hydraulics.
- Vengatesan, V., Varyani, K.S. & Barltrop, N., 2000. An experimental investigation of hydrodynamic coefficients for a vertical truncated rectangular cylinder due to regular and random waves. , 27, pp.291–313.
- Venugopal, V., Varyani, K.S., Baltrop, N.D.P., 2005. Wave force coefficients for horizontally submerged rectangular cylinders. *Ocean Engineering* 33, pp.1669–1704
- Venugopal, V., Varyani, K.S., Westlake, P.C., 2008. Drag and inertia coefficients for horizontally submerged rectangular cylinders in waves and currents. , 223, pp.121–136.
- Vogel, S., 1994. In: *Life in Moving Fluids*, 2nd ed. Princeton University. Press, Princeton, NJ.
- Waseda, T., Yoshiaki, T., Marshall, P.T., 2001. Adjustment of Wind Waves to Sudden Changes of Wind Speed. *Journal of Oceanography*, 57, pp. 519-533.
- White, F.M., 2008. *Fluid Mechanics*, volume 6. McGraw-Hill International.
- Williamson, C.H.K., 1984. Sinusoidal flow relative to circular cylinders. *Journal of Fluid Mechanics* 155, pp. 141-174.
- Zedler JB, Callaway JC, Sullivan G., 2001. Declining biodiversity: Why species matter and how their functions might be restored in California tidal marshes. *BioScience* 51 pp 1005–1017.
- Zeller, R.B. et al., 2014. Improved parameterization of seagrass blade dynamics and wave attenuation based on numerical and laboratory experiments. , 59(1), pp.251–266.
- Zukauskas, A., 1987. Heat transfer from tubes in cross-flow. *Advances in Heat Transfer* 18, pp. 87–159.

Appendix A. Additional validation for submerged rigid cylinders

Validation of the motion

An additional verification was done in order to assess if the forces had been correctly implemented in Dynveg. A stem was exposed to uniform loads along its height (Figure 1-A) and the modelled displacement of the tip was compared with the maximum deflection at the free end of a cantilever beam, δ_{max} . The theoretical magnitude of the movement was calculated from the integration of the basic differential equation of the deflection curve of a beam:

$$\delta_{max} = \frac{ql^4}{8EI} \quad (A.1)$$

Where q is the intensity of the load, l is the length of the beam and EI is its flexural rigidity.

The application of equation A.1. is restricted by the assumptions of linearly elastic material, originally straight shape and small angles of rotation, curvatures and deflections (Gere and Goodno, 2009). In order to ensure that the requirements were met, the most rigid mimic (i.e., mimic 4, section 1) was modelled and small loads were exerted to the plant.

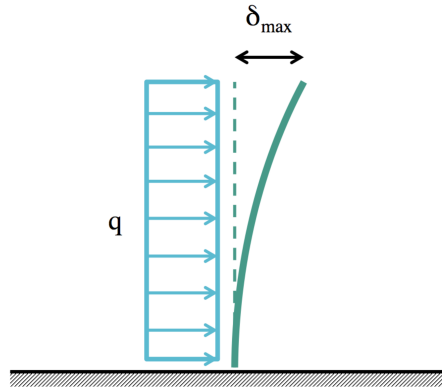


Figure 1-A. Ideal scenario for the validation of the inertia and drag forces.

Two situations were considered:

- Only drag forces act on the stem. The added mass coefficient was set to zero and the velocity was constant in time and space so that the Froude-Krylov force was equal to zero. Three cases were tested ($u(z, t) = 0.001, 0.002, 0.003$ m/s) in which the distributed load q was given by:

$$q = f_d = \frac{1}{2} c_D \rho_w w u^2 \quad (A.2)$$

Where u is the flow velocity, c_D is the drag coefficient, ρ_w is the density of the fluid and w is the width of the mimic.

- Only inertia forces act on the stem. The drag coefficient was set to zero and the magnitude of the depth-uniform velocity profiles was increased at a constant rate every timestep. Three values of acceleration were modelled ($\partial u / \partial t (z, t) = 0.01 - 0.02 - 0.03$ m/s²). The distributed force resulted equal to:

$$q = f_i = c_M \rho_w A \frac{du}{dt} \quad (A.3)$$

Where c_M is the inertia coefficient, ρ_w is the fluid density, A is the cross-sectional area of the stem and $\partial u / \partial t$ is the flow acceleration.

The density of the plants was set equal to that of the water to eliminate the buoyancy. The sudden application of the load in the first timestep resulted in free vibrations of the stem, which ceased after some time as shown in Figure 2-A.

The same values of force coefficients were used in all the scenarios ($c_D = 1.8$ and $c_M = 3.2$). The comparison between the static deflection of the plant from Dynveg (when the dynamic effects were dampened) and the theoretical value from equation A.1. is shown in Table 1-A.

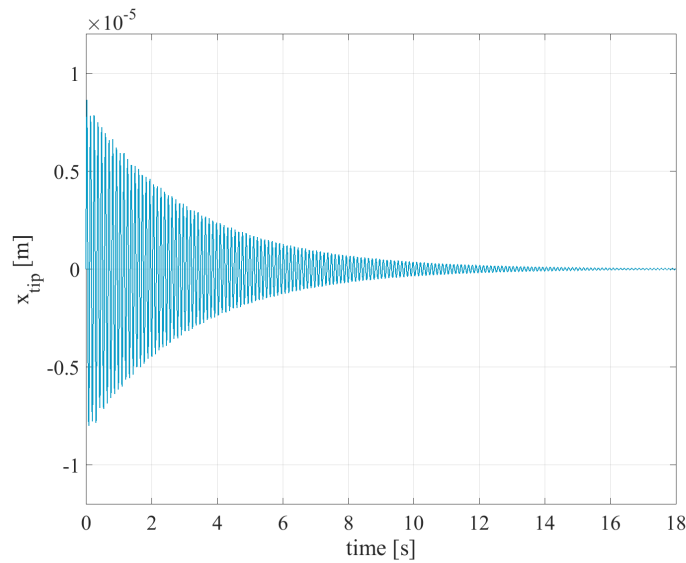


Figure 2-A. Deflection of the tip of the stem modelled over time for the case of $c_a = 0$, $u(z) = 0.001$ m/s and $\frac{\partial u}{\partial t}(z) = 0$ m/s² (only drag forces act on the stem).

Table 1-A. Comparison between maximum deflections modelled with Dynveg ($\delta_{max,Dyn}$) and the theoretical expression for a cantilever beam ($\delta_{max,eq}$).

$du/dt(z)$	$u(z)$	f_i	f_d	$\delta_{max,eq}$	$\delta_{max,Dyn}$	$\delta_{max,eq}/\delta_{max,Dyn}$
m/s	m/s	N/m	N/m	m	m	-
0.01	-	0.0010	0	4.36E-06	4.30E-06	1.3842%
0.02	-	0.0020	0	8.72E-06	8.60E-06	1.3841%
0.03	-	0.0031	0	1.31E-05	1.29E-05	1.3843%
0	0.001	0	6.64E-06	2.83E-08	2.79E-08	1.3833%
0	0.002	0	2.66E-05	1.13E-07	1.12E-07	1.3843%
0	0.003	0	5.98E-05	2.55E-07	2.51E-07	1.3841%

The predicted deflection is very similar in both cases and only differs at the third significant digit. It is concluded that both the inertia and the drag force are correctly implemented in the model.

Validation of the forces

The computation of the base forces by Dynveg was also verified contrasting the results obtained using three different procedures:

- (1) Calculating the velocities for a certain wave condition using linear wave theory in Matlab, introducing the velocities in Dynveg via input files, doing appropriate temporal and spatial interpolation and finally determining the forces of the stem within the model.
- (2) Directly calculating the flow velocities for a certain wave condition at the grid points for the timesteps of the simulation (inside the Fortran code: avoiding the use of input files and the interpolation of velocities in time and/or space) and calculating the loads exerted on the stem with Dynveg.
- (3) Calculating the velocities using linear wave theory and determining the base force applying the Morison equation (assuming negligible plant motion). In order to ensure that the relative velocity was equal to the flow velocity the properties of mimic 4 (defined in Table 1, section 1) were used in the set-ups. The same force

coefficients were implemented in the three approaches ($c_D = 1.9$ and $c_M = 3.1$). The flexural rigidity of the stem was increased with a factor of 10 to guarantee that the motion of the plant was insignificant.

The aim of step 1 was to check the performance of the interpolation subroutines, which were be further used in the non-linear fitting of the force coefficients for the cases of flexible vegetation (Appendix E). The comparison of the theoretical and computed base force (derived from the curvature of the stem, in accordance to equation 1.15) is shown below for an inertia dominated case, with $H = 0.01\text{ m}$ and $T = 1\text{ s}$ (Figure 3-A) and for a drag dominated case, with $H = 0.2\text{ m}$ and $T = 3.5\text{ s}$ (Figure 4-A).

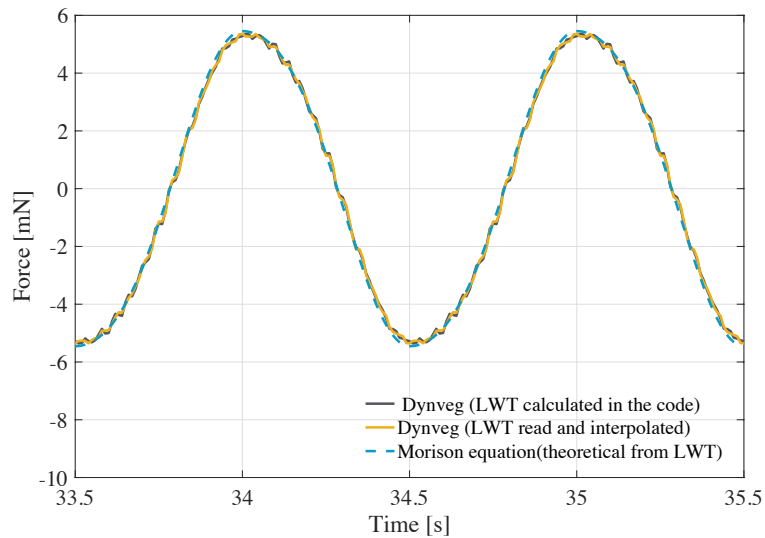


Figure 3-A. Comparison of the horizontal forces at the base for mimic 4 with $h_v = 0.30\text{ m}$, $H = 0.02\text{ m}$ and $T = 1\text{ s}$.

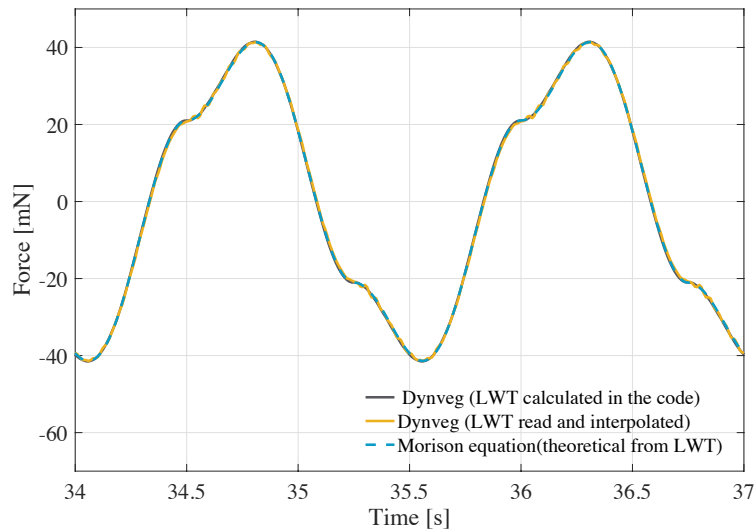


Figure 4-A. Comparison of the horizontal forces at the base for mimic 4 with $h_v = 0.30\text{ m}$, $H = 0.20\text{ m}$ and $T = 3.5\text{ s}$.

As it can be observed in the figures, the force time series from the three procedures coincide in one single line and the performance of the model is considered satisfactory.

Appendix B. Analysis of acceleration for rigid cylinders

Analysis of the noise in the computed forces for the inertia dominated cases

The time-series of the computed forces displayed strong fluctuations for the wave conditions with the smallest wave height ($H = 0.04$ m) and the shortest wave periods ($T = 1$ s and $T = 2$ s), which were not present in the measurements (Figure 1-B). Such cases were associated to large accelerations and a higher relative importance of the inertia forces. The oscillations were absent in drag-dominated cases, where the predictions of the model reproduced with high accuracy the results from the experiment. Consequently, the implementation of the acceleration in Dynveg was identified as a possible source of noise. In order to confirm such hypothesis, the Froude-Krylov force was set to zero in the model. The result of the run is shown in Figure 2-B.

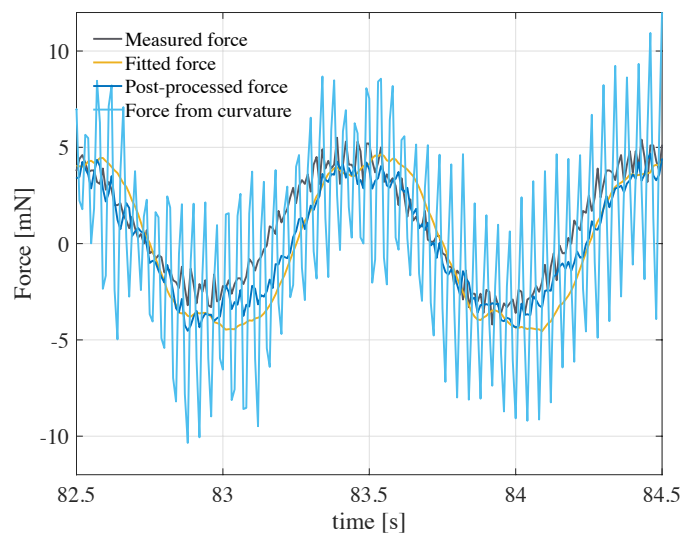


Figure 1-B. Comparison of the computed and measured horizontal forces at the base for $h_v = 15$ cm, $H = 0.04$ m, $T = 1$ s. The input velocities were obtained combining measurements of different set-ups.

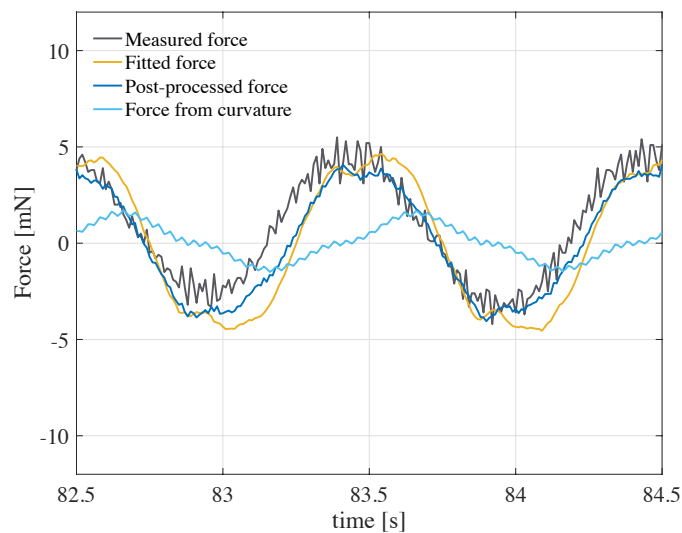


Figure 2-B. Comparison of the computed and measured horizontal forces at the base for $h_v = 15$ cm, $H = 0.04$ m, $T = 1$ s. The Froude-Krylov force was set equal to zero in the model.

As it can be observed, the force derived from the curvature at the base is 90° out of phase with the measurements and has a lower magnitude, since it only includes the effect of the drag. Nevertheless, it did not display the large oscillations that had been modelled previously. The post-processed force was determined using equation (2.12) with the measured velocities, the plant motion computed in Dynveg and the fitted force coefficients derived in Section 5. Even though the stem dynamics were not accurately reproduced in the model, the magnitude of the stem motion is so small compared to the flow properties that the result was still very similar to the measurements.

Such tests seemed to confirm that the cause of the fluctuations resided in the acceleration. Figure 3-B shows the time-series of the acceleration for $H = 0.04$ m and $T = 1$ s, calculated from the measurements using central differences.

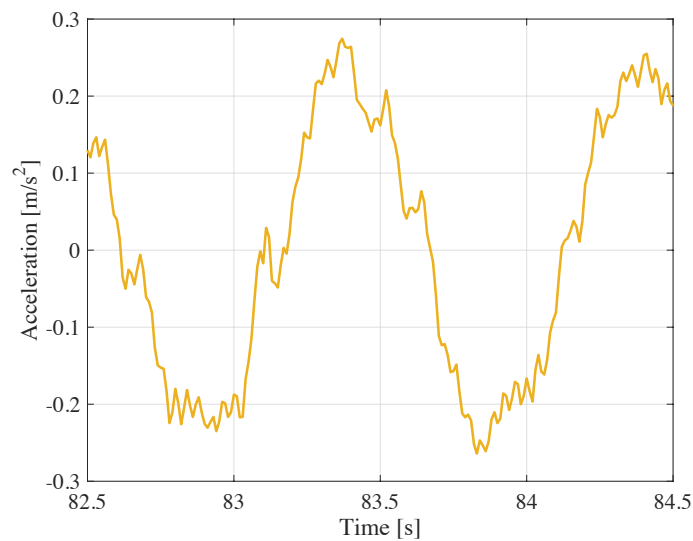


Figure 3-B. Time series of the acceleration obtained by central differences from the recorded velocities for mimic 4 with $h_v = 15$ cm, $H = 0.04$ m, $T = 1$ s, and $z = m$

Two possible causes were suggested to cause discontinuities in the acceleration:

- The velocity profiles were built combining data from different experiments. An example of an ensembled velocity profile is represented in Figure 4-B. The shape of the curve is not smooth and it displays considerable variations along the depth, which could produce jumps in the distributed forces along the plant, induce vibrations and result in deviations from the conditions of the experiments.

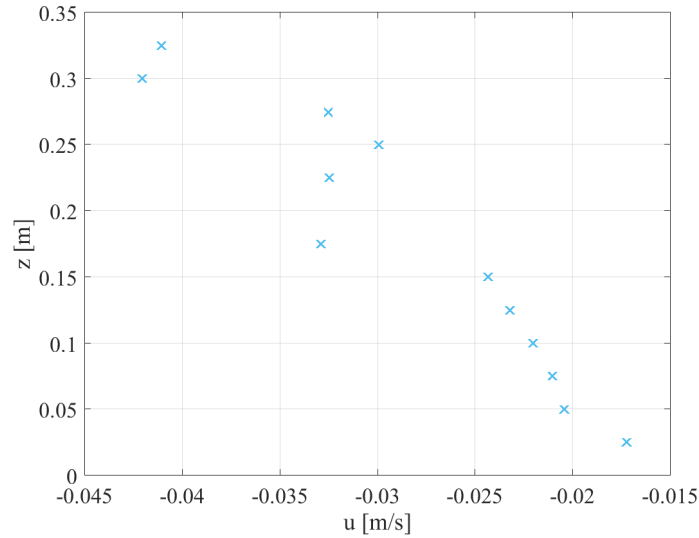


Figure 4-B. Instantaneous velocity profile obtained combining measurements from various experiments at different elevations for mimic 4 with $h_v = 15$ cm, $H = 0.04$ m, $T = 1$ s.

- Another possible source of noise may be directly associated to the numerical differentiation of experimental data, which is very sensitive to errors yielded by the measurements.

Separate checks were done in order to evaluate the effect of both factors.

Depth-uniformity of the velocity profiles

In the present check, instead of combining information obtained in different set-ups to derive a complete vertical profile, hyperbolic functions were fit to the velocities measured by the EMF (at a single height) for every timestep. The flow properties at the remaining elevations were calculated using such fit, according to:

$$u(z, t) = A(t) \cdot \cosh(kz) \quad (\text{B.1})$$

$$w(z, t) = B(t) \cdot \sinh(kz) \quad (\text{B.2})$$

Where k is the wave number, z is the height with respect to the bottom and $A(t)$ and $B(t)$ are the fitting coefficients. The velocities were defined in Dynveg at the same heights (from $z = 2.5$ cm to $z = 32.5$ cm at intervals of $\Delta z = 2.5$ cm) and timesteps ($\Delta t = 0.01$ s) than the experiments. An instantaneous profile is shown in Figure 4-B.

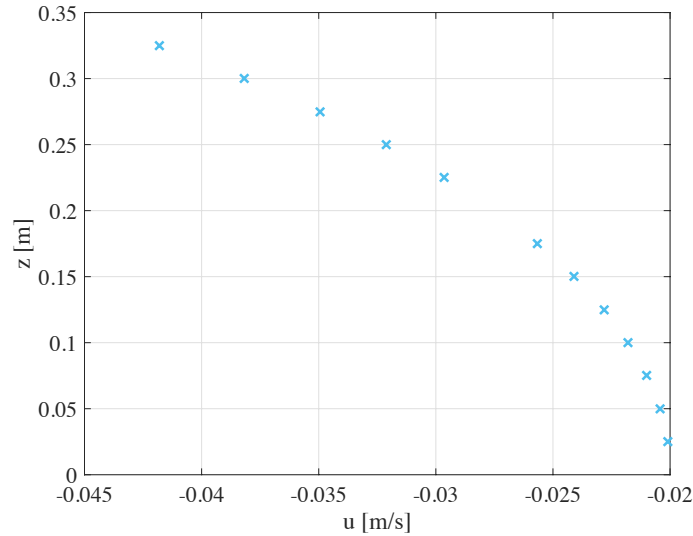


Figure 4-B. Velocity profile obtained fitting hyperbolic functions to the measurements of the EMF.

The accelerations were calculated through numerical differentiation inside the code. The modelled horizontal base forces are shown in Figure 5-B.

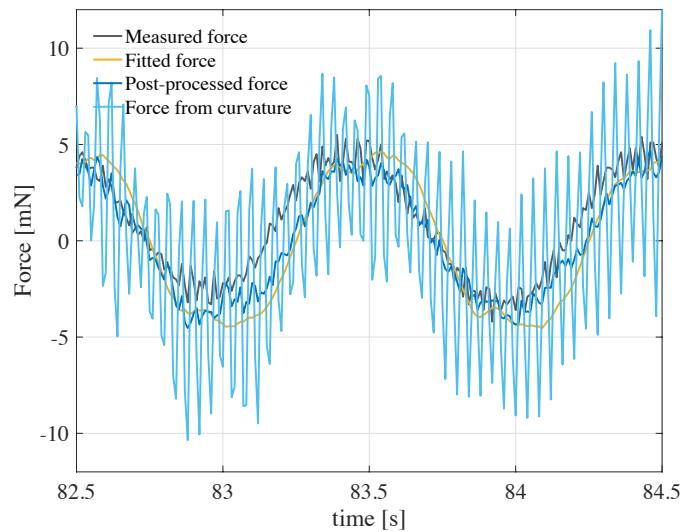


Figure 5-B. Comparison of the computed and measured horizontal forces at the base for $h_v = 15$ cm, $H = 0.04$ m, $T = 1$ s. The input velocities were calculated fitting hyperbolic functions to the measurements of the EMF.

The use of continuous velocity profiles did not improve the quality of the predictions neither it smoothed the acceleration. Moreover, by deriving the velocities from one single measurement any error or fluctuation at those points would be propagated all over the water column.

Time-differentiation of the velocity

Continuous velocity time-series were generated to evaluate if the fluctuations were produced by Dynveg or were associated to the processing of experimental data. Linear wave theory was used to reproduce the flow velocities since the small waves of the inertia dominated cases were within its range of applicability. The results of the model are represented in Figure 6-B.

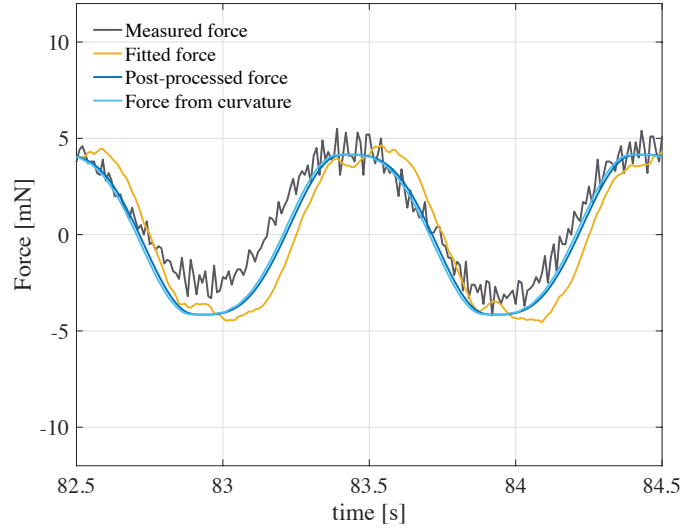


Figure 6-B .Comparison of the computed and measured horizontal forces at the base for $h_v = 15$ cm, $H = 0.04$ m, $T = 1$ s. The input velocities were calculated using linear wave theory.

Using smooth velocity and acceleration time-series seemed to eliminate the noise of the computed signal. Therefore, a low-pass filter function was applied to the acceleration derived from the measurements before calculating the inertia forces in Dynveg. The filter operation was done using a rational transfer function of the form (Oppenheim et al., 1999):

$$H(z) = \frac{b(1) + b(2)z^{-1}}{a(1)} \quad (\text{A.3})$$

Where the denominator coefficient $a(1)$ was defined as:

$$a(1) = \frac{\Delta t}{\tau} \quad (\text{A.4})$$

Here Δt is the timestep and τ is the relaxation time, which was set to 0.06 s. The numerator coefficients were defined as $b(1) = 1$ and $b(2) = 1 - a(1)$. The time-series of the acceleration after the filtering procedure is shown in Figure 7-B.

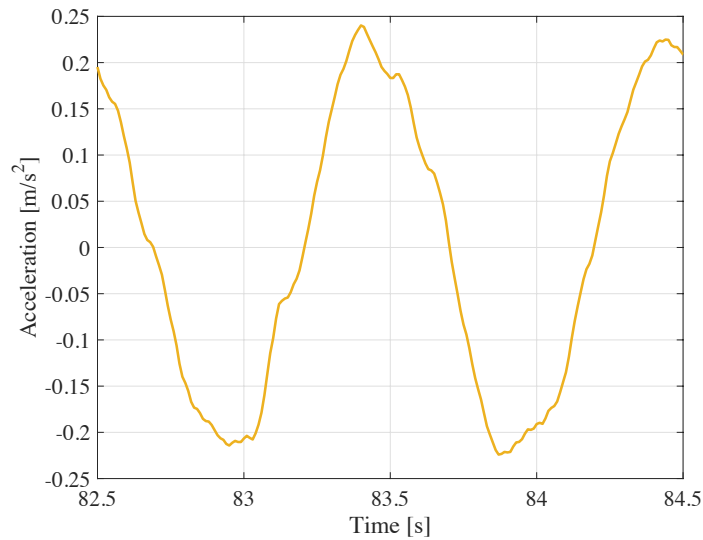


Figure 7-B. Time series of the acceleration obtained by central differences from the recorded velocities and low-pass filtering for mimic 4 with $h_v = 15$ cm, $H = 0.04$ m, $T = 1$ s.

As it is shown in Figure 8-B, by filtering the signal the amplitude of the oscillations was reduced until it coincided with that of the measurements, and the model reproduced the results of the experiment with considerable accuracy.

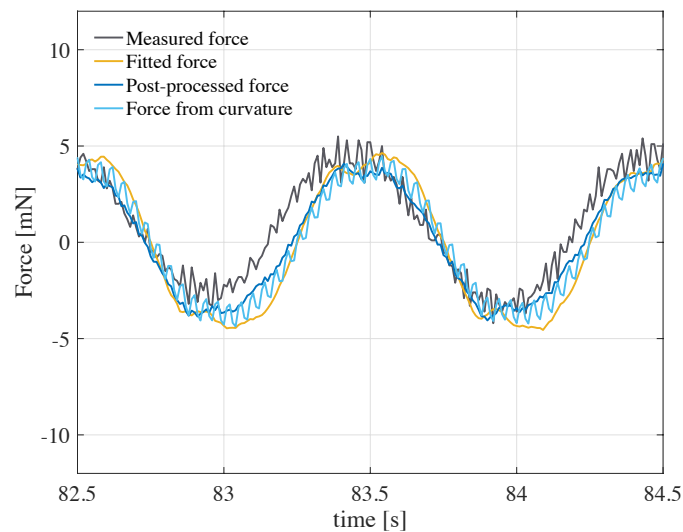


Figure 8-B. Comparison of the computed and measured horizontal forces at the base for $h_v = 15$ cm, $H = 0.04$ m, $T = 1$ s. The input velocities were obtained combining measurements from different set-ups. A low pass-filter function was used to reduce the noise in the acceleration.

Appendix C. Model parameters

Effect of the timestep

The effect of the timestep, Δt , on the computed base force was analyzed by running the same wave condition in Dynveg using different values of Δt . The results are shown Figure 1-C.

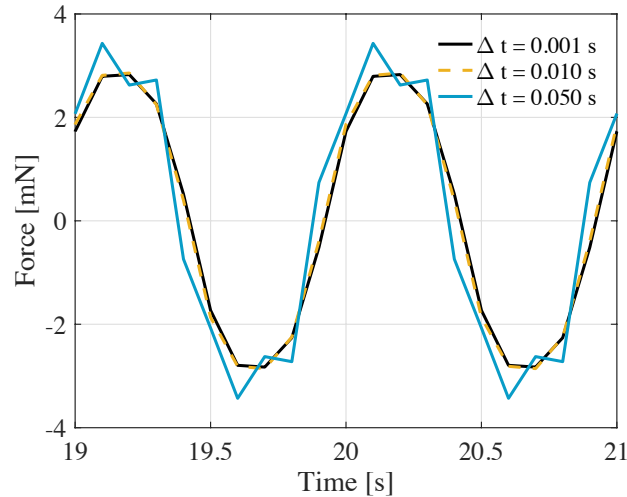


Figure 1-C. Comparison of the computed forces at the base, F_x , over time for different values of the timestep Δt , with Mimic 4, with $h_v = 15$ cm, $H = 0.04$ m and $T = 1$ s.

The computed time-series coincided for $\Delta t = 0.001$ s and $\Delta t = 0.01$. Consequently, it was concluded that the second value allowed to reduce the duration of the simulations without leading to errors. The predictions showed significant differences when a value of $\Delta t = 0.05$ s was used, and this timestep was considered too large for the present conditions.

Effect of the theta-method

The numerical method used to solve the integro-differential equation was defined by the parameter θ , with $0 \leq \theta \leq 1$, where $\theta = 0$ corresponded to the explicit method and $\theta = 1$ to the implicit method. As it can be observed in Figure 2-C, variations of the value of θ did not alter the results of the simulations.

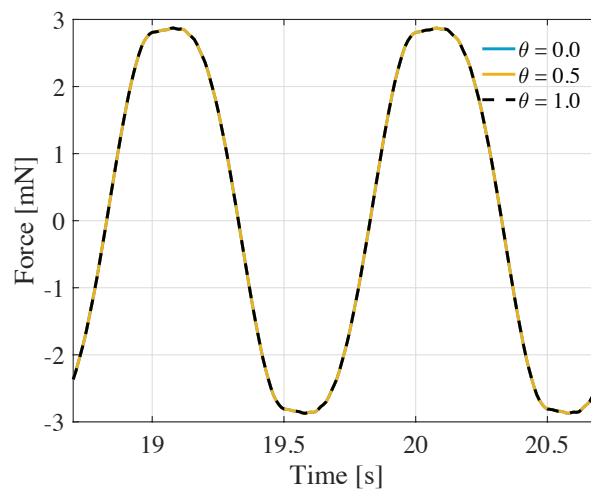


Figure 2-C. Comparison of the computed forces at the base, F_x , over time for different values of the timestep Δt , with Mimic 4, with $h_v = 15$ cm, $H = 0.04$ m and $T = 1$ s.

Appendix D. Hysteresis effects

Initial phase of the velocity

The effect of the initial phase of the velocity on the stem motion was analyzed by running the same wave condition using linear wave theory with $x_v = 0$, changing the value of φ in equation (2.19) and equation (2.20) from $\varphi = 0^\circ$ until $\varphi = 180^\circ$ at intervals of 45° . The computed tip motion is shown for two different wave conditions in Figure 1-D and Figure 2-D.

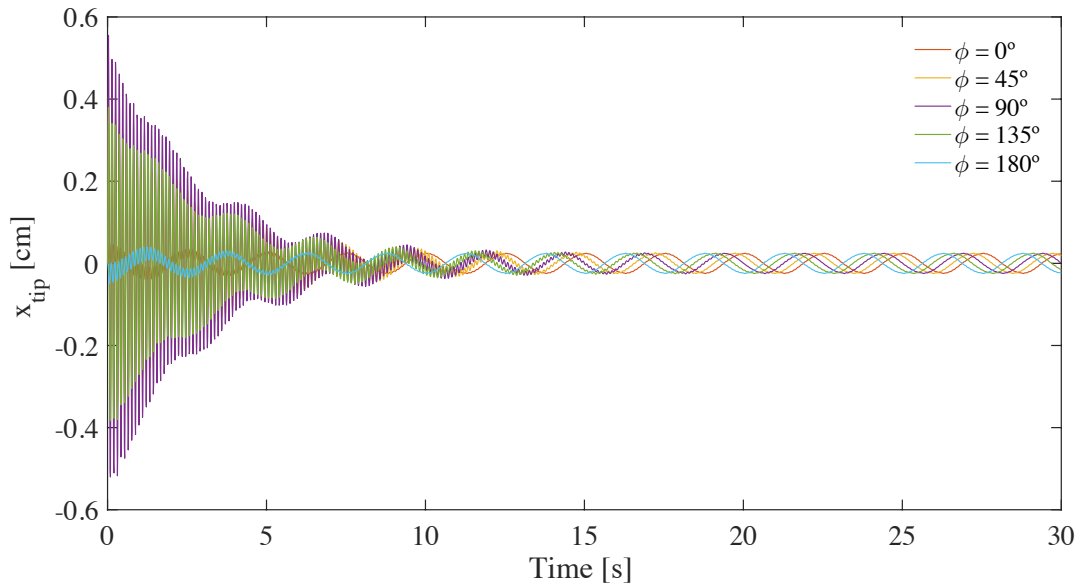


Figure 1-D. Comparison of the position of the tip, x , over time for Mimic 2, with $h_v = 30$ cm, $H = 10$ cm and $T = 2.5$ s.

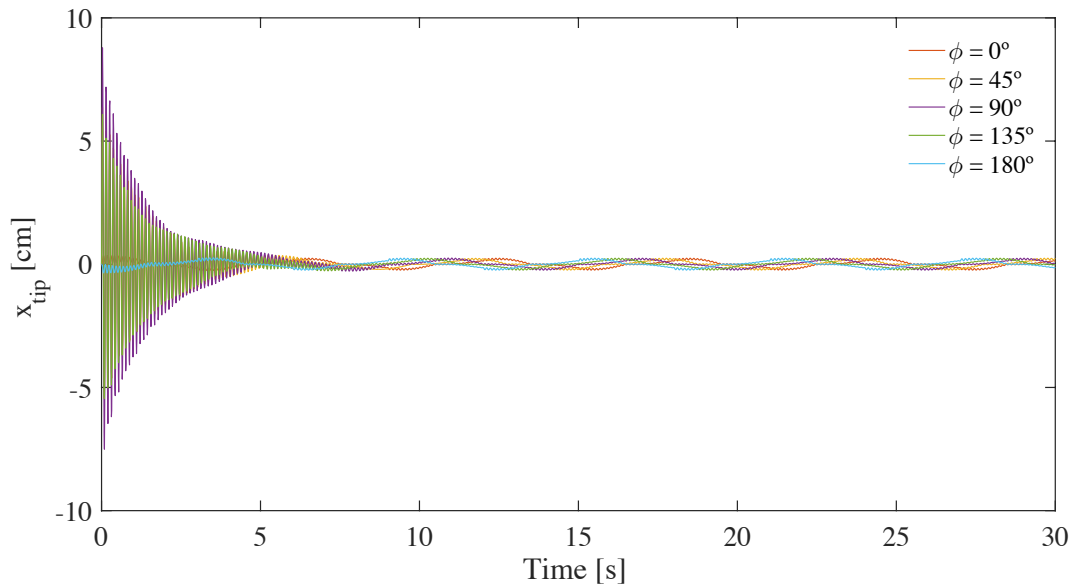


Figure 2-D. Comparison of the position of the tip, x , over time for Mimic 2, with $h_v = 30$ cm, $H = 15$ cm and $T = 6$ s.

The behaviour of the stem changed for the different cases at the beginning of the simulations. Nevertheless, once the initial oscillations were dampened, the solutions converged into the same steady state. It was concluded that hysteresis effects did not affect the results of the model.

Appendix E. Validation of Dynveg for flexible vegetation

Non-linear fitting of force coefficients for flexible mimics

The procedure to obtain the force coefficients for flexible vegetation was applied for Mimic 3 with $h_v = 0.3 \text{ m}$ and with a wave condition of $H = 0.16 \text{ m}$ and $T = 3.5 \text{ s}$ as a proof of concept. Dynveg was ran using the velocities recorded in the experiments by Bakker (2015). The complete vertical profile was constructed using data from different set-ups, as indicated in Section 5. The velocities were differentiated to derive the accelerations and a low pass filter function was applied to smooth the time series. The force coefficients were varied in the simulations within the ranges of $c_D = 1 - 4$ and $c_a = 1 - 4$. The results of the model were compared with the experiment *3L30H160T35EMF300_take1*. The laboratory records had been processed by Döbken (2015), producing a structure file which contained the measured velocities, base force and tip position during two wave periods. The comparison with the experiments was based on the horizontal position of the tip, $x_{tip}(t)$, and the horizontal force at the base, $F_x(t)$.

After performing the simulations, the velocities that had been introduced as an input in Dynveg were correlated with the time-series of the structure file. This was done to ensure that the computations corresponded to the same phase of the wave than the measurements. The modelled forces and positions were also shifted using the same offset. When the computed and recorded time-series were plotted, the forces were in phase with the experiments for all the combinations of c_D and c_a , as shown in Figure 1-E. Nevertheless there was an offset in the horizontal displacement of the tip which varied between $\Delta t_s = 2.57 - 2.77 \text{ s}$ for the different values of c_D and c_a , as illustrated in Figure 2-E (a).

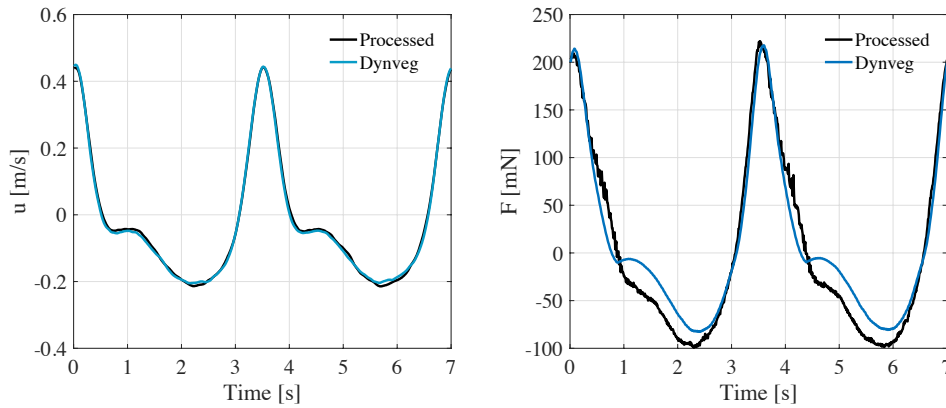


Figure 1-E. Comparison of results for $c_D = 2$ and $c_a = 1$. (a) Inputted and measured velocity time-series after correlation (b) Computed and measured forces after shifting using the offset obtain from (a).

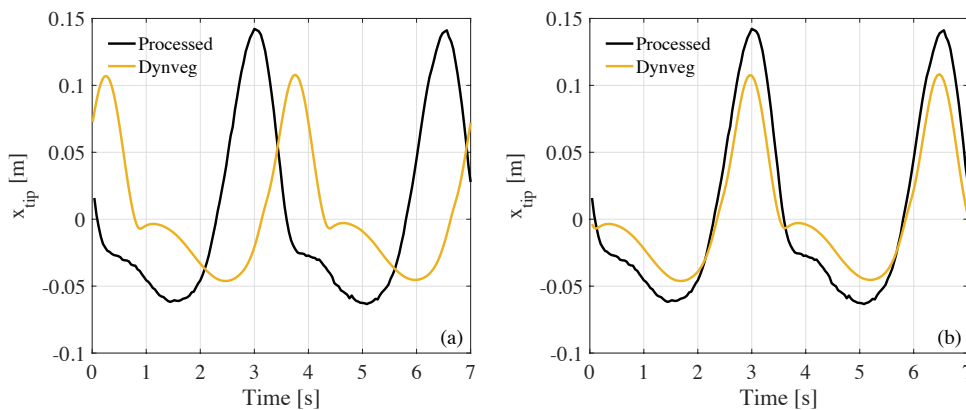


Figure 2-E. Comparison of results for $c_D = 2$ and $c_a = 1$ (a) Computed and recorded tip position after correlating the velocities. (b) Horizontal measured and computed tip positions after correcting for the phase shift of (a).

Such timeshift could have several causes. For instance, it could be associated to the processing of the experimental data. In order to synchronize the measurements of the force transducer and the camera, a LED light was shifted on. The flash was recorded by both the camera and the data-acquisition software (Bakker, 2015), and its duration was approximately equal to the found offset. Therefore, the shift could be caused by referencing the forces to the moment when the LED was shifted on and the stem position to the instant in which the light was turned off. Nevertheless, the causes of the delay have not been further investigated in the present work.

In order to compare the amplitude of the modelled and measured time signals, the calculated tip position was correlated to the record to correct for the phase difference, as shown in in Figure 2-E (b). The root mean square error of both variables (F_x and x_{tip}) was calculated according to equation (E.1) and equation (E.2).

$$\varepsilon_x = \frac{1}{N} \sqrt{\sum_{t_0}^{t_f} (x_{tip,m} - x_{tip,D})^2} \quad (E.1)$$

$$\varepsilon_F = \frac{1}{N} \sqrt{\sum_{t_0}^{t_f} (F_{x,m} - F_{x,D})^2} \quad (E.2)$$

Where ε_x and ε_F are the errors in the positions and the forces, respectively. The subscript m refers to measured values and D to the results of Dynveg and N is the number of data points in the time interval considered, from $t = t_0$ until $t = t_f$. The comparison for the different values of c_D and c_M is represented in Figure 3-E.

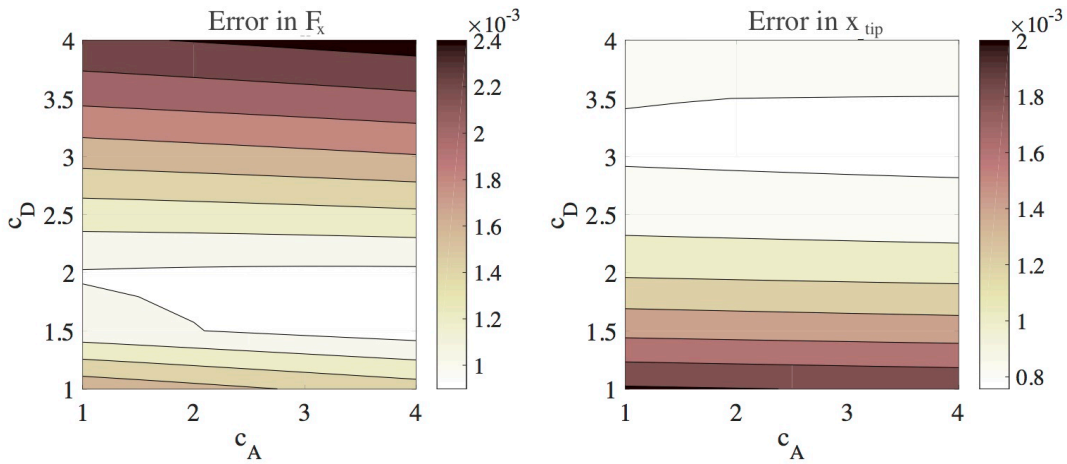


Figure 3-E. Root mean square error in the prediction of the horizontal force at the base (left) and in the horizontal tip displacement (right)

Both the base forces and the tip motion were more sensitive to changes in the drag coefficient and considerably less influenced by modifications of the added mass coefficient, which is coherent with the fact that the case was drag-dominated. The error in the base load was minimized for a value of approximately equal to $c_D \approx 2$. The horizontal excursion of the tip was more accurately predicted for values of the drag coefficient ranging between $c_D = 3$ and $c_D = 3.5$. The pair of force coefficients that minimized both errors in the forces and plant motion were $c_D = 2.5$ and $c_a = 2.5$. The corresponding results are shown in Figure 4-E.

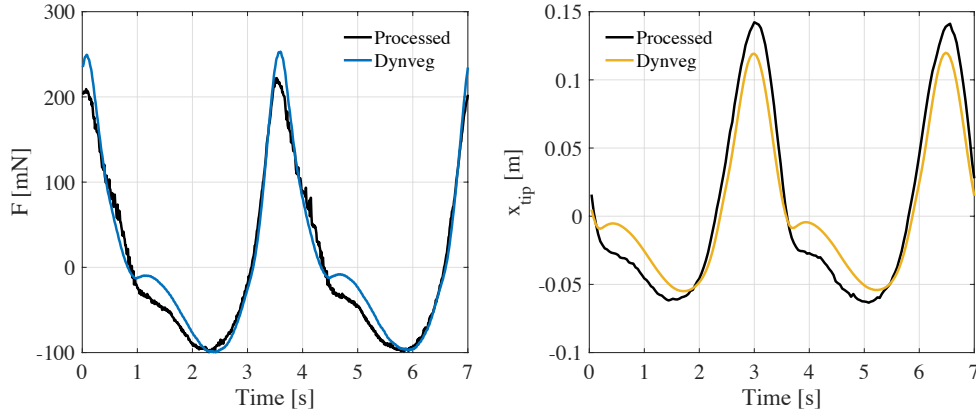


Figure 4-E. Comparison of results for $c_D = 2.5$ and $c_a = 2.5$.

It can be observed that there are some deviations in the predictions, particularly at the peaks and at the transition from positive to negative velocities. The differences can be attributed to different factors. The force coefficients were kept constant in the runs regardless of the value of the Keulegan-Carpenter number. It was already shown Section 5 that Dynveg provided accurate predictions of the fitted forces (i.e., the forces calculated from the measurements and constant values of c_D and c_M using the Morison formulation) but could not exactly reproduce the recorded time-series, since in order to emulate those it would be necessary to incorporate the influence of the flow properties on the coefficients. There may be additional sources of error associated to the measuring devices and the processing of the experimental data. Moreover, there is also uncertainty in relation to the properties of the mimic. The manufacturer of Mimic 3 provided a possible range of values for the elastic modulus, with $E = 1.1 - 2.9 \cdot 10^9 \text{ N/m}^2$. Bakker (2015) measured its value in the laboratory, attaching a weight, P , at the end of the stem and using the measured deflection, δ_{max} , to calculate E from equation (E.3)

$$\delta_{max} = \frac{Pl^3}{3EI} \quad (\text{E.3})$$

Here l is the length of the stem and I is the second moment of area. He obtained an intermediate value of $E = 2.2 \cdot 10^9 \text{ N/m}^2$, which was used in the previous runs. In order to evaluate the influence of variations of E , two additional simulations were performed using the extremes values of the interval given by the manufacturer. The results of the model are compared with the measurements in Figure 5-E.

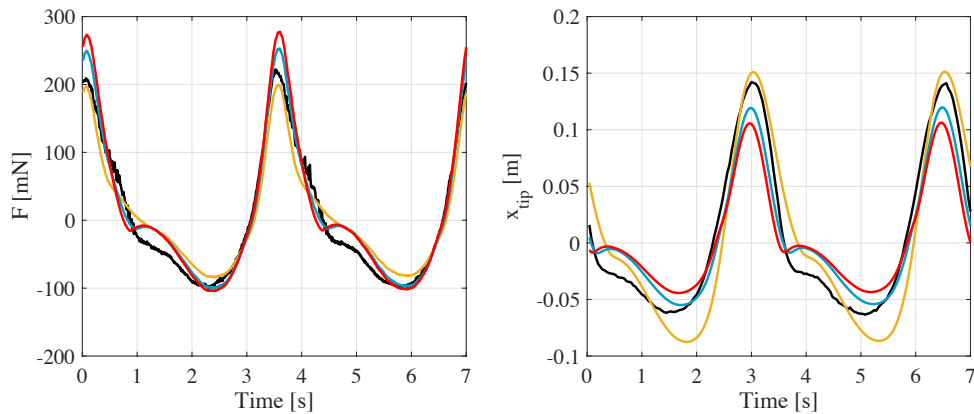


Figure 5-E. Effect of the stiffness on the computed base forces (left) and tip motion (right). The measurements are represented by a black line (—). The results of the largest elastic modulus $E = 2.9 \cdot 10^9 \text{ N/m}^2$ is shown with a red line (—). The results obtained with the intermediate elastic modulus $E = 2.2 \cdot 10^9 \text{ N/m}^2$ is shown with a blue line (—). The results of the smallest value with $E = 1.1 \cdot 10^9 \text{ N/m}^2$ is represented by a yellow line (—).

The largest elastic modulus overestimated the measured peak force the 35% of its magnitude and underestimated the excursion of the tip in a 30%. The intermediate stiffness provided a slightly better results. The best fit was obtained with the smallest stiffness, for which the modelled forces and tip positions differed approximately in a 10%.

The previous example may have additional implications for model validation using field measurements. Samples of seagrass can be collected in order to define the geometry of the vegetation of a site and bending tests can also be performed in the laboratory to determine their flexural rigidity. Nevertheless, there is considerable variability in the biomechanical properties of the plants of a meadow, even between individuals of the same species (de Langre, 2013). A number of environmental factors control plant growth and morphology, such as light, water temperature, sediment composition and inorganic carbon availability among others (Barko et al., 1986). For instance, nutrient enrichment may increase the proportion of low-density tissues of the plant, consequently reducing its mechanical resistance (Lamberti-Raverot and Puijalon, 2012). Moreover, the bending stiffness for a single element may vary as the plant deflects in response to the hydrodynamic loading. The roots, stems and leaves of seagrasses have tissues with intercellular spaces (lacunae) filled with gas, mostly oxygen derived from photosynthesis (Karleskint et al., 2012). Such aerial spaces are surrounded by mesophyll cells (Hemminga and Duarte, 2000). Under high deformations the lacunae may be compressed against each other resulting in an increase of the young modulus of the plant. This process could not be captured by the use of a constant value of E . Given the sensitivity of the model to changes in the elastic modulus, deviations from the recorded vegetation motion can be expected associated to the uncertainties in the determination of the plant properties within a natural canopy.

The work done by the vegetation was also represented as a function of the drag coefficient and the added mass coefficient. The dissipation could not be directly compared against the experiments, since the distributed forces along the stem were not measured in the laboratory. The modelled dissipation is shown in Figure 6-E.

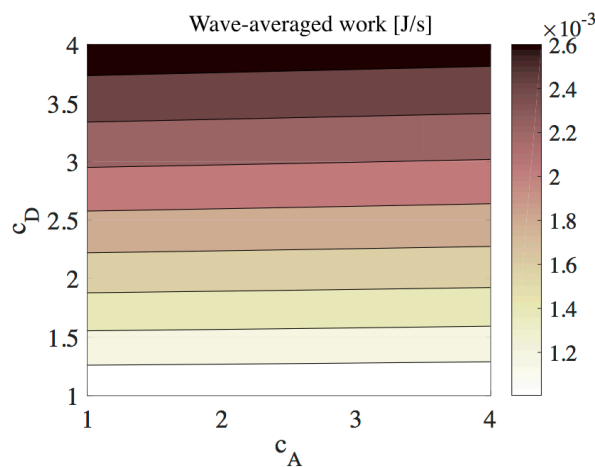


Figure 6-E. Wave-averaged energy dissipation as a function of the drag coefficient and the added mass coefficient.

There is a 20% reduction in the dissipation when using $c_D = 2$ instead of $c_D = 3$, and the attenuation is two times larger for the maximum value of the drag coefficient ($c_D = 4$) compared to the smallest value ($c_D = 1$). Therefore, changes in the force coefficients can lead to important differences in the computed energy dissipation and uncertainties in their determination can alter considerably the predictions of wave-attenuation.